

UNIVERSITY OF CALIFORNIA,
IRVINE

Applications of Synthetic Microchannel and Nanopore systems

DISSERTATION

submitted in partial satisfaction of the requirements
for the degree of

DOCTOR OF PHILOSOPHY

in Physics & Astronomy

by

Preston Hinkle

Dissertation Committee:
Dr. Zuzanna S. Siwy, Chair
Dr. Jun Allard
Dr. Ilya Krivorotov

2017

© 2017 Preston Hinkle

DEDICATION

(Optional dedication page)
To ...

TABLE OF CONTENTS

	Page
LIST OF FIGURES	v
LIST OF TABLES	xi
ACKNOWLEDGMENTS	xii
CURRICULUM VITAE	xiii
ABSTRACT OF THE DISSERTATION	xv
1 Introduction	1
1.1 Nanopores	2
1.1.1 Biological nanopores	3
1.1.2 Synthetic nanopores	4
1.1.3 Applications (introductions)	7
1.2 Nanopore science—physics and chemistry	10
1.2.1 Pore/channel	11
1.2.2 Electrolyte solutions	12
1.2.3 Electrodes	12
1.2.4 Particles	12
1.2.5 Equations of motion for fluidic systems—Navier–Stokes equations . .	13
1.2.6 Motion of ions in a solvent—Poisson–Nernst–Planck equation	16
1.2.7 The diffuse layer—Poisson–Boltzmann equation	17
1.2.8 Electroosmosis	23
1.2.9 Surface conductance and conductance saturation	26
1.2.10 Ion selectivity	28
1.2.11 Ionic current rectification	29
Bibliography	1
2 Development and testing of a single carbon nanotube based pore	32
2.1 Background	32

3 Experimental study of ion conductance property of hybrid conductor-insulator nanopores	34
3.1 Background	34
3.2 Experimental setup	37
3.2.1 Silicon nitride	37
3.2.2 Gold deposition	38
3.2.3 Transmission electron microscope drilling	38
3.2.4 Pore conductance characterization	39
3.3 Experimental results	41
3.4 Modelling results	44
3.5 Conclusion & Future Work	48
4 Resistive pulse studies of aspherical mesoparticles	50
4.1 Background & Theory	50
4.1.1 Dynamic time warping	55
4.2 Experiment	57
4.3 Analysis & Discussion	59
4.4 Conclusions	65
5 Resistive pulse studies of cancer cell deformability	68
5.1 Background & Theory	68
5.2 Experiment and data analysis	74
5.2.1 Experiment and instrumentation control	75
5.2.2 Data analysis	79
5.3 Results & Discussion	83
6 Hybrid resistive-pulse optical detections in microfluidic systems	84
6.1 Background & Theory	84
6.2 Experimental hardware and software	87
6.3 Data analysis software	90
6.4 Results & Discussion	92
6.4.1 Data analysis explanation	92
6.4.2 Straight channels	96
6.4.3 Channels with a central cavity	103
Bibliography	108
A Appendix Title	109
A.1 Lorem Ipsum	109

LIST OF FIGURES

	Page
1.1 Two types of nanopores. Left: Alpha-hemolysin, a biological type of nanopore approximately 1 nm in diameter. Right: A silicon nitride nanopore drilled using a transmission electron microscope (TEM), approximately 10 nm in diameter.	3
1.2 Four important length scales for fluidics and surface forces. milli- : <i>Caenorhabditis elegans</i> (<i>c. elegans</i>) sample, approximately 1 mm in length. Surface tension and capillary forces become significant at this length scale. Fluid dynamics is described by the complete Navier-Stokes equations. micro- : HCT-116 (colorectal cancer) cells, approximately 10 μm in diameter. Surface effects become increasingly important. Gravity becomes increasingly negligible, and systems under small applied pressures are described by having low-Reynolds number. nano- : A protein. Fluidic systems are dominated by surface forces. Liquid within 1 nm of surfaces is entirely contained within the electrical double layer. Fluid is completely non-inertial. sub nano- : A water molecule. Mean-field approximations are no longer valid. Navier-Stokes breaks down. Physics is determined entirely by electrostatic and Van der Waals forces between individual atoms and molecules.	11
1.3 Scheme of the electrical double layer under the Gouy-Chapman and Stern model. There is an abundance of counterions near the pore surface and a reduced number of coions. At the bulk both ion species' concentrations are equal.	18
1.4 Plot of fraction of volume in a nanopore that is within the EDL versus pore diameter. The plot reveals a large super linear increase of total solution within the EDL as diameter decreases, starting at approximately $D \approx 10\lambda_D$	19
1.5 Ion concentrations adjacent to a negatively charged surface according to the Debye-Hückel theory. The plot reveals that the counterion concentration (blue) is enhanced near the wall, and decays approximately exponentially as distance from the wall increases. Oppositely, coions (red) are diminished near the wall, and rise to their bulk value with distance from the wall. The <i>total</i> ion concentration at the pore surface is slightly higher than the total ion concentration in the bulk. The space charge density $\rho_E \propto [c_+(y) - c_-(y)]$ is non-zero near the wall, and decays to zero in the bulk.	22

1.6	Plot of electroosmotic flow along an infinite plane with finite slip length. A net ion charge at the surface experiences a force in an electric field which drags fluid along with it. The force is only present in the electrical double layer, which viscously couples to the rest of the fluid. This fluid flow profile is known as plug flow, and extends far beyond the EDL where it originates.	26
1.7	Reprinted (abstract/excerpt/figure) with permission from [(FULL REFER- ENCE CITATION) as follows: Author's Names, APS Journal Title, Volume Number, Page Number and Year of Publication.] Copyright (YEAR) by the American Physical Society.	27
1.8	An ionic diode formed in a conical nanopore with bipolar surface charge patterning. The region between negative and positive charges is the depletion zone, and provides a large resistance to ion flow through the pore for one voltage polarity. Reprinted with permission from . Copyright 2007 American Chemical Society.	30
3.1	Model for the induced-charge and EDL charges in the hybrid conductor-insulator nanopore. Left: Negative bias applied to gold side. Right: Positive bias applied to gold side. For the positive bias, a depletion zone forms at the junction between the gold and SiN, which is expected to severely limit the conductance. For the negative bias, no depletion zone forms and therefore the conductance is expected to be unhindered. The double conical geometry reflects the expected geometry of SiN pores drilled <i>via</i> a transmission electron microscope electron beam.	36
3.2	A ~ 15 nm SiN pore drilled <i>via</i> TEM.	39
3.3	A current-voltage time series alongside the current-voltage curve produced from it. Left: Current-voltage time series. Each continuous line corresponds to one voltage setting; once a voltage value is set, the current does not significantly vary. Right: Traditional pore I-V curve. The asymmetry in the current with respect to voltage (present in both signals) is the hallmark indicator of ionic current rectification.	40
3.4	IV curves taken of bare SiN pores. The symmetry in the IV curve reveals no inherent rectification of the TEM drilled pores.	41
3.5	IV curves taken of Au-SiN pore in 100 mM and 500 mM KF. The sym- metry in the IV curve reveals no inherent rectification of the TEM drilled pores. The ion rectification ratio R is lower in the higher concentration solution, as is expected from basic considerations of EDL thickness.	42
3.6	IV curves taken of Au-SiN pore in 500 mM KCl and KF. The rectifi- cation ratio R is lower in the KCl solution than in the KF solution, which is expected due to the additional contribution of the static charge from adsorbed Cl^- ions on the gold surface.	43
3.7	COMSOL simulations.	45
3.8	COMSOL simulations.	46
3.9	COMSOL simulations.	46
4.1	adsf	52

4.2	Comparison of standard Euclidean distance metric (left) and distance metric as determined by dynamic time warping (right). Notice that the Euclidean distance does not take into account small displacements of the two signals in time, despite their obvious similarity. On the other hand, dynamic time warping is able to account for small mismatches in time by finding the connections between points that minimizes the total cost.	54
4.3	Distance (left) and cost matrices (right) of two resistive pulse signals as determined by dynamic time warping. The element (i, j) in the distance matrix represents the Euclidean distance between the two signals, $(S_i - S'_j)^2$. Every element in the cost matrix represents the summed Euclidean distance along the minimum path that arrives at that point. Therefore, the point at the lower right-most point in the distance matrix is the summed cost to completely connect the two signals. The path that yields the cost of that element in the matrix is represented by the yellow dashed line.	55
4.4	Scanning electron microscope images of metal replica of track-etched PC (left) and PET (right) pores. The pores were filled with metal and the polymer was completely etched a way, leaving a metal structure that is the inverse image of the pore. The metal was imaged in a scanning electron microscope. While the PC pores are nearly perfectly cylindrical in shape, the PET pores are characterized by rough inhomogeneities across their entire surface, punctuated with large local bumps. The large bumps in the images of the metal replicas correspond to equally large cavities in the PET pore.	58
4.5	Transmission electron microscope images of polystyrene beads and silica nanorods. While the polystyrene beads are nearly perfectly spherical, the silica nanorods are approximately ‘bullet shaped’. For the purposes of this work, we approximated their shapes as ellipsoids in order to apply equation 4.2.	58
4.6	Resistive pulse events through PC (left) and PET (right) pores. As expected, the PET events are highly irregular and reflect the interior irregularities of the PET pore itself. On the other hand, the PC pores show no such irregularity. The events show that PC pores have large resistances at the beginning and end, reflecting the narrow, ‘pinched’ diameters at the openings of the pores.	59
4.7	Resistive pulse events of a 410 nm diameter sphere (red), and 590 nm (blue) and 1920 nm (green) in length rods. The top row shows a cartoon scheme of the pore with the particles inside its interior. The bottom resistive pulse event in each column corresponds to the raw recorded data; events above this are smoothed <i>via</i> the moving average transformation. The bottom left figure shows the raw events on the same scale.	61
4.8	Resistive pulse signal of a single long rod passing through a PET pore. The variation in the amplitude of the current signals that the pore has an inhomogeneous interior shape.	63

4.9	Resistive pulse signal of a single short rod passing through a PET pore alongside many instances of the moving average transformation performed on the signal for different length intervals. As the length interval is increased, the finer structure of the resistive pulse signal is smoothed over. For the greatest length measured, many of the features prominent in the raw signal have disappeared..	64
4.10	Raw resistive pulse signal of a single long rod matched with the signal of a short rod that has been transformed via the moving average process. The aligned points were determined by the dynamic time warping algorithm, and the particular transformation shown was the one that minimized the difference between the two signals, also determined by the dynamic time warping algorithm.	64
4.11	Histogram of particle length as determined by dynamic time warping along with the actual distribution of sizes determined by electron microscopy imaging. A normal distribution is fit to the histogram of particle lengths as determined by dynamic time warping and shown to be in good agreement with the expected distribution.	65
5.1	Resistive pulse amplitude $\Delta I/I_p$ for equal volume spheroidal objects relative to a sphere. The polar axis of the particle is aligned with the channel's axis, so that oblate geometries correspond to motion along the channel axis. The values come from equation 5.1 when the correct shape factor f_{\parallel} is applied.	72
5.2	Confocal images of 293-T (left) and HCT-116 (right) cells. Scale bars are $50 \mu\text{m}$ long.	75
5.3	Example ellipse fitting protocol for a single detection within a single event. The left column of each row shows the current image transformation. The central column shows the raw frame with the pixels shaded green with intensity according to the intensity of the pixels in the transformed image. The right column shows pixel intensity in the processed image. 1: Raw image. 2: Image is cropped in the vicinity of the particle. 3: Template image is subtracted off. 4: Pixel intensity is rescaled. 5: Laplacian derivative. 6: Pixel intensity thresholding. Notice the histogram becomes binary distributed. 7: Morphological closing of image. 8: Image is dilated and subtracted from undilated image, leaving a thin shell around the border of the cell. 9: Ellipse is fit to the cell's border.	81
5.4	Ellipse fits for a 293-T cell passing through a $15 - 30 - 15 \mu\text{m}$ channel at various positions. Notice that in the narrow portions of the channel the particle assumes a prolate (axially-elongated) shape, while in the central cavity it assumes an oblate (laterally-elongated) shape, in agreement with the motif presented in Fig. ??	82
6.1	Hardware set up for the hybrid RP-IM experiments.	88
6.2	cell_controller, a GUI program written in C++ and the Qt Framework. The program controls the instruments used to run the experiment.	89

6.3	<i>Screen capture of the GUI component of the pore-stats software library.</i> The program enables fast and accurate extraction of RP events from the baseline data. The main panel shows the raw time-series data (zoomed out), with events that were detected with the program highlighted in blue. The bottom left plot shows a single event that has been targeted by the user. The bottom right plot shows a scatterplot of the current and duration for all events detected, and shows how bulk events can be rejected by selecting a region of the scatter plot. The bottom right buttons and fields are used to change the search parameters, to begin the search, filter data, and enable various other functionalities.	91
6.4	Images of some of the channels used in this study with trajectory lines overlaid. Each line corresponds to the passage of a single particle through the channel, tracked using image detection techniques. The channels fall into two categories, channels that are complete straight and channels which have central cavities.	93
6.5	Event matching protocol for the RP and IM signals. a.	95
6.6	Resistance maps of the straight channels used in this study. The resistance maps show that the resistance is most concentrated in the micro constriction, and that the resistance is small elsewhere. A region of finite resistance exists between the micro constriction and the reservoir leading up to the channel. This region is known as the channel's access resistance.	97
6.7	Plot of $\Delta I/I_p$ vs axial-position x_c for polystyrene beads passing through the PDMS channels. The plots reveal that the current does not reach its maximal value until the particle is well inside the channel.	98
6.8	Plot of the measured voltage (similar to current) of simulated particle translocations through a pore, with off-axis contribution according to the results of Berge <i>et al.</i> (Eq. 6.3). The plot reveals the effects of off-axis translocation, namely that the distribution of measured ΔV shifts towards greater values and broadens.	100
6.9	Scatter plot of translocation duration Δt versus event amplitude $\Delta I/I_p$ for the four straight channels studied, with straight line fits. The fits reveal the positive correlation between translocation time and off-axis position, as observed by Berge <i>et al.</i>	101
6.10	Translocation duration Δt and RP amplitude $\Delta I/I_p$ versus lateral position y_c for four straight channels.	102
6.11	Resistance maps of channels having a central cavity. The resistance maps show that the resistance is most concentrated in the narrow portions of the channel, and less-so in the central cavities (as expected from $R = \rho \int dz / A(z)$).	104
6.12	Resistive pulse amplitude $\Delta I/I_p$ versus axial position x_c (a) and versus time t (c). The camera image (b) shows several stills of particle positions aligned with the instantaneous resistive pulse value in the plot above (a).	105

6.13 Histograms of the ratios of the pulse amplitude $\Delta I/I_p$ in the narrow portion of the channel and in the central cavity for the two types of cavitated channels studied. The dashed lines indicate the theoretical values predicted by Eq. 6.5. In both cases, the theoretical predictions closely match the experimentally obtained results. 106

LIST OF TABLES

	Page
5.1 Class Mark List	76

ACKNOWLEDGMENTS

I would like to thank...

(You must acknowledge grants and other funding assistance.

You may also acknowledge the contributions of professors and friends.

You also need to acknowledge any publishers of your previous work who have given you permission to incorporate that work into your dissertation. See Section 3.2 of the UCI Thesis and Dissertation Manual.)

CURRICULUM VITAE

Preston Hinkle

EDUCATION

Doctor of Philosophy in Computer Science	2012
University name	<i>City, State</i>
Bachelor of Science in Computational Sciences	2007
Another university name	<i>City, State</i>

RESEARCH EXPERIENCE

Graduate Research Assistant	2007–2012
University of California, Irvine	<i>Irvine, California</i>

TEACHING EXPERIENCE

Teaching Assistant	2009–2010
University name	<i>City, State</i>

REFEREED JOURNAL PUBLICATIONS

REFEREED CONFERENCE PUBLICATIONS

Awesome paper	Jun 2011
Conference name	
Another awesome paper	Aug 2012
Conference name	

SOFTWARE

nanoIV	https://github.com/tphinkle/nanoIV
<i>Keithley 6487 Picoammeter control GUI program. Allows measurement of current-voltage and time-series data.</i>	
pore stats	https://github.com/tphinkle/pore_stats
<i>GUI program and Python library for extracting and analyzing resistive pulse data.</i>	

ABSTRACT OF THE DISSERTATION

Applications of Synthetic Microchannel and Nanopore systems

By

Preston Hinkle

Doctor of Philosophy in Physics & Astronomy

University of California, Irvine, 2017

Dr. Zuzanna S. Siwy, Chair

The abstract of your contribution goes here.

Chapter 1

Introduction

The introduction to this dissertation is structured as follows. First, we introduce the main topic of this dissertation and of my PhD research work, the nanopore. This section serves to introduce the reader first, to the basic definition of a nanopore and then to some of their applications, in addition to miscellaneous facts about nanopores that provide context for why they are of interest to scientists. This section is entirely qualitative and does not aim to make any statements about the underlying physics needed to understand nanopore systems. Subsequently, I introduce in three stages the physics that is relevant to nanopore systems. It turns out that if we take a macroscaled system (say, a tube rather than a nanotube) and slowly shrink it in size, then as the system size shrinks new types of physics emerges and become increasingly relevant to the system. We will start by addressing the relevant physics at the milliscale and shrink in intervals of powers of three, stopping at the sub-nanoscale. Therefore, the progression looks like milli-, micro-, nano-, and finally, sub-nano-. To provide a bigger picture of the journey through different length scales, the progression looks like ant, cell, protein, molecule.

1.1 Nanopores

Unlike most physics jargon, the name nanopore is entirely self-explanatory. In fact, the following is a terse (but accurate) definition of a nanopore:

Definition 1.1. *A nanopore is a hole on the order of 1 nm in size*

As we will discover, this definition, while accurate, does not do justice to the field of nanopore research.

Nanopores generally belong to two classes, biological and synthetic. Because nanopores can be found in biology, many scientists are interested in studying them in their own right, to better understand how biological systems function. On the other hand, nanopores, both biological and synthetic, can be used in a surprisingly large variety of applications, with the total count of such applications constantly increasing. In this section we will briefly discuss the types of biological nanopores and where they are found in nature, and then move on to describing different types of synthetic nanopores. Given the loose criteria required by 1.1 for something to constitute a nanopore, listing off every type of either biological or synthetic nanopores would be impossible; instead, I seek to introduce the most relevant types, with an admitted bias towards the types of nanopores I am most familiar with and that I have worked with in my research. After discussing the various types of nanopores, I will give a summary of applications in which nanopores see use. Some of these applications, for instance resistive-pulse sensing, are a major part of this dissertation and will therefore be discussed in much greater detail later on, while others, such as DNA sequencing, are important enough to be mentioned but not discussed in significant detail later on. An extensive list of references, including those not explicitly referenced in this work, will be included should the reader wish to read more on a particular topic.

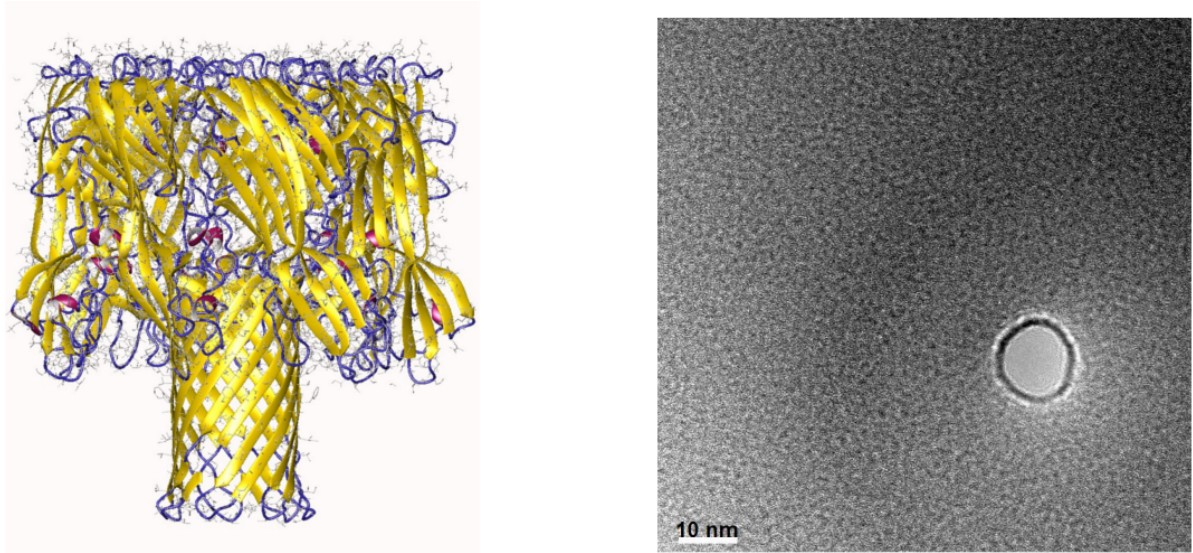


Figure 1.1: Two types of nanopores. **Left:** Alpha-hemolysin, a biological type of nanopore approximately 1 nm in diameter. **Right:** A silicon nitride nanopore drilled using a transmission electron microscope (TEM), approximately 10 nm in diameter.

1.1.1 Biological nanopores

As mentioned before, nanopores exist naturally in biology. Their most important function is to enable passage from one region to another, much like a tunnel does; however, where a tunnel permits cars, trucks, etc., the passengers in nanopore systems are water, ions, proteins, etc. Nanopores typically connect regions that are necessarily divided in order for a cell to function. Membrane-bound nanopores are structures made out of protein that are embedded in a cell's lipid bilayer that connect the outside of a cell to the inside of a cell. They serve the useful function of regulation osmotic pressure by allowing water to enter and exit the cell, and also balance voltage differences by allowing passage of important electrolytes such as sodium, potassium, and chloride. Therefore, maintaining homeostasis is one of the chief functions of these types of nanopores. These pores also enable passage of messenger molecules that enable extracellular messaging, crucial to all multicelled organisms. Like lipid bilayer pores, there are also pores in the nuclear membrane that enable transport into and out of the nucleus of a cell. These pores' chief responsibility is to allow the passage of

messenger molecules in and out of the nucleus.

The most fascinating property of nanopores is their capacity for active management of transport. For instance, some nanopores may open or close when the voltage difference across them surpasses a threshold; other types of nanopores are *ion selective*, permitting passage of some types of ions while denying passage to others. *Active* transport is absolutely crucial to biological systems; if all nanopores were passive holes that permitted anything to pass through, the system would equilibrate in a homogeneous, non-functional soup of maximum entropy—life simply could not exist. Fortunately for us, nanopores are active transport regulators and life goes on. Going back to our tunnel analogy, nanopores act more like regulated tunnels, for instance some with guards that permit small cars only and deny trucks, or permit passage in only one direction, etc.

1.1.2 Synthetic nanopores

Advances in nano- and microfabrication have led to an enormous number of different types of synthetic nanopores. Synthetic nanopores can be made from a variety of different types of materials, and often their geometry (shape and size), as well as their surface chemistry properties, can be tailored to introduce specific types of behavior. However, the type of material used to make the nanopore most often determines the types of geometries and chemistries that are allowed. The following is a list of common types of nanopores, with a description of the type of material they are made from, their permissible length scales, and other miscellaneous relevant facts about them.

Monolayer pores. The invention of graphene, a monolayer of carbon atoms, and later MoS₂, opened the possibility of creating nanopores with a length of a single atom. These types of pores are created by punching through the thin monolayer, typically with an electron or ion beam. While still a very new field of study, these pores may see future use in

desalination (removing electrolyte ions from water).

Carbon nanotubes. A carbon nanotube can be conceptually understood as a rolled up tube of one or a stack of graphene layers. Graphene is a monolayer of carbon atoms, and therefore a carbon nanotube itself is a type of pure crystal structure. The lattice arrangement of carbon atoms permits only certain tube diameters, which itself depends on the chirality of the tube (the way the tube is rolled up). Carbon nanotubes are interesting to researchers because of the exotic behaviors they exhibit that are not present in most other types of nanopores—for instance, they exhibit frictionless transport of water, hydrogen-dominant conductance (*via* the Grotthus mechanism), ion selectivity, and more. As of the submission of this dissertation, the use of CNTs as nanopore is still a new field of study, and the physical mechanism for the previously mentioned behaviors is still poorly understood. Nevertheless, the extreme confinement (1 nm and below for small CNTs) and the atomic-level precision of their structure are believed to be responsible. Another interesting aspect of the smallest CNTs is the breakdown of mean-field physics in describing their behavior. For instance, the Navier-Stokes equations which describe fluid dynamics, breaks down at this level because the water must be considered at the molecular level; the mean-field approach is no longer valid. Because they are still new, we do not yet know the exact applications that these nanopores will see use in. However, it is likely that they could be used in desalination applications (removing ions from water), or in ionic circuits as cation selective elements.

Silicon nitride. Silicon nitride is a type of crystalline semiconductor that permits engineering of nanopores through several different fabrication processes. Briefly, very thin layers of silicon nitride (e.g. 10 – 100 nm) are grown, and a hole is bored through via either electron or ion beam milling. For instance, in one project of this dissertation I describe a project conducted with silicon nitride pores that were drilled via high-energy transmission electron microscope (TEM). Depending on the type of mill used (ion or electron), the size of these nanopores ranges, but the diameter is generally in the range of 1 – 100 nm. One advantage of

silicon nitride pores is their smooth interior geometries, as well as the native silane chemistry on the surface that permits many types of chemical modifications. These types of pores are used as ionic rectifiers (after modification), and in resistive pulse applications.

Glass nanopipettes. Quartz pipettes can be heated and slowly stretched, reducing the tip diameter with the possibility of reaching the nanoscale. Unlike the previously mentioned pores which all had an approximately cylindrical geometry, these nanopipettes have a conical shape. These pores have a couple advantages. First, the stretching process itself is simple and can be used to create many pores over a short amount of time. Second, the surface chemistry of the glass or quartz is amenable towards chemical modification. These pores may be used in ionic circuits, in resistive pulse sensing, or as a surface probe, by monitoring the current through the pipette as it approaches a charged surface.

Track-etched polymer nanopores. These types of pores are perhaps the most robust, dependable types of nanopores. Pore formation is a multistep process. First, untouched polymer membranes are irradiated by a single heavy isotope of an element such as gold and xenon, that has been accelerated to high speeds in a particle accelerator. The ion rips through the membrane, uniformly dispersing some of its kinetic energy into the surrounding polymer, and breaking the bonds in the polymer surrounding its trajectory. This location of damaged polymer bonds is known as the ‘damage track’. An ion detector is placed at the exit point of the membranes so that the beam can be switched off when a single ion is detected. This detection, along with a solid mask placed in front of the beam that blocks the vast majority of the ions in the beam, ensures that films that only have a single damage track can be prepared. This step, known as irradiation, must be performed off-site at a particle accelerator. After heavy ion irradiation, the membranes are immersed in an etchant solution such as NaOH or KOH. The etchant preferentially attacks the polymer in the damage track, clearing out the polymers along the track much faster than elsewhere in the membrane. Once the track has been etched out, the rest of the membrane is isotropically etched slowly by the NaOH. Pores

prepared by the track-etch technique have a few advantages, including a customizable size and geometry. By putting etching solution on only one side of the membrane, it is possible to create conical pores of various aspect ratios. By applying a voltage across the pore during the etching process, the ionic current can be monitored and the etching process can be stopped at a particular current level, allowing the researcher customize the pore diameter. Another advantage of these pores is the carboxyl groups native to their surfaces, which permit many types of useful chemical modifications.

Hybrid biological-synthetic nanopores. Biological nanopores, such as alpha hemolysin, aerolysin, or MSPA to name a few, can be isolated from their host biological systems and inserted into synthetic systems, forming a hybrid biological-synthetic complex. In these cases, the pore is entirely biological, but the complex does not appear naturally in nature, and the pores may be used in engineering or scientific applications. To make matters even more confusing, such pores may also be genetically modified to change some of their behavior, meaning they are derived from biology but are synthesized in the lab. For instance, the company Oxford nanopore invented a genetically modified alpha hemolysin nanopore that is especially adept at differentiating between nucleotides, and is currently being used in DNA sequencing applications.

1.1.3 Applications (introductions)

So far, I have hinted at or referred to nanopore applications without getting into specifics. Just as there are too many types of nanopores to enumerate, there are too many applications of nanopores to list them all off. This is a list of some of the most important applications of nanopores.

Analyte detection and characterization with the resistive pulse technique. Surprisingly, nanopores may be used as a sort of particle characterizer using something called the

resistive pulse technique, which works as follows. A voltage is applied across the nanopore, which induces a measurable ionic current to flow through the channel. If a particle enters the nanopore, the particle will occupy a volume that otherwise would be occupied by high-conductivity ions, increasing the pore's resistance, and decreasing the measured current. It turns out that by studying the nature of the decrease in the current, we can gather some information about the transiting particle. For instance, by counting the number of pulses in the measured ionic current, we can determine the concentration of particles in the suspension. The size of the particle can be determined by relating it to the depth of the pulse—larger particles block the current to a larger degree, and therefore create deeper resistive pulses. If the particle is at least partially driven through the channel *via* electrophoresis (discussed later), then the particle's surface charge can be determined by the length of the pulse, or ‘dwell time’ of the particle.

One advantage of resistive pulse sensing is its scale-independence, which is a result of the generality of the physics involved. For this reason, resistive pulse sensing has been used in a large number of applications. The original use of the resistive pulse technique was in performing red blood cell counts (channel size approximately $\sim 100 \mu\text{m}$ which was achieved by Coulter in 1953; this is the reason why sometimes the resistive pulse technique is referred to as the Coulter counter principle, or simply the Coulter principle. Since Coulter's original design, the resistive pulse technique has been used in counting smaller specimens such as exosomes, proteins, and viruses, used to measure particle rigidity, and perhaps most importantly, in DNA sequencing. The basic idea of resistive-pulse sensing for DNA sequencing is that the four types of nucleotides have slightly different sizes, and therefore lead to four unique current blockages. DNA can be slowly threaded through a nanopore while the current is monitored, and the discrete states in the resulting time-series of the measured current yield the sequence of DNA.

Water desalination. Charged nanopores are slightly ion selective, meaning they preferen-

tially allow one polarity of charge over another to pass through. If one side of a nanopore membrane is filled with electrolyte solution and a pressure is applied, water will pass through the pore, and due to the selectivity of the membrane, fewer ions will pass through than are contained in the bulk. In this way, nanopores can be used for water desalination. This mechanism of salt rejection is electrostatic, since the finite potential in the vicinity of the pore walls is responsible for screening ions. Traditional water desalination relies on reverse osmosis membranes that are completely impermeable to salts, and therefore *sterically* reject ions. In future sections we will discuss the physics involved with water desalination.

Nanopore ionics and ionic circuits. Ion transport is fundamentally important to all cellular life. At the most basic level, single cells maintain homeostasis with their environment by maintaining a careful balance of salt ions across their membranes. This balance is regulated by a rich variety of ion channels, each with their own specific functionality. For instance, potassium can diffuse through potassium channels at nearly the bulk diffusion rate (i.e. the channel hardly impedes their motion), while sodium is completely blocked, an amazing feat considering the ions are nearly identical, save a minute difference in their hydration radii. Beyond maintaining homeostasis, ion channels are also responsible for propagating electric signals along axons, crucial for signaling in multicellular organisms.

One of the holy grails in nanopores is being able to reproduce the functionality of these biological pores, that were created by millions or billions of years of evolution, in synthetic systems. The ability to do so could create a revolution in ion conducting systems, analogous to the revolution in electronics that was created by the invention of the solid-state transistor. However, the goal of ionics is not to replace wires, capacitors, and transistors with ion channels and pores; indeed, ions travel orders of magnitude slower than electrons, and therefore ionic systems are expected to act more slowly than electronic systems. Instead, integrated ionic circuits could be used for complex signaling since each ion carries its own information, and for controlling the transport of biomolecules. One needs only to look at

biology for inspiration on the application of complex ion channels.

1.2 Nanopore science—physics and chemistry

The actors at play in nanopore systems include the fluid solvent that fills the pore and its exterior regions, the charged ion species, the pore surfaces themselves, the electrodes, and finally, any particles (cells, biomolecules, etc.) present in the system. In the following sections we will delve into the physics that determines the interplay between these actors. As it turns out, as we shrink a system size from the macro to nanoscale, new regimes of physics become increasingly important. Therefore, not all of the physics mentioned in the upcoming sections are applicable to all length scales; for instance, the properties that make nanopores behave more interesting than just an open space only emerge close to the nanoscale, and are irrelevant in microscale systems. We can think of four distinct length scales at which the physics, and hence the system behavior, is sufficiently differentiated so as to give that scale its own identity. These scales are the milliscale, microscale, nanoscale, and subnanoscale. For example, microscale physics is sufficiently different from nanoscale physics that one may be an expert in one of the two, but not the other. While the actors at play in these two systems—water, ions, particles, etc.—are all the same, the observed behavior of the systems can still be quite different. To give a brief preview of what is to come, the most important physics involved in nanopore theory is fluid mechanics (to describe the forces on the solvent), electrostatics (because of the voltage boundary conditions imposed by electrodes and charged surfaces), electrokinetics (due to migration of charged species under electric fields), and statistical mechanics (to describe the ensemble behavior of the ions and diffusion). Before moving on, it is important to note that concepts in chemistry are also very important in nanopores. For instance, electrochemical theory explains the mechanism for how an ion current turns into an electron current at the electrode-liquid interface. As

another example, the charges present at the surfaces in almost all surfaces in contact with a fluid are due to the chemical groups, and their charged state. In the following sections, whenever chemistry is relevant, I will mention its role in creating the entity that we then go on to describe insofar as is possible with physics alone. For example, I will acknowledge the charge of a nanopore is due to chemical groups attached to its surface, but will then proceed agnostically, treating the charges as if they were a perfect model surface-charge, uniformly distributed over the surface of the pore. Chemistry will be invoked in the main chapters of this thesis as it relates to specific aspects of the projects.

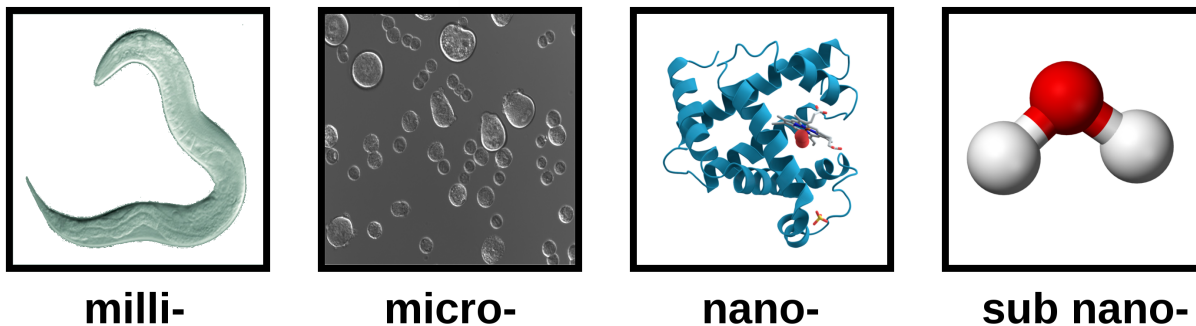


Figure 1.2: Four important length scales for fluidics and surface forces. **milli-**: *Caenorhabditis elegans* (*c. elegans*) sample, approximately 1 mm in length. Surface tension and capillary forces become significant at this length scale. Fluid dynamics is described by the complete Navier-Stokes equations. **micro-**: *HCT-116* (colorectal cancer) cells, approximately 10 μm in diameter. Surface effects become increasingly important. Gravity becomes increasingly negligible, and systems under small applied pressures are described by having low-Reynolds number. **nano-**: A protein. Fluidic systems are dominated by surface forces. Liquid within 1 nm of surfaces is entirely contained within the electrical double layer. Fluid is completely non-inertial. **sub nano-**: A water molecule. Mean-field approximations are no longer valid. Navier-Stokes breaks down. Physics is determined entirely by electrostatic and Van der Waals forces between individual atoms and molecules.

1.2.1 Pore/channel

The pore/channel itself is the primary actor of interest in our systems. The pore is created in some material, and the material properties as well as the fabrication procedure dictate the shape and geometry of the pore. As we will see, ionized chemical groups on the surface

of the pore play as important a role as geometry in determining the behavior of the pore system.

1.2.2 Electrolyte solutions

Life on Earth exists in primary a *fluid* environment, with the primary fluid being water. Water is the solvent for the chemistry of our bodies, and acts as the medium that allows electrolytes to ionize and transport between areas. In synthetic nanopore systems, we immerse our pore in an electrolyte solution that fills the channel, and under an applied voltage induces conduction of ions.

1.2.3 Electrodes

In order to create an external voltage in our system, an electronic voltage must be transformed into an ionic voltage potential. This is achieved *via* ion electrodes, which allow transferrance of electrons into the ions of the solution and vice-versa, and the ions from the electrode then become the conductors in the system. This transferrance is known as a redox reaction in chemistry. For the rest of the thesis, unless specified we turn a blind eye to the chemical conversion process at the surface of the electrodes, and pretend that our electrodes are ideal voltage sources.

1.2.4 Particles

Because so many of the applications of interest for nanopore and microchannel studies involve biomolecule manipulation, we often work with electrolyte solutions that contain a suspension of particles in addition to the ions. The particles used are tied to the application, but often

respond in the same way to forces present in the system.

1.2.5 Equations of motion for fluidic systems—Navier–Stokes equations

One of the major actors in nanopores systems is the fluid solvent, which may remain at rest or, more commonly, move in response to forces present in the system. Because the motion of the solvent couples to the motion of other actors present in the system, understanding the physical laws governing the fluid medium is crucial. For systems large compared to the size of molecules, we make the approximation that the fluid is a continuous rather than discrete medium. In reality, we know that fluids are not continuous but are made up of discrete atoms and molecules, which may make this approximation seem limiting. However, the continuum approximation has been shown to accurately describe fluids all the way down to the scale of a single nanometer, and thus are valid in most systems of interest [2]. Under the continuum approximation, the equations of motion of the fluid are described by the Navier-Stokes equation.

The Navier-Stokes equations are actually three coupled 2nd order non-linear partial differential equations that yield the fluid vector velocity \vec{u} . Despite the apparent complexity of the equations, they can be derived simply using Newton's 2nd law $\frac{d\vec{p}}{dt} = \vec{F}$ and conservation principles.

Consider an integrable quantity ϕ that is convected in a fluid field with velocity \vec{u} . For a given control volume, the continuity equation relates the time rate of change of ϕ in the volume with the flux through the boundaries due to convection in the fluid field and the sources and sinks that create or consume the field. The continuity equation is

$$\frac{d}{dt} \int_V \phi dV = - \int_A \phi \vec{u} \cdot \hat{n} dA - \int_V s dV,$$

where dV is the control volume, dA its bounding surfaces, \hat{n} the unit normal to the surface dA , and s are the sources and sinks present in the control volume, with the convention that sinks are positive and sources negative.

If we consider the quantity to be the max flux (the momentum density) $\phi = \rho \vec{u}$ and simplify the equation, we arrive at the Cauchy momentum equation:

$$\begin{aligned} \rho \frac{\partial \vec{u}}{\partial t} + \rho \vec{u} \cdot \vec{\nabla} \vec{u} &= \vec{s} \\ \rho \frac{D \vec{u}}{Dt} &= \vec{s}. \end{aligned} \tag{1.1}$$

The derivative $\frac{D}{Dt}$ in the second term is the material derivative, which describes the time rate of change of the velocity of a fluid parcel given that its change is time and position-dependent. Written in this way, we see that the equation for momentum continuity in the fluid leads us to a Newton's second law type expression. The term $\rho \vec{u} \cdot \vec{\nabla} \vec{u}$ is known as the convective term, and describes the transport of momentum due to motion of the flow-field itself.

Next, we replace the sources and sinks \vec{s} with their physical origins. Because the quantity of interest is momentum, we recognize that the sources and sinks must be forces (force densities) in the system, which can generally be broken down into body forces, such as those due to electrostatics or gravity, and surface forces. Therefore, we replace the source/sink term with $\vec{s} = \vec{\nabla} \cdot \sigma + \sum_i \vec{f}_i$, where σ is the Cauchy stress tensor and \vec{f}_i is a body force acting on the control volume. We can further break down the Cauchy stress tensor into the sum of two

separate pieces, an isotropic pressure tensor $p\mathbf{I}$ and the stress tensor τ due to *viscous* forces. For Newtonian fluids like water, there is a fundamental postulate that the stresses σ are proportional to the strain rates, with proportionality constant η , the viscosity of the fluid. In this case, $\tau = 2\eta\epsilon$, where ϵ is the strain rate tensor which describes the deformation of the fluid due to velocity gradients. When the stress tensor τ is replaced with the strain rate tensor ϵ via the constitutive relationship for Newtonian fluids, we finally arrive at the full Navier-Stokes equations:

$$\rho \frac{\partial \vec{u}}{\partial t} + \rho \vec{u} \cdot \nabla \vec{u} = -\nabla p + \eta \nabla^2 \vec{u} + \sum_i \vec{f}_i. \quad (1.2)$$

Solving the Navier-Stokes equation yields the correct fluid velocity \vec{u} at all points in the system. While it is a complex equation, in many systems it can be simplified and solved analytically. For instance, in microfluidic channels gravity is often insignificant compared to other inertial and pressure forces, and is often ignored. Additionally, in small channels and with relatively small velocities, the inertial/convective term $(\vec{u} \cdot \nabla) \vec{u}$ is often negligible and can be dropped. To quantify this notion, we introduce a dimensionless parameter called the Reynolds number:

$$Re = \frac{\rho u L}{\eta}. \quad (1.3)$$

L in the above equation is the characteristic length scale of the flow, which in pores or channels is chosen to be the diameter by convention. The Reynolds number Re is essentially a ratio of the strength of inertial/convective forces to inertial forces. For high Reynolds number, convective forces dominate and we expect turbulent and chaotic flow. At low

Reynolds number, inertial forces dominate and fluid motion is laminar and smooth. The Reynolds number is useful for knowing which two regimes we are in, and can provide intuition about the behavior of our systems. In microfluidic systems, we are seldom in the turbulent regime, and are often at medium to low Reynolds numbers. Nanofluidic systems are almost certainly non-inertial for reasonable external pressures.

1.2.6 Motion of ions in a solvent—Poisson-Nernst-Planck equation

While the Navier-Stokes equations of motion describe the motion of the fluid solvent, the Poisson-Nernst-Planck, or PNP equations describe the motion (flux) of ions in the solution. The flux of ions is due to the superposition of diffusion, advection in the fluid solvent (known as ‘streaming’ current), and migration in electric fields (e.g. due to external voltage sources). Summing the individual contributions, the PNP equation for the flux of an ion species is

$$\vec{J}_i = - \left[D_i \nabla c_i - \vec{u} c_i + \frac{D_i z_i e}{k_B T} c_i \nabla \phi \right], \quad (1.4)$$

where \vec{J}_i is the ion flux of species i , D is the diffusion coefficient, c is the ion concentration, z is the ion valence, e is the elementary charge, k_B is the Boltzmann constant, T is the temperature, nad ϕ is the electric potential. The first term in eq. 1.4 is the diffusion term, which essentially states that there is a flux of ions in the opposite direction of the gradient of the ion concentration. The second term is the advective term, which accounts for the ions moving with the fluid solvent. The final term is the electric migration term, which describes the motion of the ions in an electric field gradient.

1.2.7 The diffuse layer—Poisson-Boltzmann equation

The diffuse layer is of paramount importance in nanopore studies; without it, nanopores would simply act as passive conductors with no interesting conductance properties. When any type of material is submitted in solution, charges tend to appear at the surface. Some of these charges are due to specific adsorption or immobilization of ions or molecules onto the surface, which give the surface some charge. The other charge type which is usually more significant is due to the ionization of chemical groups native to the surface of the pore. The type of chemical group present on the pore depends on the material out of which the pore is made. For instance, polymer pores prepared via the track-etch technique are formed when an etchant solution cleaves the monomer units in half, exposing a carboxyl group, which is then deprotonated at basic solution pHs. On average there are approximately 1 of these surface groups per 4 nm^2 , yielding a net surface charge density of 0.25 e/nm^2 . In any case, the total charge that mobile ions ‘feel’ in the solution is the sum of the adsorbed charges (Stern layer), plus the chemical groups attached to the surface, plus the immobilized ions within the slip layer. The electric potential immediately outside the Stern layer due to these superimposed charged sources is known as the ζ potential.

Because the ion solution is conductive, mobile ions outside the Stern layer will redistribute themselves near the charged surface to counter or ‘screen’ its ζ -potential. This screening layer is known as the Debye layer, and is characterized by an enriched number of counterions (ions of opposite charge polarity to the wall) and a depleted number of coions. As we will see, the electrical double layer has a characteristic length scale known as the Debye length λ_D , which ranges from $0.1 - 10\text{ nm}$ for most solution concentrations. Figure 1.3 gives a view of the electrical double layer under the combined Gouy-Chapman and Stern models.

Nanopore’s interesting behavior emerges when a non-negligible amount of the total volume is within a distance of λ_D of the pore wall. Assuming $\lambda_D = 1$, figure 1.4 shows the fractional

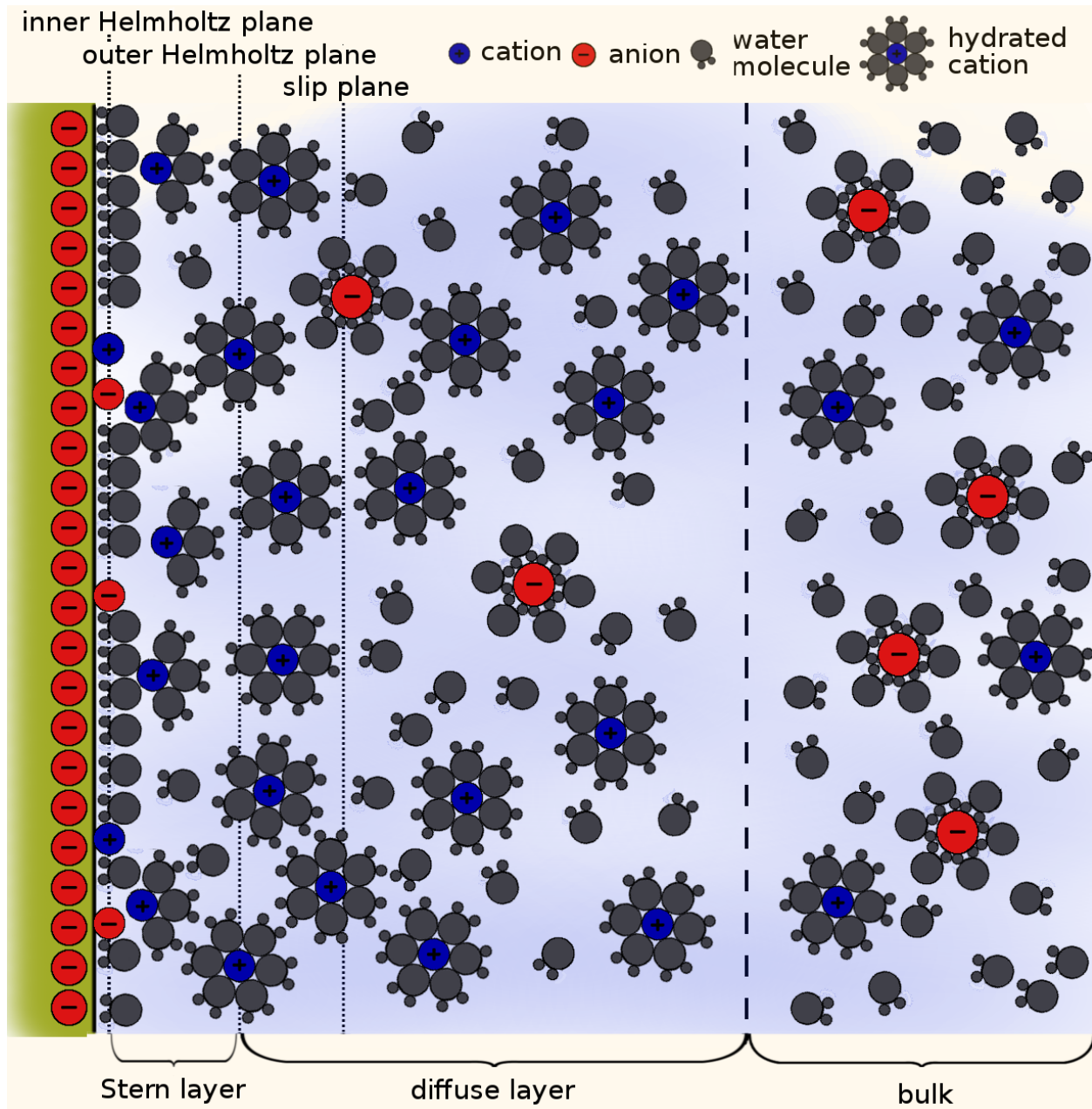


Figure 1.3: Scheme of the electrical double layer under the Gouy-Chapman and Stern model. There is an abundance of counterions near the pore surface and a reduced number of coions. At the bulk both ion species' concentrations are equal.

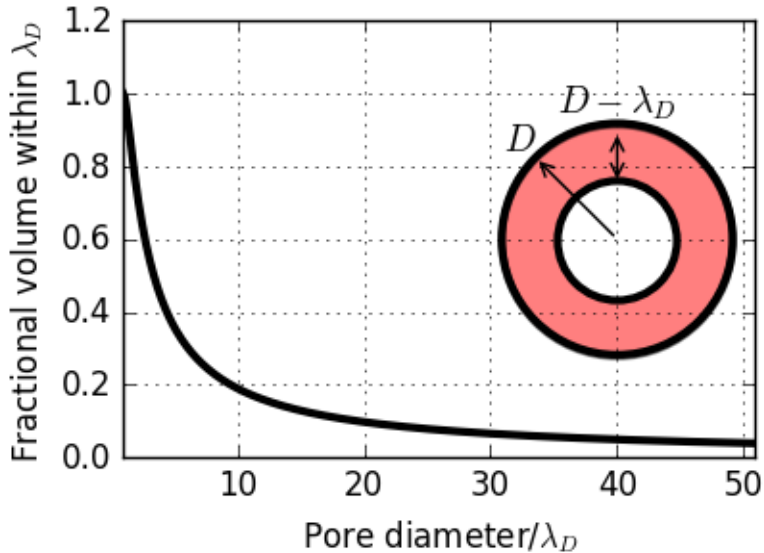


Figure 1.4: Plot of fraction of volume in a nanopore that is within the EDL versus pore diameter. The plot reveals a large super linear increase of total solution within the EDL as diameter decreases, starting at approximately $D \approx 10\lambda_D$.

area of pore contained within λ_D of the pore wall as a function of the pore diameter D .

For pores with diameter $D \gtrsim 10\lambda_D$, the total volume within the electrical double layer is negligible; however, below approximately $10\lambda_D$ the total volume within the EDL quickly increases. This explains why the ‘nano’ prefix in nanopore is important; as we approach the scale of the EDL, the structure of the solution very quickly changes, in a non-linear fashion, within the vicinity of a few nm of the pore wall.

In order to derive the appearance of the EDL, we consider the equations governing the distribution of ions in solution. In the solution, the ion species i have an electrostatic potential energy $U_i = z_i e \phi$, and have the following distribution in accordance with Boltzmann statistics

$$c_i = c_{0,i} e^{-\frac{z_i e \phi}{k_B T}}. \quad (1.5)$$

The electric potential itself is given by the Poisson equation

$$\begin{aligned}\nabla^2\phi &= -\frac{\rho}{\epsilon} \\ \nabla^2\phi &= -\frac{1}{\epsilon} \sum_i z_i e c_i(y).\end{aligned}\tag{1.6}$$

Plugging the concentrations given by the Boltzmann equation into the Poisson equation, we arrive at the Poisson-Boltzmann equation

$$\nabla^2\phi = -\frac{1}{\epsilon} \sum_i z_i e c_{0,i} e^{-\frac{z_i e \phi}{k_B T}}.\tag{1.7}$$

The Poisson-Boltzmann equation 1.7 is a second order non-linear differential equation for the electrostatic potential ϕ ; after solving for ϕ , it can be plugged back into the Poisson equation 1.6 to obtain the ion concentrations c_i . The Poisson-Boltzmann equation is generally solved numerically, but analytic solutions exist for simplified assumptions about the geometry and magnitude of the electrostatic potential in the solution.

Consider a planar surface with unit normal pointing in the \hat{y} -direction and uniform surface charge density σ immersed in a solution of water and symmetric ions with molar concentration c_{\pm} , valency $z_{\pm} = z$, and identical diffusion coefficients D_i ; this ion configuration is a close approximation of a KCl electrolyte solution, a common-used electrolyte in nanopore experiments due to the near-perfect symmetry of the ions. The ions have electrostatic potential energy given by $U_i = z_i e \phi(y)$ where the electric potential ϕ is only a function of distance from the wall due to the system's symmetry. Under these assumptions, the Poisson-Boltzmann equation becomes

$$\frac{d^2\phi}{dy^2} = -\frac{zec_0}{\epsilon}.$$

Though the solution can be solved analytically, a simple solution is obtained when we linearize the right hand side of the equation under the assumption $zec_0 \ll k_B T$ and apply the correct boundary conditions, an approximation known as the Debye-Hückel approximation. The solution is

$$\begin{aligned}\phi &= \phi_0 e^{-\frac{y}{\lambda_D}} \\ c_i &= c_{i,0} e^{-\frac{z_i e \phi_0}{k_B T} e^{-y/\lambda_D}} \\ \lambda_D &= \sqrt{\frac{\epsilon k_B T}{2c_0}} z,\end{aligned}\tag{1.8}$$

where we introduced a new parameter, the Debye length λ_D . The solution to the 1-D linearized Poisson-Boltzmann equation reveals that the electrostatic potential exponentially approaches 0 from the wall, that the counterion species are enriched at the surface and diminish towards the bulk, and the coions are diminished at the surface, but recover their concentration towards the bulk. The Debye length is perhaps the most useful parameter in nanopore systems since it gives a characteristic length scale for the region within the pore wall that departs from its bulk, ordinary behavior. The Debye length increases with dilute ion concentrations and decreases as the ion concentration is increased, and is typically somewhere in the range of 0.1–10 nm for common solution preparations. Note that although we discussed the electrical double layer here in the context of a pore surface, nearly every body immersed in solution will have some surface charge and therefore its own electrical double layer. The electrical double layers of free-bodies i.e. particles are integral in explaining

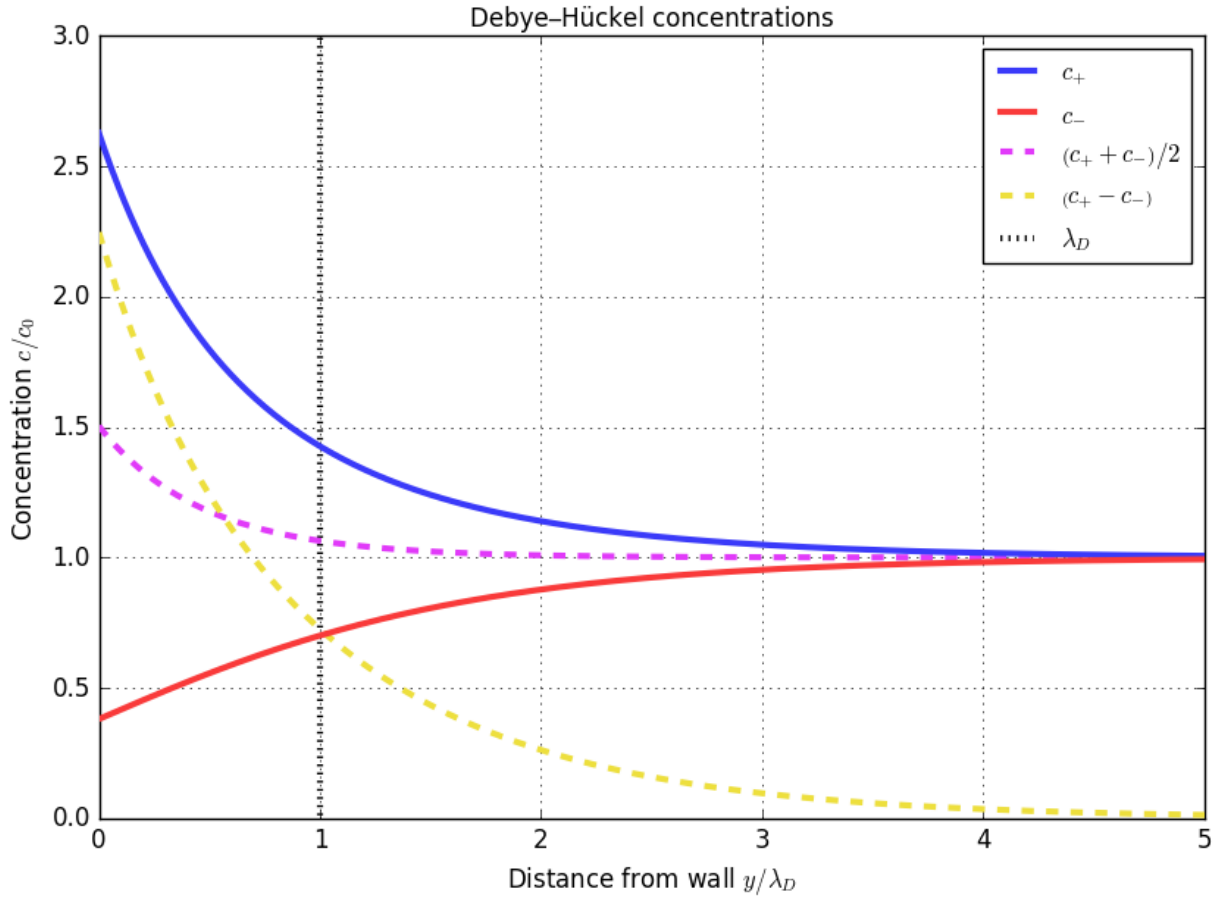


Figure 1.5: **Ion concentrations adjacent to a negatively charged surface according to the Debye-Hückel theory.** The plot reveals that the counterion concentration (blue) is enhanced near the wall, and decays approximately exponentially as distance from the wall increases. Oppositely, coions (red) are diminished near the wall, and rise to their bulk value with distance from the wall. The *total* ion concentration at the pore surface is slightly higher than the total ion concentration in the bulk. The space charge density $\rho_E \propto [c_+(y) - c_-(y)]$ is non-zero near the wall, and decays to zero in the bulk.

their motion in applied electrical fields, also known as electrophoresis.

The importance of the EDL in bestowing nanopores with their novel conductance properties cannot be overstated, and accordingly there are many phenomenon that nanopores that exhibit that are a direct consequence of the presence of the EDL. In the next few sections we will review some of these phenomena.

1.2.8 Electroosmosis

Ions migrate in externally applied electric fields, and ions of opposite polarity travel in opposite directions. When ions move, they tend to drag fluid along with them. In the bulk, this fact results in no net motion of fluid because for every anion that drags fluid towards the cathode, there is a cation that drags fluid towards the anode, and the two motions cancel each other out so that there is no net motion of fluid. However, as we've just learned there *is* a net concentration of one ion polarity in the EDL, so we expect that an electric field applied parallel to a charged surface will induce motion of the fluid. This intuition turns out to be correct, and the effect is known as electroosmosis. Interestingly, although the effect originates due to the presence of the $\sim 1\text{ nm}$ -thick EDL, the induced fluid flow propagates well into the bulk, and electroosmosis is observable in micro- and even milli-sized systems. This result, while surprising, is due to the simple viscous coupling of the fluid at the EDL surface to the rest of the fluid.

Because electroosmosis induces a general fluid flow, the effect couples with the motion of all unbound actors in the system, namely the ions species and any particles suspended in the solution. In typical nanopores, convection in the electroosmotic flow tends to be less pronounced than migration in the electric field. However, some lightly charged particles for instance will only experience a small force from the electric field (electrophoresis) compared to the drag force from the fluid moving electroosmotically, and their motion is therefore

determined primarily by electroosmosis. For the case of ions, usually the electroosmotic convective velocity adds or subtracts only a small offset to their net total motion, which remains dominated by electrophoresis. However, recently it was shown that some types of channels exhibit frictionless flow of water, and in these cases the electroosmotic velocities can become very large. In these channels it is actually expected that electroosmotic offers a large, if not dominant contribution to the motion of ions in the system. One example of these special types of pores, carbon nanotube pores, will be discussed later in this dissertation.

To understand electroosmosis, we look to the Navier-Stokes equations which describe the motion of fluids, and the Poisson-Boltzmann equation which yields the distribution of ions in the vicinity of the EDL. As an example, consider again an infinite charged plane with unit normal pointing in the \hat{y} - direction, but this time with a constant electric field \vec{E} applied parallel to its surface. The Navier-Stokes equation (eq 1.2) simplifies greatly in this case, and simply becomes

$$0 = \eta \frac{\partial^2 u}{\partial y^2} + [c_+(y) - c_-(y)] z e E_{ext}.$$

The equation shows that there is a momentum flux source term from the electric field acting on the charged solution in the EDL, which is proportional to the net charge in the solution (proportional to $c_+ - c_-$) times the electric field \vec{E} . The other term that balances the driving force is due to viscous forces between neighboring layers that have different y - velocities u , i.e. due to velocity gradients perpendicular to the wall. In order to solve this equation, we can replace the charge density $\rho_E = z e (c_+ - c_-)$ with the Laplacian of the scalar potential ϕ , integrate twice, and apply the correct boundary conditions, that the velocity at the pore wall is 0 (the so-called ‘non-slip’ boundary condition) and that the velocity gradients are 0 infinitely far from the wall. Performing these steps, we find the fluid velocity equals

$$u = \frac{\epsilon E_{ext}}{\eta} (\phi - \zeta),$$

where ϕ_0 is the electric potential immediately outside the surface charges on the pore wall. Interestingly, according to this equation the fluid velocity is proportional to the local electric potential in the screening layer, which is determined by solving the Poisson-Boltzmann equation (Eq. 1.7). Under the Debye-Hückel approximation of small surface potentials, the fluid velocity is zero at the walls, and exponentially approaches its bulk value as distance from the wall increases. This type of fluid flow profile is known as ‘plug flow’, since the velocity is approximately constant everywhere except in the thin EDL where there are sharp velocity gradients. Since the potential in the bulk is equal to $\phi = 0$, we find the bulk velocity to be equal to

$$u = -\frac{\epsilon \zeta}{\eta} E_{ext}$$

$$u = \mu_{EO} E_{ext}, \quad (1.9)$$

a result known as the Helmholtz-Smoluchowski equation. The parameter $\mu_{EO} \equiv -\frac{\epsilon \zeta}{\eta}$ introduced is known as the electroosmotic mobility, and is the proportionality constant between the applied electrical field and the resulting fluid velocity. Typical values of the mobility are $\mu_{EO} = 10^{-8} [m^2/Vs]$, which for an electric field of $1 V/\mu m^2$ yields a fluid velocity of approximately 1 cm/s .

Figure 1.6 shows the fluid flow profile in a pore with a finite slip length u_{slip} ; however, it must be noted that in the vast majority of experimental systems, $u_{\text{slip}} = 0$.

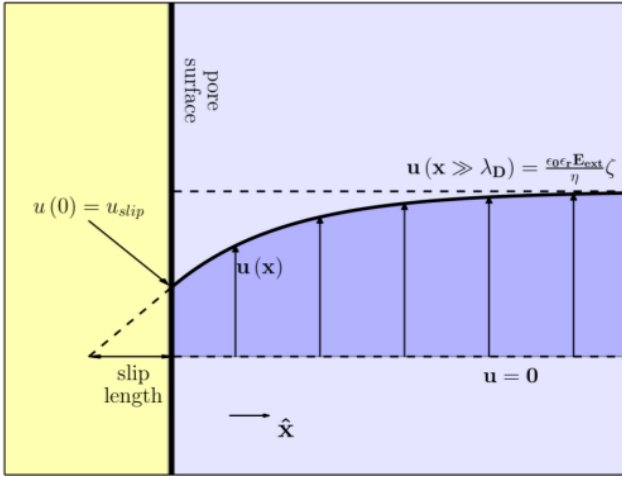


Figure 1.6: Plot of electroosmotic flow along an infinite plane with finite slip length. A net ion charge at the surface experiences a force in an electric field which drags fluid along with it. The force is only present in the electrical double layer, which viscously couples to the rest of the fluid. This fluid flow profile is known as plug flow, and extends far beyond the EDL where it originates.

It is possible to experimentally observe the fluid flow velocity, for instance by tracking the motion of small particles that move in the fluid flow, and therefore Eq. 1.9 provides a means for directly measuring the ζ -potential.

1.2.9 Surface conductance and conductance saturation

Ignoring electrical double layer effects, the conductance of an ion channel is proportional to the ion concentration in the solution; doubling the ion concentration exactly doubles the measured current. However, the presence of the electrical double layer breaks this perfect linear conductance relationship for two reasons. First, the integrated *excess* ion count $\int_0^{EDL} [(c_+ + c_-) - 2c_0] dy$ in the EDL layer is not guaranteed to be the same as the total ion concentration in the bulk; in fact, in most cases it is slightly higher, meaning the electrophoretic current in the EDL is slightly higher than in the bulk. Another important contribution to the measured current is the current from convection due to electroosmosis; because there is a net charge density in the fluid, electroosmosis will create a measurable

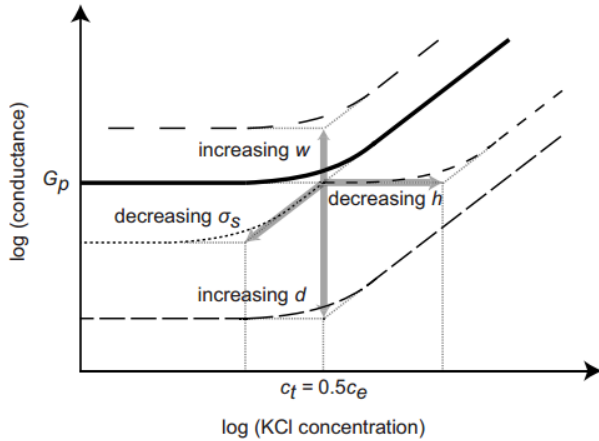


Figure 1.7: Reprinted (abstract/excerpt/figure) with permission from [(FULL REFERENCE CITATION) as follows: Author's Names, APS Journal Title, Volume Number, Page Number and Year of Publication.] Copyright (YEAR) by the American Physical Society.

ion current! In total, there are three terms that contribute to the total current measured in a channel, migration of ions in the bulk, migration of the integrated ion *excess* in the EDL, and net convection of charge in the EDL due to electroosmosis. Without applying any equations, we can use what we learned about the EDL and some general logic to reason about what the current behavior should be in the limiting cases of very large ion concentration and very small ion concentration. The equation for the Debye-length is $\lambda_D \propto c_0^{-1/2}$; for very large ion concentration, the EDL should be negligible and therefore neither the effects of electroosmosis nor electrophoretic ion excess should be significant. At the other end of the scale, in the limit of nearly zero ions in the bulk we still must have charge neutrality in the pore, meaning a finite concentration of ions despite the bulk concentration being zero. In this case, the EDL fills the entire pore and the result is that the conductance is entirely due to the integrated excess and convective terms. This finite conductance at zero concentration is known as the *saturation current*. Therefore, as we increase the length of the EDL we expect the conductance discrepancy, the difference in bulk conductance versus conductance due to the two surface effects, to increase. The end result of all this is that the conductance is a non-linear function of ion concentration at sufficiently low ion concentration; removing ions past some point does not further reduce the conductance of the channel! Consider a

nanopore immersed in solution of two symmetric ions denoted + and – (symmetric means their mobilities, valencies, and bulk concentrations are equal) with electrophoretic mobility μ_{EP} and electroosmotic mobility μ_{EO} . The following expression breaks down the total measured current into the three components described above:

$$I = I_{\text{bulk}} + I_{\text{excess}} + I_{\text{EO}}$$

$$I = \int 2c_0\mu_{EP}EezdA + \int [c_+(z) + c_-(z) - 2c_0]\mu_{EP}EezdA + \int [c_+(z) - c_-(z)]u_{\text{EO}}(z)ezdA. \quad (1.10)$$

Figure 1.7 shows a plot of the conductance versus solution concentration for a nanopore; the plot reveals a saturation at low solution concentration as expected from the preceding arguments. The saturation current is equal to the surface conductance term in the above equation.

1.2.10 Ion selectivity

A phenomenon related to surface conductance is *ion selectivity*. Since the EDL has a higher concentration of counterions rather than coions, the total flux of ions through the pore is slightly skewed towards counterions. The ion selectivity is defined as

$$S = \frac{|I_+ - I_-|}{I}. \quad (1.11)$$

1.2.11 Ionic current rectification

An ion channel is said to be rectifying if its conductance for one voltage polarity is greater than the opposite voltage polarity. The presence of an EDL alone cannot account for this, since the system has symmetry with respect to switching the electrodes, and therefore no rectification will occur. However, by introducing asymmetry into a system, along with having the pore be partially ion selective, we can create rectifying pores. There are many ways to create asymmetric nanopores, but two obvious solutions are geometry and surface charge pattern based.

If the shape of a nanopore is asymmetric, for instance as in a cone, the ionic current will be rectified. A simple explanation for this is that at the tip-side of the pore (in the case of conical nanopores), there will be an excess of counterions in the vicinity of the entrance EDL, while the other side will more closely resemble the bulk. Because these ions are at the entrance of the pore, they will more easily enter the pore than when at the other side. The result is that for one voltage polarity the ionic current is greater than at the opposite polarity.

By similar reasoning, charge patterning asymmetry can also lead to rectification. By placing two charges of opposite polarity adjacent to one another inside the pore, for one voltage polarity a depletion zone is created in analogy with the depletion zone formed between the n- and p-doped regions in a semiconductor diode. The ionic current is rectified, and because the diode junction so severely limits the ionic current under one voltage polarity, the device is said to be equivalent to an ionic diode.[10]

Figure 1.8 shows a conical nanopore with a bipolar charge distribution. The combination of the geometrical and charge asymmetry gives the pore a very large rectification value, and the near-zero current for one polarity of voltage is enough to consider the pore a diode.

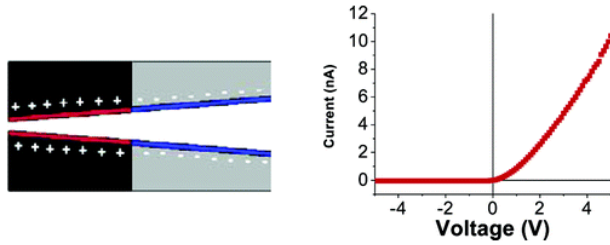


Figure 1.8: An ionic diode formed in a conical nanopore with bipolar surface charge patterning. The region between negative and positive charges is the depletion zone, and provides a large resistance to ion flow through the pore for one voltage polarity. Reprinted with permission from I. Vlassiouk and Z. S. Siwy. Nanofluidic diode. *Nano Lett.*, 7(3):552–556, 2007. PMID: 17311462. Copyright 2007 American Chemical Society.

Particle electrophoresis

Electrophoresis is the transport of a charged particle in the presence of an electric field. The effect of electrophoresis can be derived much in the way electroosmosis was derived, but instead of considering the fluid flow velocity at the surface of the particle to be zero, we set it equal to the electrophoretic velocity. For particles with thin electrical double layers (Debye-Hückel approximation) and laminar flow (Stoke's flow), the particle velocity is

$$\vec{u} = \frac{\epsilon \vec{E}_0}{\eta} \phi_0 \quad (1.12)$$

$$\vec{u} = \mu_{EP} = \frac{\epsilon \phi_0}{\eta}.$$

In equation 1.12, we've again introduced a proportionality factor between the applied electric field E_0 and the induced velocity \vec{u} ; this factor is known as the electrophoretic mobility. However, these equations are derived under the assumption that the applied electric field does not perturb the distribution of ions in the electrical double layer, which is only true for small surface potentials. If this assumption is invalid, additional effects related to the redistribution of ions must be taken into account; the net effect is a retarding force on the particle that slows its velocity.

Electrophoresis is an important effect in many applications involving particles. One useful application is that particle electrophoresis through a nanopore can be used to measure the zeta potential of a particle, related to its surface chemistry and chemical adsorption. An electric field is applied across a nanopore which is immersed in electrolyte solution containing ions and charged particles. Particles travel through the pore under electrophoresis, and the dwell time can be recorded using resistive pulse sensing or optical techniques. If the geometry of the pore is known, the dwell time can be related with the particle velocity, and the electric field strength can be determined as well. In this case, equation 1.12 can be solved for the surface potential ϕ_0 , which is the same as its zeta-potential.

Particle electrophoresis + electroosmosis

Transport of particles is in general a superposition of electrophoretic and electroosmotic effects. Combining the two, the velocity of a charged particle translocating through a charged pore is

$$\begin{aligned} v &= (\mu_{EP} + \mu_{EO}) E, \\ v &= \frac{\epsilon}{\eta} (\zeta_{\text{particle}} - \zeta_{\text{pore}}) E \end{aligned} \tag{1.13}$$

In general the net velocity can be positive, negative, or zero depending on the relative sizes and signs of the electrophoretic mobility.

Chapter 2

Development and testing of a single carbon nanotube based pore

2.1 Background

This chapter describes my research performed on measuring the ion, water, and particle transport properties of single carbon nanotubes. A carbon nanotube (CNT) is a cylindrically-shaped monolayer of carbon atoms, and because of its shape it can effectively act as a nanopore. When used as nanopores, CNTs are thought to exhibit behavior that is significantly different than traditional nanopores, including large fluxes of water, large fluxes of some ion species, steric rejection of other ion species, ultra-high proton mobilities, and an unusual sub-linear power law in the conductance-concentration relationship. These effects are poorly understood, and since it was discovered that they could be used as single nanopores many labs around the world have worked on understanding them. Besides being poorly understood, there is even a lack of consensus in the field about whether some of these properties are even real! The objective of this experiment was to test a new CNT platform

that could help point the field in the right direction; by observing transport phenomena in our CNT platform, hopefully we nudged the field in the direction of a concensus.

In the following sections, I will explain in greater depth a functional CNT nanopore platform, and the physical reasons underlying their novel transport characteristics.

Chapter 3

Experimental study of ion conductance property of hybrid conductor-insulator nanopores

3.1 Background

In the introduction of this thesis we discussed the electrical double layer (EDL) which is a screening layer of ions that forms in the proximity of a charged surface. The vast majority of pores studied are non-conductive insulators, and their surface charge properties come from the functionalization of chemical groups at their surface. For instance, the base of the pore studied in this section is Si₃N₄ (silicon nitride), whose native silane chemistry means there are exposed alcohols at the surface that are either negative or neutral depending on pH. However, charge on a surface can arise *via* other means. When a metal is exposed to an electric field, electrons in the metal rapidly redistribute themselves on the surface to cancel the external applied field. If we assume the metal was originally overall neutral, the

charge pattern will consist of an abundance of negatively-charged electrons at one end and an abundance of positively-charged holes at the other. A natural question is whether these *induced* charges have associated EDLs in the same way that static charges do.

Previous studies suggest they do. For instance, Squires *et al.* and Pascall *et al.* performed experiments with applied external electric fields on various metal surfaces and discovered that electroosmotic flow occurred. They reasoned that electroosmosis was a result of polarization of charges according to the model discussed above [9, 6]. However, these types of induced-charges have been seldom discussed in the context of nanopore transport, especially in the context of a realizable experimental platform. In order to understand the effect of induced charges on nanopore transport, we considered a hybrid metal-insulator pore created by evaporating a thin layer of gold onto the pore surface. If the pore was only the insulator, its IV curve would be symmetrical due to the lack of any symmetry breaking in the system. The addition of the metallic layer breaks this symmetry, and we expect to see ionic current rectification in the pore (see chapter 1.) However, ionic current rectification alone is insufficient for proving that induced surface charges contribute to the pore's conductance; this is because essentially *any* symmetry breaking in a pore, including a difference in static surface charges between two regions, a difference in geometrical shape between two regions, or induced surface charges, will lead to ionic current rectification.

In order to provide evidence that induced charges directly contributed to a pore's conductance properties in this system, we need to devise a model for the manner of the induced rectification properties, and to check if the model accurately describes experimental data. Figure 3.1 is a scheme of the induced-charge model, which is effectively explained by the surface charges present. First, the insulating part of the pore has an approximately uniform surface charge due to ionization of the chemical groups on its surface. On the gold, the charge patterning depends on the applied voltage. When a negative bias is applied on the gold side of the pore, electrons are repelled from the electrode while holes are attracted. The

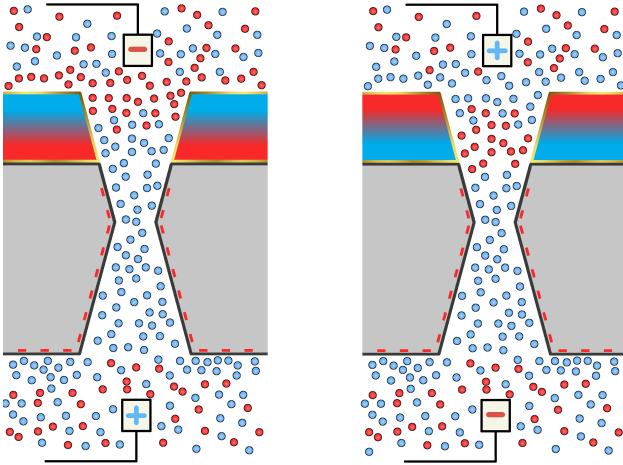


Figure 3.1: Model for the induced-charge and EDL charges in the hybrid conductor-insulator nanopore. **Left:** Negative bias applied to gold side. **Right:** Positive bias applied to gold side. For the positive bias, a depletion zone forms at the junction between the gold and SiN, which is expected to severely limit the conductance. For the negative bias, no depletion zone forms and therefore the conductance is expected to be unhindered. The double conical geometry reflects the expected geometry of SiN pores drilled *via* a transmission electron microscope electron beam.

charge pattern in the solution from top to bottom is then $- + +$. On the other hand, when a positive bias is applied on the gold-side of the pore, holes flee to the inside of the pore while electrons are drawn towards the electrode. Therefore, from the positive electrode to the negative electrode the surface charge pattern is $+ - +$ (right hand side of figure 3.1). The primary difference in the charge pattern as it relates to the influence on the nanopore between the two voltage polarity cases is the charge junction at the conductor-insulator interface; in the latter case (positive voltage applied on the metallic side), the $+ -$ junction indicates the presence of a bipolar junction that leads to a depletion zone in the EDL, as discussed in the section on ionic current rectification in chapter 1. This depletion zone is characterized by having a very large resistance, and therefore limits the total current through the pore. For the opposite polarity, the depletion zone is not present and therefore we do not expect any significant limiting of the current.

This model, known as the induced-charge model for hybrid conductor-insulator nanopores, was tested experimentally in this work.

3.2 Experimental setup

In order to test the induced-charge model, we devised a platform consisting of thin nanopores in silicon nitride (SiN) with gold (Au) deposited on top. The crucial elements of this setup consisted of the silicon nitride (SiN) membrane, evaporated gold (Au) layer, transmission electron microscope drilling of the pore, and the current-voltage characterization measurements.

3.2.1 Silicon nitride

Silicon nitride was used as the substrate through which to drill the nanopore. The effects of polarization of the gold should be apparent in truly nano-scale systems, so it was important to choose a material through which a small pore could be fabricated. As of the writing of this thesis, silicon nitride (chemical formula Si_3N_4) is a popular choice for creating small nanopores given its mechanical stability and well-understood surface chemistry. The method of pore formation, TEM drilling (discussed below) can enable pores ranging from 1 – 20 nm in diameter, and is capable of drilling through substrate lengths of up to 100 nm. It is predicted that pores with very low aspect ratios, i.e. short pores, will have severely diminished rectification properties. In order to ensure large rectification, the solution must be subjected to a sufficient length of EDL. In order to strike a compromise between TEM's capabilities and the undesirable low-aspect ratio effects, a substrate thickness of 50 nm was chosen. The silicon nitride substrate is commonly used in TEM microscopy, and therefore is available from commercial vendors. The substrates were ordered from the SPI company. The substrate itself is grown onto a thicker layer of silicon, through which a window is drilled on the backside to expose the silicon nitride. The final result is a 50 nm thick layer of SiN supported by a silicon chip. After pore fabrication, silanol groups native to the pore surface act as surface charges if immersed in solution with pH beyond their pKa value of

3.2.2 Gold deposition

Although the model of induced-charge rectification described above is independent of the type of conductor used, we chose to use gold (Au) because of its mechanical stability after deposition and its resistance to corrosion and oxidation, which could create a surface chemistry effect that could potentially obscure the relationship with the induced surface charges. With the conductor's material chosen, we think about the desired deposition thickness. In the model of induced-charge rectification described above, it is necessary to have a bipolar junction far enough inside the pore that a depletion layer can form. For this reason, we aimed to deposit a 30 nm layer of gold onto the surface of the SiN. There are a number of means of depositing metals onto surfaces, but given the thinness of the desired layer we chose to deposit *via* an e-beam evaporation. During e-beam evaporation, a chunk of metal is pumped down in vacuum and bombarded with high-energy electrons. The combination of low-pressure and large temperature caused by the bombardment with the electrons causes individual metal atoms to evaporate from the surface of the chunk along straight-line or ray paths. The atoms then hit the surface of the substrate, which is suspended above it, and stick. Although Au *can* be deposited directly onto the surface of SiN, a thin layer (3 nm) of chromium (Cr) was first evaporated, which facilitates adhesion of the Au.

3.2.3 Transmission electron microscope drilling

The transmission electron microscope (TEM) is a super resolution imaging technique that is typically used to image objects below the optical diffraction limit of 200 nm. However, if the electron beam is sufficiently energized and focused, the electron beam can act as a drill for forming nanopores instead of for imaging. This technique was used to drill pores through the SiN-Au hybrid device described in the above two steps. A highly focused beam in the TEM's scanning (S) mode is applied to the surface. The energetic electrons strike the

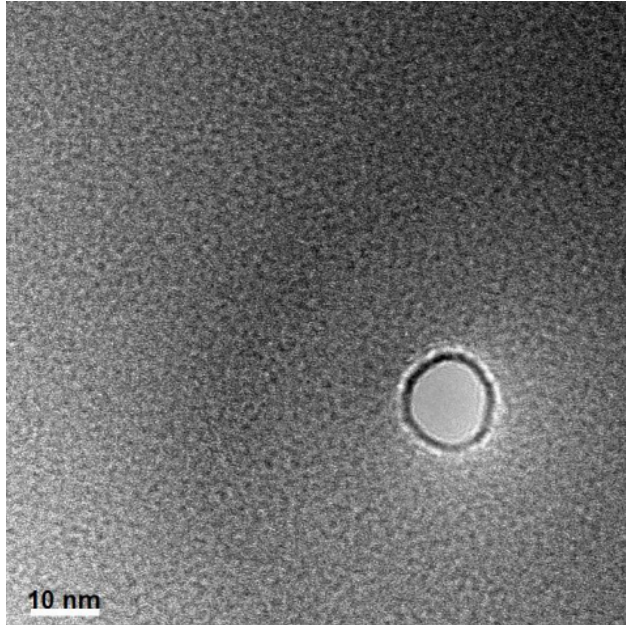


Figure 3.2: A ~ 15 nm SiN pore drilled *via* TEM.

surface and eject atoms, while simultaneously the entire structure melts. The final result is a pore with the same thickness as the substrate, and with a double conical geometry which is a result of the simultaneous ballistic ejection and melting. Because the drilling is performed inside the TEM, the resulting pore can also be immediately imaged. Figure 3.2 shows an example of a ~ 15 nm TEM-drilled pore.

3.2.4 Pore conductance characterization

In order to test the induced-charge model, we measured the current-voltage (IV) response of each of the fabricated nanopores in 100 and 500 mM KF and KCl salt solutions. The total surface charge of a pore ‘felt’ by the ions in the solution is given by a combination of the ionized chemical groups on its surface and any chemical species that are adsorbed to the surface. Cl is known to adsorb to the surface of gold, and so we expect that the gold in KCl solutions will have net charge given by the adsorbed chloride ions and the induced-charges. For this reason, measurements were performed primarily with KF solution. However, it

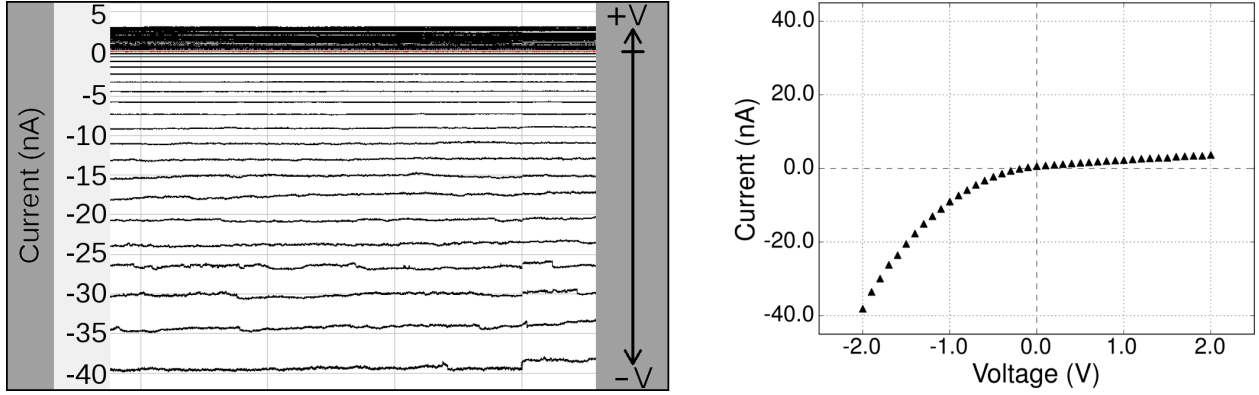


Figure 3.3: A current-voltage time series alongside the current-voltage curve produced from it. **Left:** Current-voltage time series. Each continuous line corresponds to one voltage setting; once a voltage value is set, the current does not significantly vary. **Right:** Traditional pore I-V curve. The asymmetry in the current with respect to voltage (present in both signals) is the hallmark indicator of ionic current rectification.

was predicted that adsorption of chloride on the Au surface would diminish the effects of the induced-charge, and this model was tested by performing measurements with KCl on chips that had already been measured in KF, to see if their conductance behavior changed according to this prescription.

Due to the small sizes of the pore and the low surface charge density of the silanols on the SiN surface, the interior of the pore is difficult to wet, meaning any vapor present inside the pore can be stable and difficult to remove. If this is the case, ions cannot pass through. Often times these vapor phases are quasi-stable and the pore will spontaneously wet and dewet. In order to reduce these hydrophobic effects, we use an even 50/50 mixture of water and ethanol solvent; the combination of both solvents promotes wetting of the pore.

In principle, during IV measurements one needs only to sweep the voltage along the desired range, stopping to record the current at each voltage value. Usually one delays ~ 1 second after changing the voltage before a current measurement is made to allow for the system to equilibrate, e.g. due to system capacitance charging/discharging. However, in systems in which the system conductance can stochastically change, e.g. due to spontaneous wetting/dewetting transitions, it is advantageous to record a time series of the current voltage

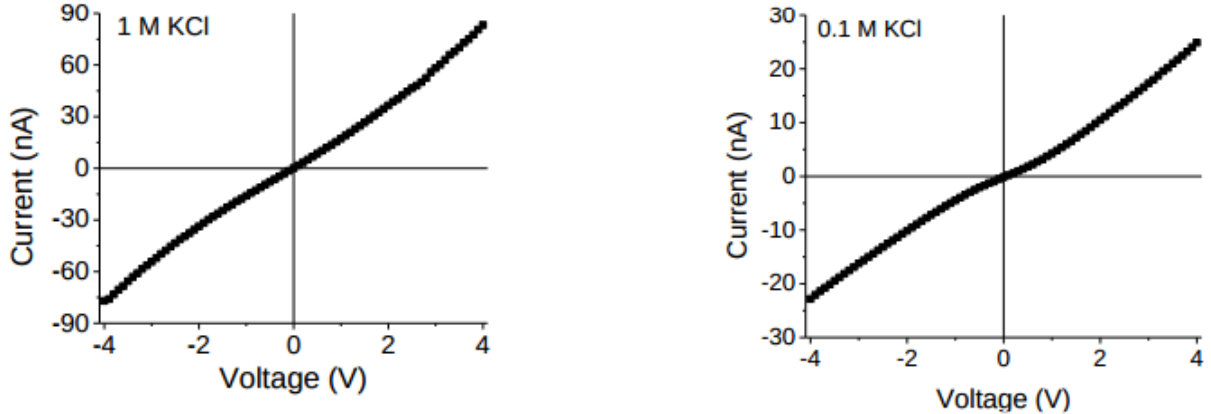


Figure 3.4: **IV curves taken of bare SiN pores.** The symmetry in the IV curve reveals no inherent rectification of the TEM drilled pores.

sweeps rather than measure single data points. If a transition occurs, it can be observed in the time series of the signal and appropriately dealt with afterwards. The protocol for measuring IV curves is then to apply a fixed voltage, record the current for a fixed amount of time, and repeat for all of the desired voltages. Then, an IV curve is produced by averaging the current time-series for a fixed interval of time (averaging is performed to smooth over the small amount of noise in the signal). In this study, voltages were applied for a total of 20 s and the current values in the last 0.5 s were averaged to create the current measurement value. Figure 3.3 shows an example current-voltage time series and the IV curve produced from it for one of the pores used in the study measured in KF solution. On the left is a current-voltage time series plot that shows the current value time series for different voltage settings, while the right hand side of the figure shows a traditional I-V curve of the pore.

3.3 Experimental results

A number of conductor-insulator pores were tested, along with plain SiN pores to test of the pores intrinsically rectify the current (e.g. due to a geometrical asymmetry).

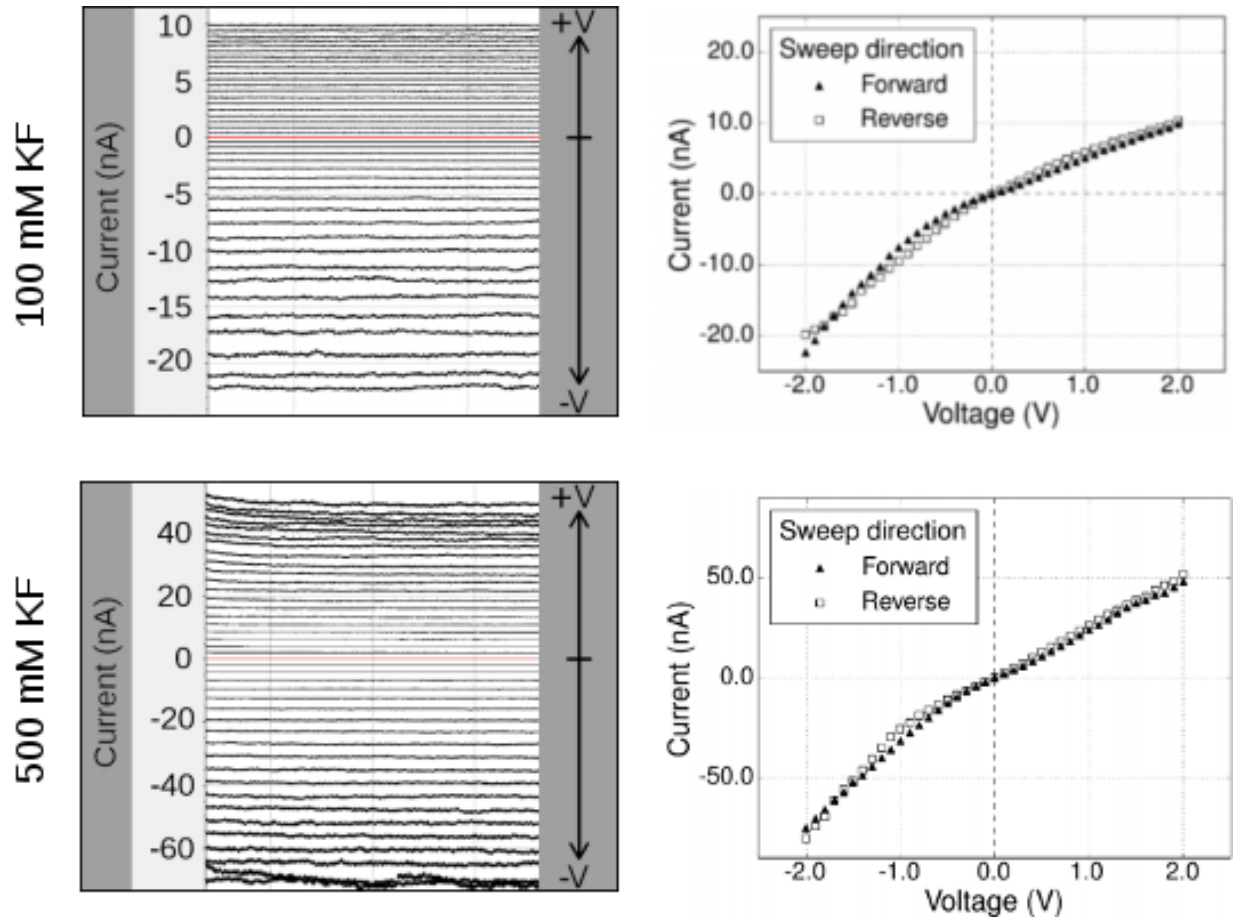


Figure 3.5: **IV curves taken of Au-SiN pore in 100 mM and 500 mM KF.** The symmetry in the IV curve reveals no inherent rectification of the TEM drilled pores. The ion rectification ratio R is lower in the higher concentration solution, as is expected from basic considerations of EDL thickness.

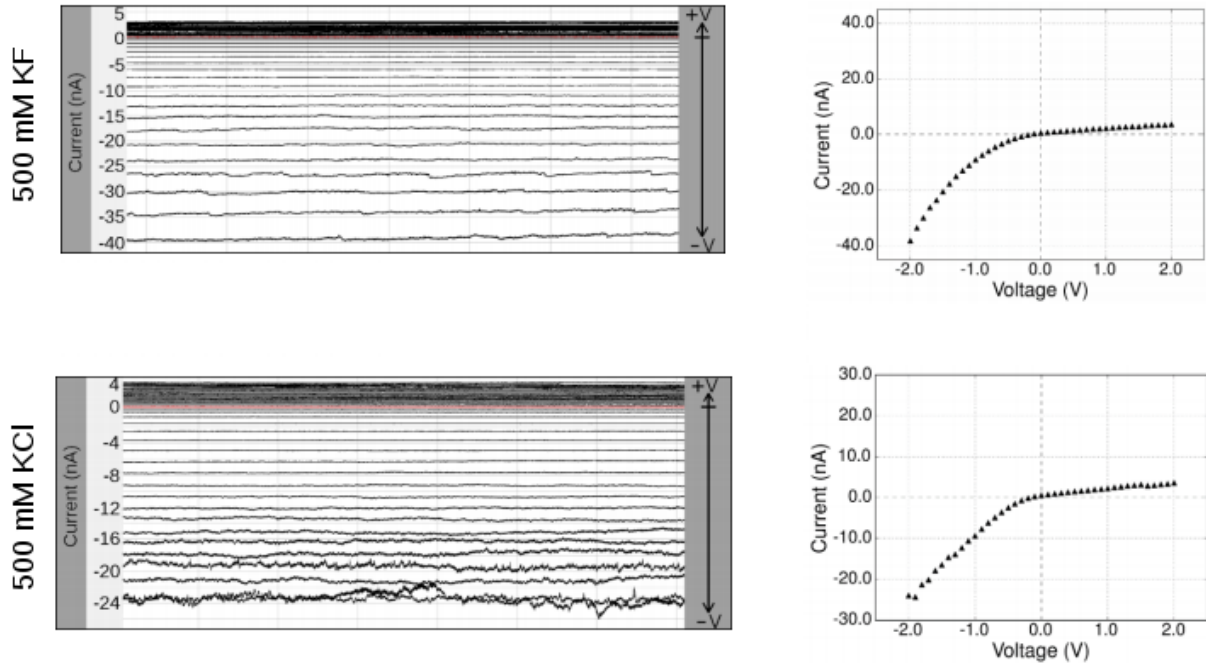


Figure 3.6: **IV curves taken of Au-SiN pore in 500 mM KCl and KF.** The rectification ratio R is lower in the KCl solution than in the KF solution, which is expected due to the additional contribution of the static charge from adsorbed Cl^- ions on the gold surface.

Figure 3.4 shows two IV curves gathered for the SiN-only (insulator pore only). The plot shows approximately symmetric IV curves, indicating a symmetric nanopore.

On the other hand, figure 3.5 shows two IV curves collected for a single nanopore approximately 9 nm in diameter. The IV curves taken in KF show significant rectification, with a ratio of approximately $R = 0.5$ for the 100 mM concentration and $R = 0.7$ for the 500 mM KF concentration. The increase in rectification R towards $R = 1$ with increasing salt concentration is consistent with the decrease in thickness of the EDL. In the model we developed for the induced-charge rectification, a depletion region is expected to form in the interior of the pore. Typically pores that have depletion zones experience much greater rectifications due to the ‘off-state’ voltage polarity having nearly zero conductance. While this pore’s rectification is not small enough (e.g. not close to zero) to describe it as an ionic diode, the rectification direction is nevertheless consistent with the proposed model. We note that this direction of rectification is inconsistent with models having only static charges on the SiN

and Au, barring the case where the *Au* has positive charges adsorbed onto its surface, which is unexpected for the ion species used in this study.

In order to understand the effect of a static charge superimposed on top of the induced-charge, we next performed experiments in KCl in addition to KF. Figure 3.6 shows a 12 nm pore with IV curves measured in 500 mM concentration of both types of salts. Note that both salts give the same type of rectification as in the previous example. This result is not entirely unexpected, as the presence of adsorbed chloride will bring the two charges in the depletion zone closer together in magnitude, while still maintaining a finite, albeit reduced rectification. If the Cl^- ions adsorbed to the surface of the gold to the extent that they dominated both the induced-charge on the gold and the surface charge on the SiN, then it is possible the rectification direction could even flip direction such that $R > 1$. However, we did not observe such an effect.

3.4 Modelling results

In order to provide an additional line of evidence pointing to induced-charge based ion current rectification found in experiments, we performed finite-element analysis simulations using the COMSOL Multiphysics software package. The models were designed to emulate the experimental set up, e.g. the channel geometries and salt concentrations used were similar. However, rather than try to reproduce the double conical geometry expected for TEM drilled pores, we worked with a cylindrical geometry which greatly facilitated convergence of the solutions with the very minor penalty of not adhering exactly to the experimental conditions. Because the cone angle is expected to be shallow and because the COMSOL results are meant to be interpreted semi-quantitatively, and are primarily used to draw conclusions about the rectification direction and mechanism, replicating the exact geometry of the pore was deemed unnecessary. Details of the COMSOL simulation can be found in the appendix.

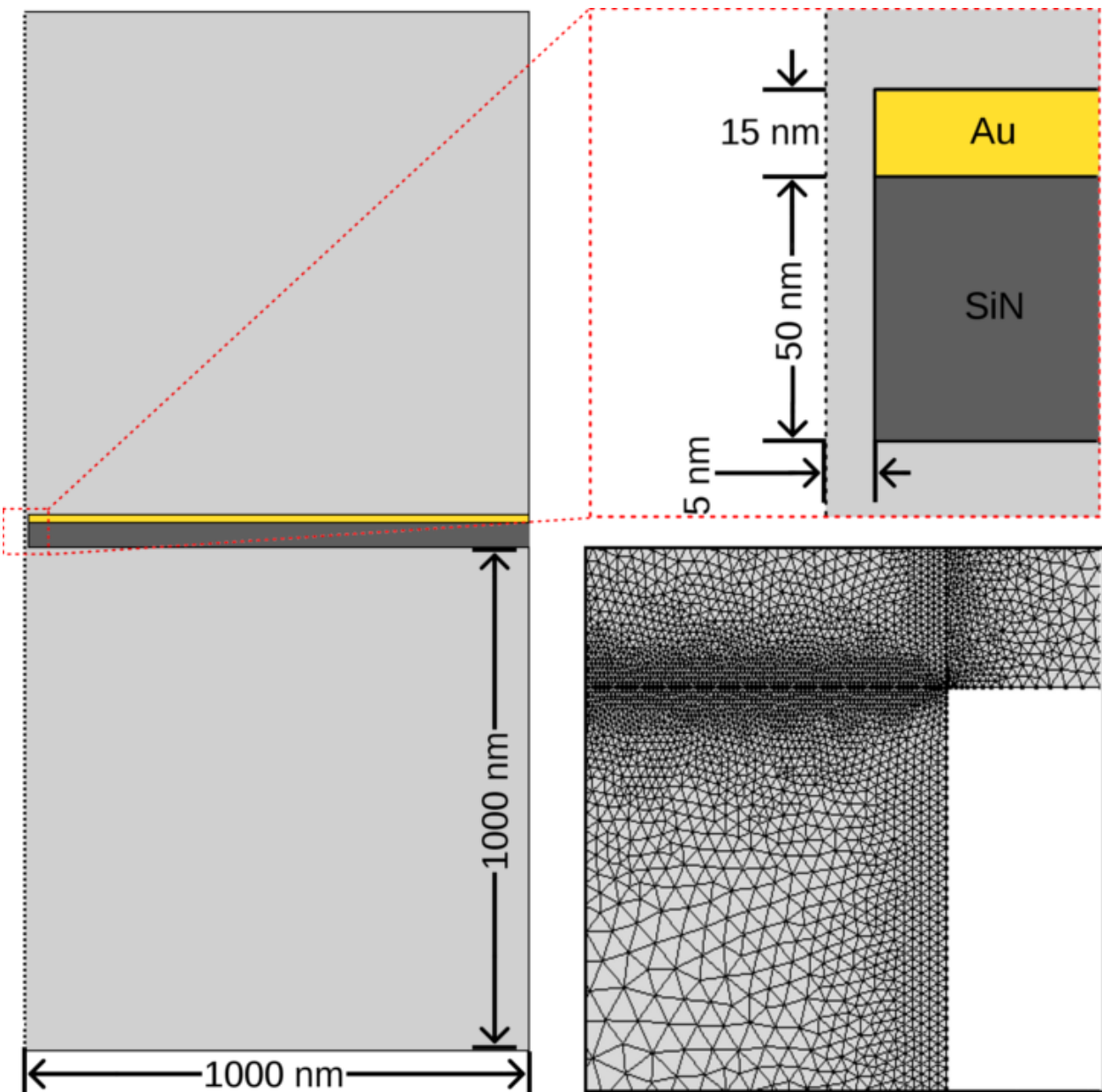


Figure 3.7: COMSOL simulations.

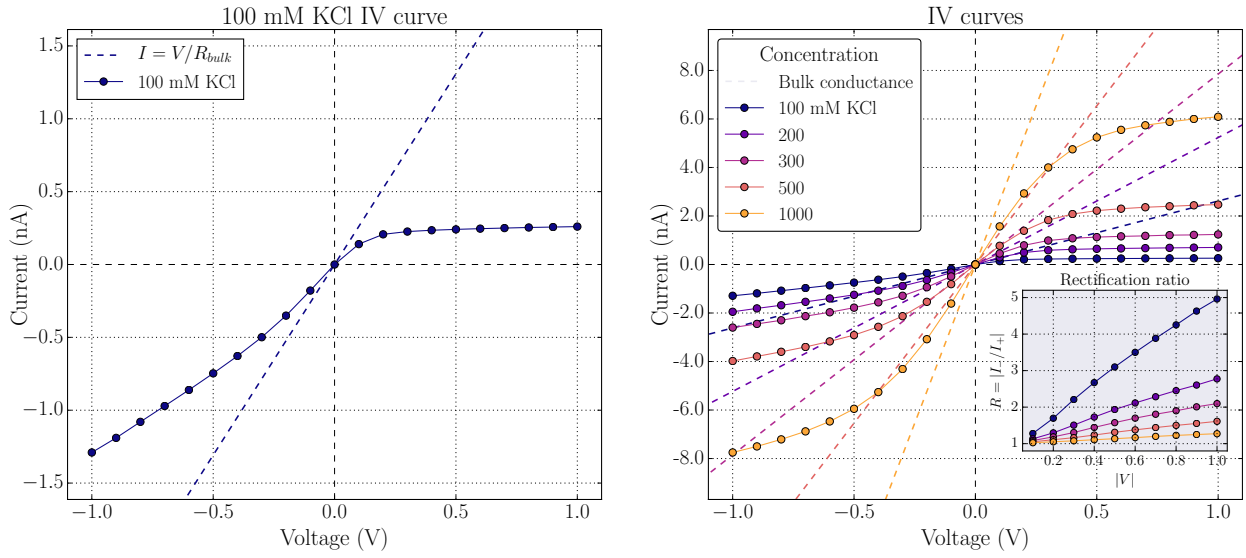


Figure 3.8: COMSOL simulations.

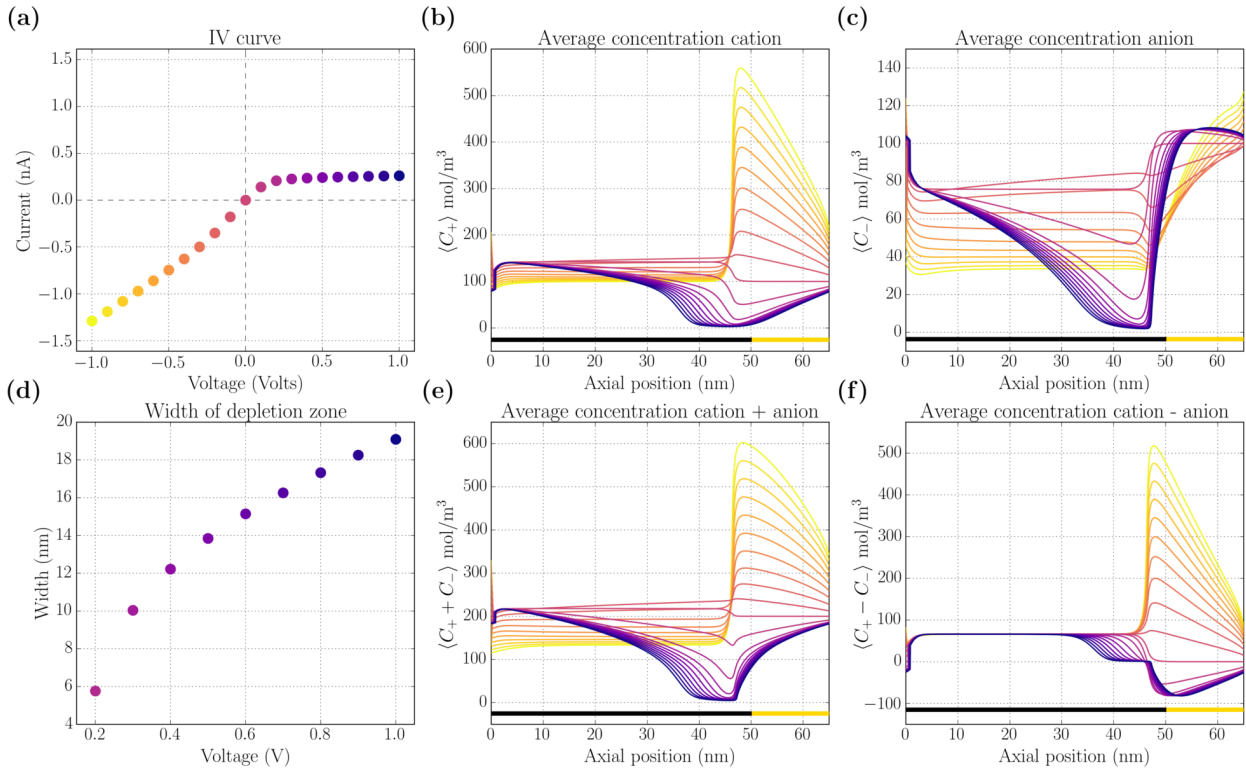


Figure 3.9: COMSOL simulations.

The results of the simulations are found in figures 3.8 and 3.9. We simulated IV curves for the model device and calculated the average concentrations of the cations, anions, and combinations at various axial positions inside the pore, and used these calculations to calculate the width of the depletion zone that forms for positive voltages. Figure 3.8 shows IV curves of the simulated pore at various concentrations. Notice htat at low concentrations the pore rectifies in the negative direction i.e. $R = |I_-/I_+| > 1$ and the rectification ratio R decreases with increasing electrolyte concentration, both results are consistent with the experimental data. Figure 3.9 shows the average concentrations of C_K , C_{Cl} , $C_K + C_{Cl}$ and $C_K - C_{Cl}$ at various axial positions. The concentrations of C_K and C_{Cl} along the length of the gold surface are consistent with the polarization model of gold: when a positive potential is applied on the side of the metal, electrons are drawn to the entrance of the pore, inducing formation of an EDL more positive than at the opposite terminal, and the opposite occurs for the opposite voltage. Along the length of the SiN far from the junction, the concentration of potassium is enhanced due to the negative charge of the surface, and fluoride is reduced. In the plot of $C_K + C_{Cl}$ which reflects the total ion concentration (bottom center), at positive voltages there is a drop in the concentration in the vicinity of the junction. In this region the total concentration is far below its bulk value, while elsewhere it is much closer to the bulk. This severely reduced charge density reflects the formation of the depletion zone, the zone created when ions near the diode junction are pulled apart. The resistivity $\rho \propto (C_K + C_{Cl})^{-1}$, so the depletion zone has a very large resistance and therefore limits the current through the pore as a whole. Depletion zone regions like the one that appears in the simulation severeliy limit current, which can be seen in the near 0 slope of the current for positive voltages in the IV curve. The current is limited by the depletion zone, and we identify this type of pore as a diode. The bottom-left plot of figure 3.9 shows the width of the depletion zone as a function of voltage. The depletion zone was defined as the width along the pore axis such that the total ion concentration is below half of the total ion concentration (in this case, below 100 mM, since $C_K = 100$ mM and $C_{Cl} = 100$ mM. While increasing the voltage

increases the current, the depletion zone is also widened with increasing voltage, resulting in a net sub-linear relationship between voltage and current at positive voltages.

The COMSOL results show that the model of induced-charge based electrical double layers is possible, and that the magnitude of the effect is enough to greatly influence the pore. Furthermore, the results show that the model system results in rectification ratio $R > 1$, in the same direction of the experiments' IV curves.

3.5 Conclusion & Future Work

The work presented in this chapter demonstrates the capabilities of conducting layers in affecting the ionic conductance properties of nanopore systems. We demonstrated, to our knowledge, the first instance of a conducting layer that actively modulates the current in a nanopore by depositing a thin layer of gold on top of a TEM-drilled SiN pore. In our model for our device, a dynamically induced charge acts in concert with the native, static ionized silane groups native to the SiN surface to create a diode-like rectification behavior. This type of rectification and its direction cannot be explained with static charges alone, and therefore we conclude that the induced charges on the gold layer were significant in contributing towards the total rectification of the device. Furthermore, numerical simulations using COMSOL multiphysics provided another line of evidence that the induced-charges contributed to the device's conductance. In the simulations, for the 'off-state' of the device at positive voltages there was a clear depletion zone in the channel, in agreement with our a priori expectations based on the physics of the device.

The ability to fabricate single nanopores with novel ion conductance properties is crucial in fabricating integrated ionic circuit devices. These non-trivial conductance properties are usually achieved *via* chemical modification or *via* or modification with biomolecules such as

DNA. However, this work has revealed another potential way of creating diode-like nanopores with the addition of permanent embedded metallic layers.

Chapter 4

Resistive pulse studies of aspherical mesoparticles

4.1 Background & Theory

In the introduction of this dissertation we introduced and explained the theory behind resistive pulse sensing, a particle characterization technique that works by monitoring the change in conductance of a nanopore as small particles pass through it. Probably the most important application of RP sensing is in measuring the sizes of particles. An analytic model was devised by DeBlois *et al.* to relate the size of a particle to its resistive pulse amplitude. The solution is essentially an electrostatics boundary-value problem: given an insulating particle inside a pore and a known externally applied voltage, calculate the electric field distribution inside the pore, and from the electric field distribution calculate the pore's expected resistance with the particle inside it. When this calculation is performed for spherical particles travelling along the axis of long cylindrical pores, the change in resistance or current is found

to be

$$\frac{\Delta R}{R_0} = \frac{\Delta I}{I_p} = \frac{4\rho D^3}{\pi d^4} \left[1 - 0.8 \left(\frac{d}{D} \right)^3 \right]. \quad (4.1)$$

Equation 4.1 is useful for relating the change in current—or resistance—to the diameter of spherical particles. However, it is very often the case that particles of interest are not spherical. For instance, many biomolecules such as viruses and proteins are poorly approximated as spheres, and are more rod-like in shape. In this case, the resistive pulse amplitude of on-axis translocations through a cylindrical pore is given by

$$\frac{\Delta R}{R_0} = [f_{\perp} + (f_{\parallel} - f_{\perp} \cos^2 \alpha)] \frac{v}{V}, \quad (4.2)$$

where f_{\perp} and f_{\parallel} are so called ‘shape-factors’, that depend on the particle’s major and minor axis lengths, α is the orientation of the particle with $\alpha = 0$ being axially aligned, and v and V are the volume of the particle and of the pore, respectively. Figure 4.1 shows a plot of the relative $\Delta I/I_p$ for various ellipsoids of the same volume but different axial lengths.

While equation 4.2 is useful for determining the volume of spheroidal particles from their resistive pulse amplitudes, it would be useful to devise a method for measuring the length of particles in addition to measuring their volumes as an additional physical marker for their identification in a sample.

Consider a pore with a rough, non-uniform interior. Due to the irregular interior, the channel cross sections will have a range of resistance values; for instance, a large cavity in the channel will have a smaller resistance than a more narrow constriction. If a very small particle travels

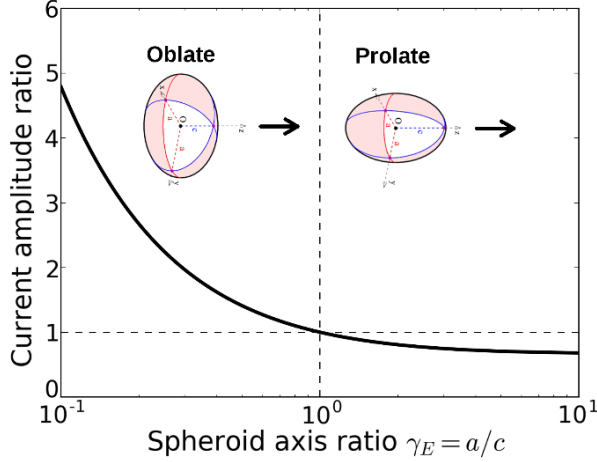


Figure 4.1: adsf

through the pore, its resistive pulse time-series is determined by the interior topology of the pore. For instance, when it happens to occupy a narrower region of the pore, the resistance in the region is larger relative to the rest of the pore, and therefore the particle will also block a relatively larger portion of the current. In this way, the particle is able to resolve the interior features of the pore. In such cases, the instantaneous resistive pulse amplitude is given by

$$\Delta R = R_p - R_0 = \frac{4\rho d^3}{\pi D^4} \left[1 - 0.8 \left(\frac{d}{D} \right)^3 \right]^{-1}. \quad (4.3)$$

$$\Delta R = \Delta R' = \int_{z=z'}^{z=z'+l} \frac{d\Delta R(z)}{dz} dz = \int_{z=z'}^{z=z'+l} \frac{4\rho d^3}{\pi D^4(z)} \left[1 - 0.8 \left(\frac{d}{D(z)} \right)^3 \right]^{-1} dz \quad (4.4)$$

Oppositely, if we consider a pore whose length extends along a significant amount of the pore's axis, it may be occupying several such regions at a time. Instead of a single particle,

we may consider the particle to be composed of many smaller segments of particles in series, and therefore the resistance values of each segment are additive. Therefore, the signals of longer particles can be seen as the convolution of the signal of an infinitesimally small particle over the long particle's length.

This fact can be used to devise an experiment that can measure the length of long particles. First, we drive a suspension of small ‘tracer’ spheres through a pore with rough interior, whose diameter is smaller than the characteristic length of the irregularities in the pore. These particles will ‘map’ the interior geometry of the pore as explained above, with resistive pulse shape given by equation 4.3. Then, we repeat the experiment with long particles for which we wish to know the length. Then we perform a convolution or moving average transformation of the signals of the tracer particles for a variety of lengths, given by the following equations:

$$I_i \rightarrow I_i^{l'} = \frac{1}{N} \sum_{j=i-\frac{N}{2}}^{j=i+\frac{N}{2}} I_j, \text{ and} \quad N = \frac{fl'}{v}, \quad (4.5)$$

where N is the total number of points in the moving average, I_i is the i th current measurement in the signal of the unprocessed short particle, $I_i^{l'}$ is the transformed data point for a moving average over length l' , f is the sampling frequency of the current acquisition instrument, and v is the *average* velocity of the particle during its translocation through the pore. However, equation 4.5 slightly oversamples particle positions in the middle of the moving average compared to particle positions at the very ends, along a distance equal to half the length of the small particle. For this reason, the moving average estimate of the correct transformation slightly overestimates the length of long particles. However, when $l \ll l'$, i.e. the tracer particle's displacement length is much less than the longer rod's displacement length, the effect is negligibly small.

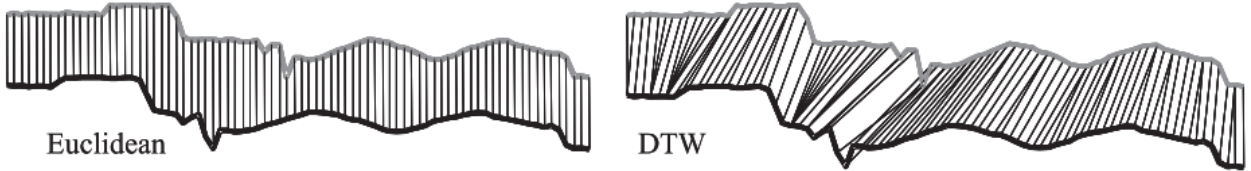


Figure 4.2: Comparison of standard Euclidean distance metric (left) and distance metric as determined by dynamic time warping (right). Notice that the Euclidean distance does not take into account small displacements of the two signals in time, despite their obvious similarity. On the other hand, dynamic time warping is able to account for small mismatches in time by finding the connections between points that minimizes the total cost.

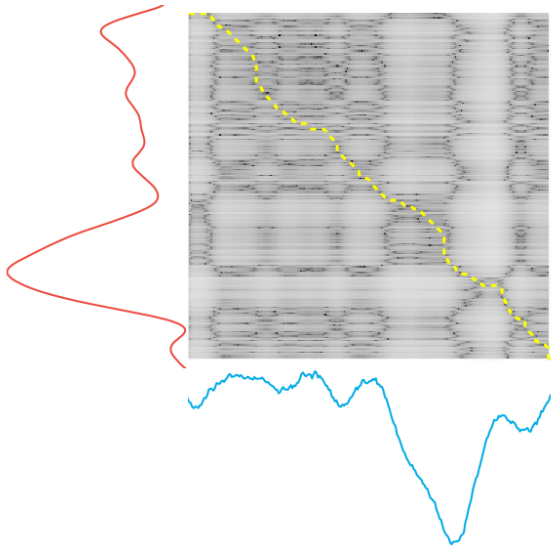
After computing the moving averages of the tracer particles over an array of lengths, a similarity measure is calculated between every pair of convoluted-raw signals for the tracer particle and the long particle, and the length with the greatest similarity measure is chosen as the correct length of the particle.

Probably the simplest similarity measure of two time-series is the point-wise summed Euclidean distance between the two signals given by the following formula:

$$C(S, S') = \sum_{i=0}^{N-1} (S_i - S'_i)^2. \quad (4.6)$$

However, the problem with this similarity measure is it is not robust against small variations in the phases of the two signals, i.e. if the two signals evolve in time noisily such that they are not instantaneously exactly in phase. For instance, Fig. 4.2A shows two resistive pulse time-series taken during an experiment and overlapped exactly in time, with lines connecting the points that would be summed in the Euclidean distance metric[5]. Notice that the two sequences are very similar, but due to a non-perfect alignment of identical features in time, the aligned Euclidean distance metric will greatly penalize the similarity of the two signals. One method of measuring the similarity of two time-series that accounts for time offsets is

Distance matrix



Cost matrix

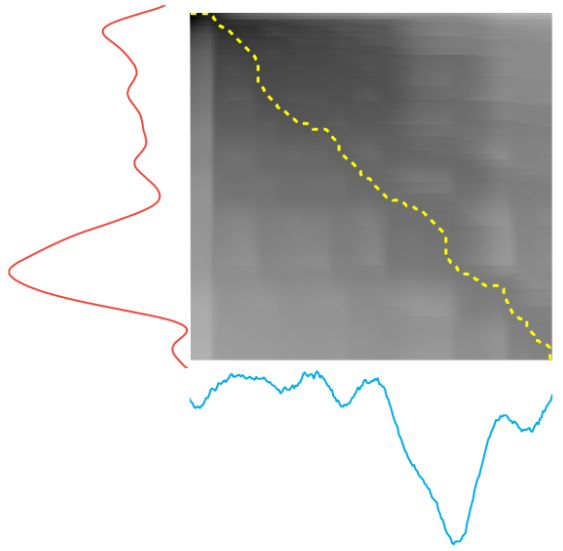


Figure 4.3: **Distance (left) and cost matrices (right) of two resistive pulse signals as determined by dynamic time warping.** The element (i, j) in the distance matrix represents the Euclidean distance between the two signals, $(S_i - S'_j)^2$. Every element in the cost matrix represents the summed Euclidean distance along the minimum path that arrives at that point. Therefore, the point at the lower right-most point in the distance matrix is the summed cost to completely connect the two signals. The path that yields the cost of that element in the matrix is represented by the yellow dashed line.

dynamic time warping.

4.1.1 Dynamic time warping

Figure 4.2B shows two time-series signals that have been aligned after dynamic time warping. The image shows that the algorithm is capable of matching points that are not perfectly aligned in time, but that reflect the actual progression of the two signals in synchronization. The algorithm works as follows.

First, a matrix $D_{i,j}$ of the point-wise Euclidean distance between all two points in the two signals is created, as shown in Fig. 4.3 (left). For instance, point $D_{3,4}$ is the Euclidean distance between point 3 and 4 in signals S and S' , respectively. The objective is to traverse through the distance matrix along the path that minimizes the total accumulated distance, or the cost C , subject to certain kinematic constraints, described below. Each step in the trajectory is defined by the indices from the two respective signals (i, j) . The non-warped Euclidean distance metric given by Eq. 4.6 would correspond to a straight diagonal trajectory through the matrix, e.g. no warping at all. Although there are several formulations of dynamic time warping, the original method only allows for three types of motion such that $(i, j) \rightarrow (i + 1, j)$ (progressive vertical motion), $(i, j) \rightarrow (i + 1, j + 1)$ (progressive diagonal motion), or $(i, j + 1) \rightarrow (i, j)$ (progressive horizontal motion). Regressive motion, which would correspond to taking a step backwards in the path back towards the upper left cell in the matrix, is forbidden. The key to dynamic time warping is the means by which we determine the optimal path that minimizes the total accumulated distance. The problem is combinatorically large and scales like $2^{\sqrt{NN'}}$, where N, N' are the number of data points in each of the two signals. Due to this scaling, random searching of paths through the matrix is not a feasible means of determining the optimum path for large NN' . As the name implies, dynamic time warping implies a dynamic computational algorithm for determining the minimum path, described as follows. First, we must recognize that, due to the rules for stepping through the matrix, the minimum path to arrive at point (i, j) must pass through one of points $(i - 1, j)$, $(i - 1, j - 1)$, or $(i, j - 1)$. Therefore, the cost C of point (i, j) is given by

$$C_{i,j} = D_{i,j} + \min [C_{i-1,j}, C_{i-1,j-1}, C_{i,j-1}] . \quad (4.7)$$

With this in mind, we can build up the complete cost matrix $C_{i,j}$ by starting from the top-left

corner $C_{0,0}$ and propagating through the matrix with Eq. 4.7. We repeat this process until we arrive at point $C_{N-1,N'-1}$, which is the minimum cost of a complete matching up of the two signals. At this point we have arrived at the answer we seeked in the beginning, the total distance metric between the two signals. However, it is often informative to calculate the actual trajectory that the dynamic time warping algorithm has determined, so as to verify that the point matching system is meaningful. In order to do so, we traverse through the matrix starting at point $(N - 1, N' - 1)$ in reverse, according to the same kinematic rules (but in reverse). At each step, we move to the nearest adjacent point with the minimum distance. This algorithm is guaranteed to return us to the starting point $(0, 0)$ along the complete minimum path between start and finish. This trajectory is shown by the yellow dashed lines in figure 4.3, and the pointwise connections are shown in the right hand side of figure 4.2.

4.2 Experiment

In order to test the method described above for determining the lengths of particles, we performed resistive pulse experiments with single mesopores ranging from 800 – 1000 nm in diameter. The materials used were polyethylene terephthalate (PET), a polymer which is known to have highly irregularly shaped interiors when pores are prepared *via* the track-etch technique, and polycarbonate (PC), another polymer but with no axial inhomogeneities which will act as a control for the method. Figure 4.4 shows images of both of these types of pores. For the particles, 280 nm and 410 nm in diameter polystyrene beads ('spheres') were used as the tracer particle, and rods of length 590 nm, diameter 210 nm ('short rods') and 1920 nm, diameter 240 nm ('long rods') were used to test the length measurement protocol; the particles are shown in figure 4.5. Particles were suspended in 100 mM KCl solution with 0.5% Tween 80, a surfactant which prevents particle aggregation. The solution was then

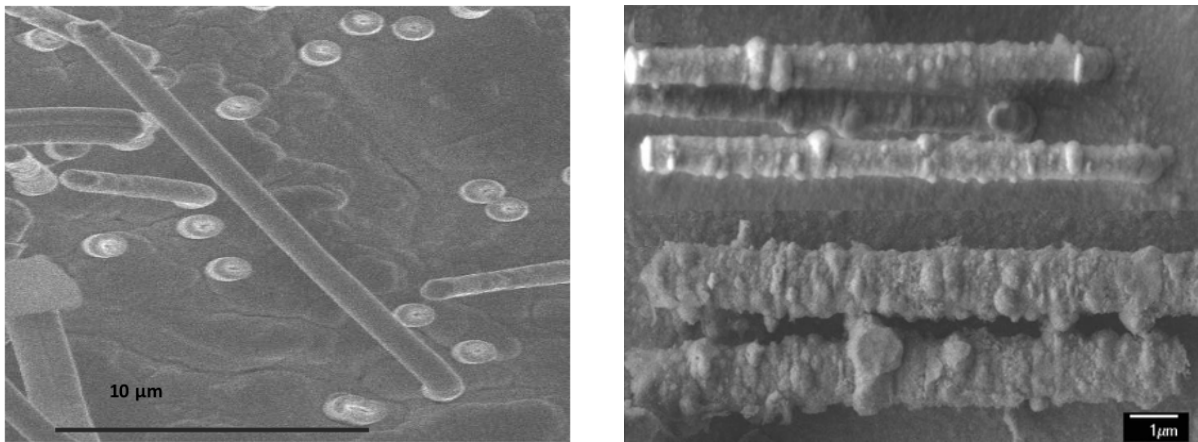


Figure 4.4: Scanning electron microscope images of metal replica of track-etched PC (left) and PET (right) pores. The pores were filled with metal and the polymer was completely etched away, leaving a metal structure that is the inverse image of the pore. The metal was imaged in a scanning electron microscope. While the PC pores are nearly perfectly cylindrical in shape, the PET pores are characterized by rough inhomogeneities across their entire surface, punctuated with large local bumps. The large bumps in the images of the metal replicas correspond to equally large cavities in the PET pore.

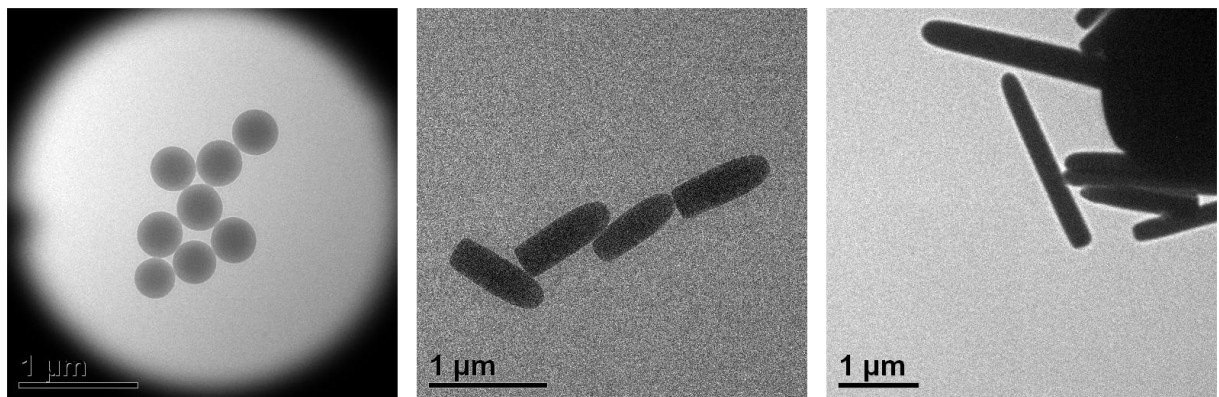


Figure 4.5: Transmission electron microscope images of polystyrene beads and silica nanorods. While the polystyrene beads are nearly perfectly spherical, the silica nanorods are approximately ‘bullet shaped’. For the purposes of this work, we approximated their shapes as ellipsoids in order to apply equation 4.2.

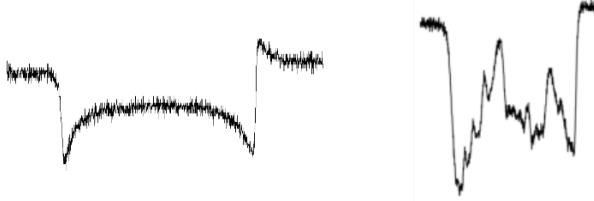


Figure 4.6: Resistive pulse events through PC (left) and PET (right) pores. As expected, the PET events are highly irregular and reflect the interior irregularities of the PET pore itself. On the other hand, the PC pores show no such irregularity. The events show that PC pores have large resistances at the beginning and end, reflecting the narrow, ‘pinched’ diameters at the openings of the pores.

injected into both sides of a conductivity cell, and a voltage was applied across the pore. The resulting ionic current was sampled at 10 kHz and recorded. The polystyrene spheres used had a larger ζ – potential than the pore, and therefore they translocated through the pore electrophoretically. On the other hand, the rods had a lower magnitude ζ – potential than the pore, and therefore travelled through the pore under electroosmotic convective forces.

4.3 Analysis & Discussion

Events were extracted from the current time series and studied separately; figure 4.6 shows two events, one from a PC pore and one from a PET pore that are representative of the translocations through each type of pore. In the initial analysis, we looked at the average $\Delta I/I_p$ of the beads and rods and compared with the theoretical predictions of Eqs. 4.1 and 4.2. Figure ?? shows the results for two pores, one 770 nm and another 1200 nm in diameter. For the two spheres studied, the measured $\Delta I/I_p$ was very close to the theoretical prediction (Eq. 4.1). The theoretical predictions were also very close to the measured values for the long rods. However, for both pores the theoretical prediction of the resistive pulse amplitude $\Delta I/I_p$ is far off for the short rods: the data shows a nearly 100% discrepancy, i.e. the measured $\Delta I/I_p$ is nearly twice its expected value. This significant of a discrepancy is highly

unusual, and one of the goals in the paper was to determine its cause. The discrepancy is made even stranger by the fact that the short and long rods are made of the same material, so any material contribution to the discrepancy e.g. due to large ζ – potentials is unlikely. Instead, we hypothesize that this discrepancy is due to their rotational dynamics. Equation 4.2 predicts that a prolate spheroid (like the rods) will have a larger $\Delta I/I_p$ when they are oriented with an off-axis component, but only considers static positioning. A very large rotational speed of the rods could couple to the measured $\Delta I/I_p$ amplitude in ways not captured by the equation, for instance by stirring the local solution in such a manner to reduce the local ion mobility. Furthermore, this hypothesis is consistent with the non-observance of the increased $\Delta I/I_p$ for the long rods, since at their length of $\sim 1920\text{ nm}$ they are too large to rotate in even the larger of the two pores (1200 nm in diameter). In any case, the net result is a measured volume for these particles that is approximately $2\times$ larger than their actual volume, which was confirmed with a combination of transmission electron microscopy images and dynamic light scattering.

The question, however, is how such a large rotation could occur. To answer this question, forces that cause rotation must be considered. In terms of translation (transport), the contributing forces are convection due to electroosmosis, and electrophoresis, as well as passive transport due to diffusion. Similarly, these forces could also contribute to rotational motion of the particles. The estimated rotational diffusion contribution of these rod particles is estimated as 13 and 0.8 rad/s for the short and long rods, respectively. In order for fluid motion to cause rotation, it is necessary to have a non-constant fluid velocity profile on the pore's length. However, because the fluid velocity is due to electroosmosis there will be a nearly constant fluid velocity profile in the pore, which is unlikely to cause significant rotation. On the other hand, the rough undulations in the pore could create axial variations in the electric field; such variations could also lead to a net torque on the particle that causes rotation. In order to estimate the potential magnitude of the rotational velocities of the rods, we considered a simple model where the pore's diameter discontinuously changes

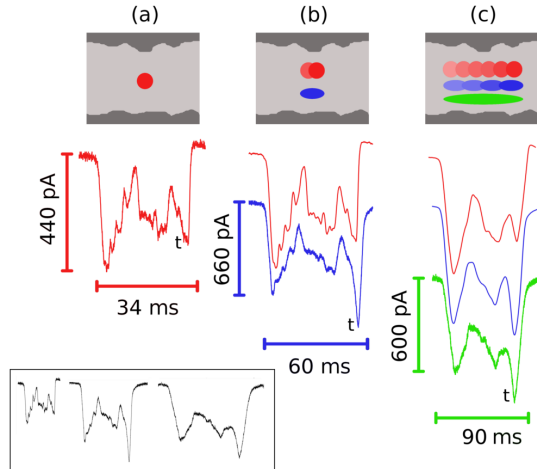


Figure 4.7: **Resistive pulse events of a 410 nm diameter sphere (red), and 590 nm (blue) and 1920 nm (green) in length rods.** The top row shows a cartoon scheme of the pore with the particles inside its interior. The bottom resistive pulse event in each column corresponds to the raw recorded data; events above this are smoothed *via* the moving average transformation. The bottom left figure shows the raw events on the same scale.

from 1000 nm to 1100 nm, a reasonable approximation for the geometries present in our system based on the images of the pores (see Fig. ??). Under this model, we calculate the electric field amplitude to differ by a factor of 1.2 between the two regions. Using the rotational diffusion coefficient of the rods and integrating the electric field differences along the length of the pore, we calculate the angular rotation rate ω to be $\omega \sim 10^4$ rad/s. Due to the preceding arguments, it is clear that the largest contribution to the rotation of the rods is from the electric forces. We believe that such a large rotation could make the rods behave as if they are much larger particles.

Figure 4.7 shows example recorded events for the three types of particles used in this study. A 410 nm sphere translocation is shown on the left column in red. Notice the roughness in the event; this roughness has been shown to correspond to the interior irregularities in the pore. Local $\Delta I/I_p(t)$ are large at relatively constricted points, and small at larger cavitated points. The green event in the right column corresponds to the raw resistive pulse signal of a long rod. Notice the difference in structure of the two events; the long rod's event shows some structure, but is missing many of the local minima and maxima that are present in

the signal of the short rod. This observation is in agreement with our previous arguments for the smoothing of the pore interior that takes place for long particles. Without making any quantitative arguments, we are able to conclude that the particle corresponding to the green event is longer than the particle corresponding to the red event. In between those two extremes are the short rods in red. The short rods at length 590 nm are slightly longer than the spheres which have diameter 410 nm, but due to their rotation it is not entirely obvious whether they should image the pore with the same resolution as the spheres. Looking at the results, the signals of the short rod and sphere are much more similar than the long rod and the sphere, but some local structure is still unresolved for the short rods.

In order to test the hypothesis that long particles behave as a moving average of shorter particles, we calculated moving averages of the spheres and the short rods. The time over which the moving average was calculated corresponded to the duration in time over which the particle travelled a distance equal to the length of the longer particle with which it is being compared. We determined the average velocity of a particle from the total translocation distance (the known length of the pore, $L' = L - D$) and the translocation duration measured from the RP signal, ΔT . The velocity is then $v = L'/\Delta t$. The moving average window then has length (in time) of $\Delta t = v/l$, which corresponds to a window of $N = f \times \Delta t$ data points in length. The transformation then from the raw signal I_i to the averaged signal I'_i is

$$I'_i = \frac{1}{N} \sum_{j=-N/2}^{N/2} I_j. \quad (4.8)$$

This moving average process was performed on the spheres and on the short rods. The red signal in the middle column corresponds to the moving average of the spheres over the length of the short rods, and the red signal in the right column corresponds to the moving average of the spheres over the length of the long rods. Finally, the moving average of the short

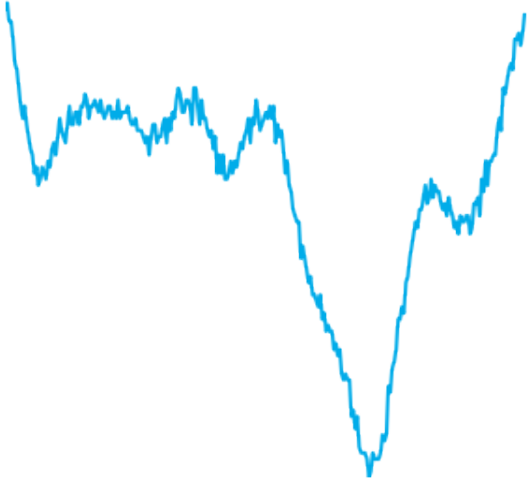


Figure 4.8: Resistive pulse signal of a single long rod passing through a PET pore. The variation in the amplitude of the current signals that the pore has an inhomogeneous interior shape.

rods over the length of the long rods is the blue signal in the right column. Qualitatively, we see that the moving average process, which is physically motivated by the equations for the resistance of small particles in series, recovers the appearance of the signals of longer particles.

In order to measure the lengths of the long rods, we performed the dynamic time warping technique described in the preceding section. Figure 4.8 shows a single instance of a long rod passing through a PET pore. Figure 4.9 shows a shorter rod particle averaged over many different length intervals. As the short rod is averaged over a greater length interval, it continuously transforms into a shape that bears a stronger resemblance to the signal of the long rods. Of all the fits calculated in Fig. 4.9, the correct length is determined by the fit with the smallest cost as determined by dynamic time warping. An example resistive pulse signal of a long rod and a shorter rod that has been transformed *via* the moving average equation is shown in Fig. 4.10. Finally, after performing the moving average and dynamic time warping minimization approach described above, we were able to determine the expected lengths of the long rods according to this algorithm. Figure 4.11 shows a plot

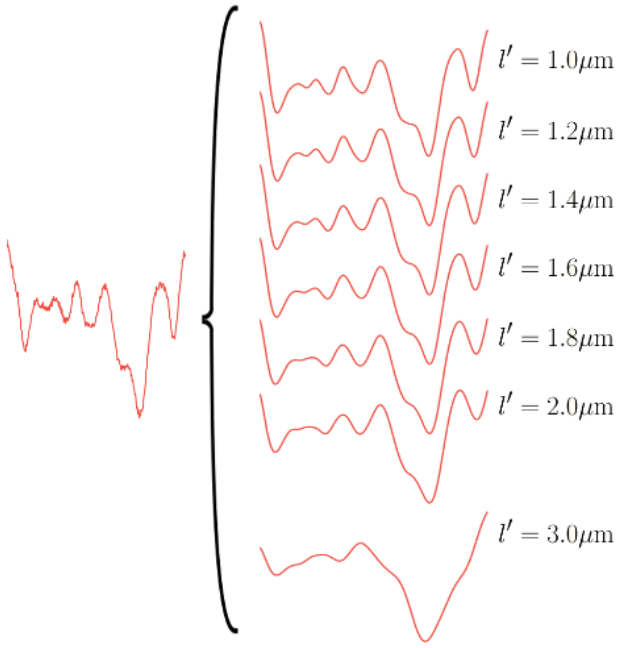


Figure 4.9: Resistive pulse signal of a single short rod passing through a PET pore alongside many instances of the moving average transformation performed on the signal for different length intervals. As the length interval is increased, the finer structure of the resistive pulse signal is smoothed over. For the greatest length measured, many of the features prominent in the raw signal have disappeared..

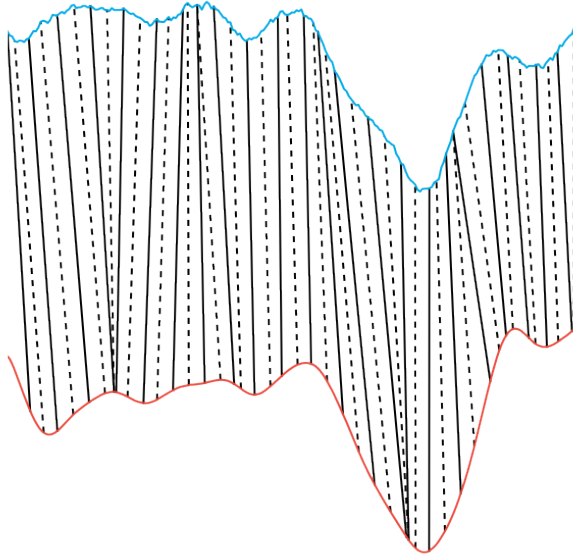


Figure 4.10: Raw resistive pulse signal of a single long rod matched with the signal of a short rod that has been transformed via the moving average process. The aligned points were determined by the dynamic time warping algorithm, and the particular transformation shown was the one that minimized the difference between the two signals, also determined by the dynamic time warping algorithm.

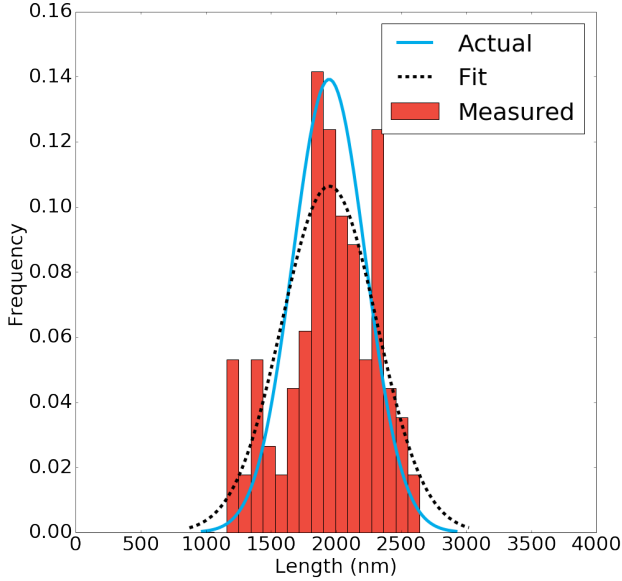


Figure 4.11: **Histogram of particle length as determined by dynamic time warping along with the actual distribution of sizes determined by electron microscopy imaging.** A normal distribution is fit to the histogram of particle lengths as determined by dynamic time warping and shown to be in good agreement with the expected distribution.

of histograms of the lengths as determined by this approach, alongside a Gaussian fit to the histogram, and a Gaussian distribution that shows the actual distribution of hte lengths of the long particles as determined by electron microscopy images. The figure reveals that, in this case, the dynamic time warping algorithm is able to successfully recover the real distribution of the known lengths relatively accurately.

4.4 Conclusions

In summary, we presented resistive pulse experiments performed with spherical and non-spherical particles in two types of pores, those with smooth interiors (PC) and rough interiors (PET). We devised a protocol for measuring the lengths of long particles by taking advantage of the rough interiors of PET pores, which reflect in the measured resistive pulse signals of all the particles. Longer particles displace a greater distance along the pore's length, and therefore their signals are a more smoothed version of the signals of shorter particles. This

smoothing attribute can be recovered by taking the moving averages of shorter particles. By performing moving averages for many different particle lengths and measuring the similarity between the raw signal of the long particles with each of the transformed signals of the shorter particles, we were able to determine the length distribution of the long particles used in experiments. Dynamic time warping was used as a means of effectively comparing the similarity of the signals of the two particles. While the general premise of the ‘smoothing’ of the resistive pulse signals by long particles compared to short particles is convincingly established, more research must be performed on the hybrid moving average-dynamic time warping method. The protocol was only tested for a small number of pores and only two types of particles, short and long rods. In the future, an ideal experiment could be performed with small spherical beads and rods of various unknown lengths. The experiments and analysis would be performed in a blind fashion, and only after the analysis is complete would the true length distribution of the long rods be revealed. If the length measurement protocol survives this blind study, it would prove to be a very effective means of determining the lengths of small particles.

Additionally, a likely unrelated phenomena was discovered where short, aspherical particles created far greater (up to 2x) resistive pulse amplitudes than predicted by the well-established classical equations. The exact reason for this effect is still unclear, however we laid out arguments that explain rotational dynamics as a likely culprit. We reasoned from our studies that an extremely rapid rate of rotation could effectively increase the radius of the particle, possibly by disturbing the local solution and decreasing its conductivity. Such rotations would not be possible for the longer rods due to their prohibitively long lengths compared to the diameter of the pore. However, more investigation must be performed in order to convincingly show that not only do short rod like objects deviate strongly from the classical equations, but also that rotational dynamics is the culprit. Additional experiments must be performed with a larger variety of short rods to show that the effect is general and not limited to the rods used in this study. Furthermore, experiments could be designed in such

a way as to retard the rods' rotations, perhaps by using smaller pores or solution with an increased viscosity.

Chapter 5

Resistive pulse studies of cancer cell deformability

5.1 Background & Theory

One of the most important applications in microfluidic technology today is the study of cell populations. The most important tool for studying cell properties is the flow cytometer, invented in 1965 by Fulwyler [4], and is conceptually the follow up to Coulter counters which can be considered to be impedance cytometers. Flow cytometers are a mixture of many individual microfluidic elements combined in series, each with its own function. On the sensing side, flow cytometry makes use of measured scattering of laser light as well as detection of fluorescence signals. Dyes are specifically attached to certain types of antibodies, which then may interact with the cell membranes in the suspension. When the cells are pulsed by lasers in the laser light, it stimulates emission of specific dyes, which can be measured to determine which antibodies have interacted with the cell. This type of information is incredibly valuable in determining phenotypic and classification information for the cells. Furthermore, the in-

formation garnered from real-time cytometry information can be used to sort cells in real time, in a system known as fluorescence activated cell sorting system (FACS). Cell cytometry is the workhorse of modern day molecular and cellular biology studies, but suffers from the fact that it is a label-dependent method due to the introduction of the dyes. Such labels can adversely affect the the cells' viability that prevents them from being used in a post-interrogation analysis, even after being separated by a system like FACS. Additionally, flow cytometry requires the use of costly fluorescent reagents and skilled technicians that must be present to perform the measurement and to ensure proper calibration of the fluorescence signal *via* the use of fluorescent beads [?] (DiCarlo PNAS).

While flow cytometry focuses on the measurement of cells' interactions with specific antibodies, another dimension often not thought of is the cells' mechanical properties, such as their size, shape, deformability, and deformability dynamics [?] (DiCarlo paper in Nature 2017). Since their discovery, we've known that a wide variety of cell sizes exist, but more recently scientists have focused on the difference in the mechanical stiffness of cells. Cell stiffness has been shown to vary from cell to cell, and even between various stages in cells' mitotic cycles. As a concrete example, cancer cells are known to be generally 'squishier' than non-cancerous cells. For these reasons, developing a method of probing the mechanical stiffness of cells is highly desirable for cell characterization applications, and serve as a complementary cell phenotyping platform to deformability cytometry.

In order to measure the stiffness of an object, it must be subjected to constrained forces and its response measured. Probably the most straight forward way of doing this is by directly applying a mechanical force on the cell, for example by using an atomic force microscopy (AFM) probe to directly press on the cells and measure the resultant recoil force felt by the AFM's cantilever, which is directly related to the Young's modulus of the cell. Other similar methods exist, and while they are very accurate and easily interpretable, they suffer from an excruciatingly slow throughput. For instance, using AFM for cell deformation measurement

can take a few minutes per cell. For cell applications a high throughput is necessary, and therefore these applications are not feasible for discovering cell population statistics.

Another method of measuring cell deformability is with microfluidics platforms. Cells passing quickly through narrow constrictions are subjected to large, anisotropic hydrodynamic forces, and these forces can induce a measurable particle deformation. The advantage of this type of method is its extremely large throughput; rather than spending several minutes per particle as in measurements conducted with AFM, thousands of cells per second can be measured in microfluidic platforms. Even within the narrow field of microfluidic-based deformability cytometry, there are multiple types of platforms. Probably the most conceptually simple is a standard microfluidic channel that tightly confines cells passing through it. Due to anisotropies in the hydrodynamic stresses and strains around the particle, it will deform even in a uniformly shaped channel.

In traditional microfluidic methods of measuring cell deformability, direct imaging is used to determine the cell shape across different frames in the video, which corresponds to the hydrodynamic load it is under. However, for the high throughputs that are the reason why people use microfluidics, camera imaging must be performed very quickly. This requires the use of a high-speed camera used in conjunction with an optical microscope, usually shooting at a minimum of 10 000 fps. When combined with an optical microscope, such high-speed cameras are capable of capturing cell deformations with high spatial and temporal resolution, and are even capable of resolving the cells' deformation dynamics [?]. Currently high-speed camera imaging is by far the most popular method of capturing cell deformations, but it comes with two serious disadvantages. First, the camera itself adds a large cost to the apparatus, and will likely dwarf the price of any other component in the deformability cytometer. Second, imaging data is inherently highly multidimensional and computationally expensive to analyze. As a result, online analyses conducted during the run of the experiment are usually not possible at the flow rates that these experiments operate at. While the data

can still be stored, processed, and analyzed later, offline analysis does not allow for real-time separation, one of the most highly desirable applications of this type of metrology.

Instead of using camera imaging, one can instead imagine trying to employ resistive pulse (RP) to measure the deformability of particles. In terms of practicality, RP is far more computationally light than imaging data, as the following order of magnitude estimate shows. First, consider the data bandwidth in high-speed imaging. Passage through a deformability cytometry system may consist of ~ 100 frames, each with a resolution of perhaps 100×50 8-bit grayscale valued pixels. As a result, a single translocation is described by 500 kB worth of data. At a rate of 1000 particles per second, this corresponds to a raw data throughput of 500 MB/s of data that must be processed. Finally, in a common image processing algorithm the number of computations performed on each pixel is probably greater than one; identifying the shape of an object in a frame certainly consists of multiple serial image processing steps. Although this is just an estimate, it conveys the point that high-speed imaging is not amenable to online analysis, especially at the throughputs that are desired for these types of calculations. On the other hand, consider a resistive pulse analysis: under the same criteria described above, an RP data stream being sampled at 1 MHz will consist of a data throughput of only 1 MB/s , a factor of 500 decrease in raw data throughput. Furthermore, the types of operations needed to extract deformability information from the raw RP signal are also computationally light relative to image processing techniques.

While it is apparent that resistive pulse is computationally cheaper than imaging analysis, it is most important to demonstrate that deformability can actually be measured via RP sensing. In chapter 4 of this dissertation, we discussed the equations for the resistive pulse amplitudes of ellipsoidal objects. For cells that are spheroidal in their unloaded state, ellipsoids are reasonable geometries to expect for the deformation shape in the loaded state, at least as an approximation. If we consider a straight ion conducting channel with an ellipsoidal particle inside it, the aspect ratio and orientation of the particle greatly affects the

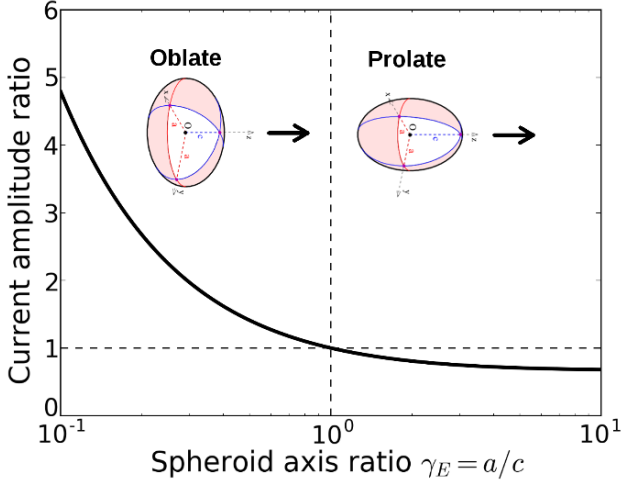


Figure 5.1: **Resistive pulse amplitude $\Delta I/I_p$ for equal volume spheroidal objects relative to a sphere.** The polar axis of the particle is aligned with the channel’s axis, so that oblate geometries correspond to motion along the channel axis. The values come from equation 5.1 when the correct shape factor f_{\parallel} is applied.

ionic resistance of the system. Under the assumption that the particles take on ellipsoidal geometries, the shapes will be described as being prolate, oblate, or spherical with respect to the channel’s axis. Oblate geometries correspond to a flattening along the channel’s axis, and prolate geometries are an extension along the channel’s axis. The difference in the measured resistive pulse amplitude of these particles is given by the following equation:

$$\frac{\Delta I}{I_p} = f_{\parallel} \frac{v}{V}, \quad (5.1)$$

where v and V are the volume of the particle and channel, respectively, and f_{\parallel} is a constant known as the ‘shape-factor’, which depends on the aspect ratio of the ellipsoid.

For spheres, $f_{\parallel} = 1$, and for prolate and oblate spheroids, $f_{\parallel} < 1$ and $f_{\parallel} > 1$, respectively. Figure 4.1 shows plots of the RP amplitude $\Delta I/I_p$ for ellipsoids of the same volume but different aspect ratios, relative to a sphere. The plot reveals that even for modest deformation, for instance a stretching ratio of $2/3$, a mildly oblate ellipsoid, the increase in

$\Delta I/I$ is nearly 30%. Similarly, the current $\Delta I/I$ changes for prolate geometries, although to a lesser degree.

As mentioned previously, there are many possible types of high throughput microfluidic systems than can induce cell deformations. We devised a method that has been shown to be capable of inducing bidirectional deformations (prolate and oblate). The key to understanding the channel geometry is to understand the primary hydrodynamic forces that work on a cell and deform it in extensional, i.e. accelerating and decelerating flows. When a cell transitions from a region of high local fluid velocity to low local fluid velocity, there is a greater magnitude of normal stress forces on the back of the particle than on the front. Consequently, the particle is pushed into a laterally elongated state, corresponding in our model to the oblate geometry. Oppositely, when the particle makes the transition from a slow to fast region, the net forces pulling the particle forward are greater than the forces pushing it from behind, elongating it in its direction of motion. This corresponds to the prolate shape configuration. According to this model, one can induce bidirectional shape changes in passing particles by having transitions between regions of slow and fast local fluid flow, and vice versa. This criterion allows for multiple possibilities, but the geometry chosen for our system is described by a channel having a central cavity, but otherwise with a straight cross-section. As the cell enters the microchannel, it accelerates and is pulled in, and in the process deforms into a prolate shape. When the cell arrives at the central cavity, the fluid flow is slower and the particle decelerates, becoming oblate. At the end of the cavity, the particle again undergoes an acceleration and deforms back into its prolate shape. Figure ?? shows an example image of one of the channel geometries used in this study, along with a scheme showing the deformation modes that occur in each region of the channel.

Although the deformation dynamics are undoubtedly complicated, to first order we seek to find the aspect ratio of the approximate ellipses a/b at various points in the channel. The aspect ratio will remain the same at all points for completely non-deforming particles, but

will vary according to the above model for deforming particles, and to a greater degree for the most deformable particles. For the scheme shown in Fig. ??, the expected aspect ratio a/b as a function of the axial position adheres to the motif shown in Fig. ???. Besides size, the observables of interest might be the minimum and maximum aspect ratios, or perhaps the ratio of the minimum and maximum aspect ratios which would reflect the general elasticity properties of the cells. However, in the RP signal the actual deformation of the particles would be reflected in the changes in the measured $\Delta I/I_p$ signal *relative to the expected $\Delta I/I_p$ of a completely non-deforming spherical particle of the same volume*. This means in the narrow regions where a prolate elongation occurs the current amplitude $\Delta I/I_p$ would be *decreased*, while in the central cavity where the particle assumes an oblate geometry the signal would be *increased*. Figure ?? shows an example RP event for a particle passing through the cavitated channels, and the distortion of the RP signal corresponding to the model described above. Therefore, the observable of interest might be the ratio of the maximum in the signal (minimum $\Delta I/I_p$) and either of the two minima in the signal (maximum $\Delta I/I_p$), which would be a proxy measurement for the ratios of the aspect ratios calculated directly from imaging data. For larger deformations, this ratio would increase as the signal distortion motif in Fig. ?? shows.

5.2 Experiment and data analysis

In order to test the concept of cell deformability cytometry with the channel geometry described above and using RP, we ran microfluidic experiments with cancer cells. Although the ultimate goal of this sensor will be to perform deformability cytometry with the RP signal alone, in order to test the method it is necessary to have a high-speed camera. In the following sections we describe the complete experimental set up, the software used to control the experimental instrumentation, and the data processing and analysis steps that take place

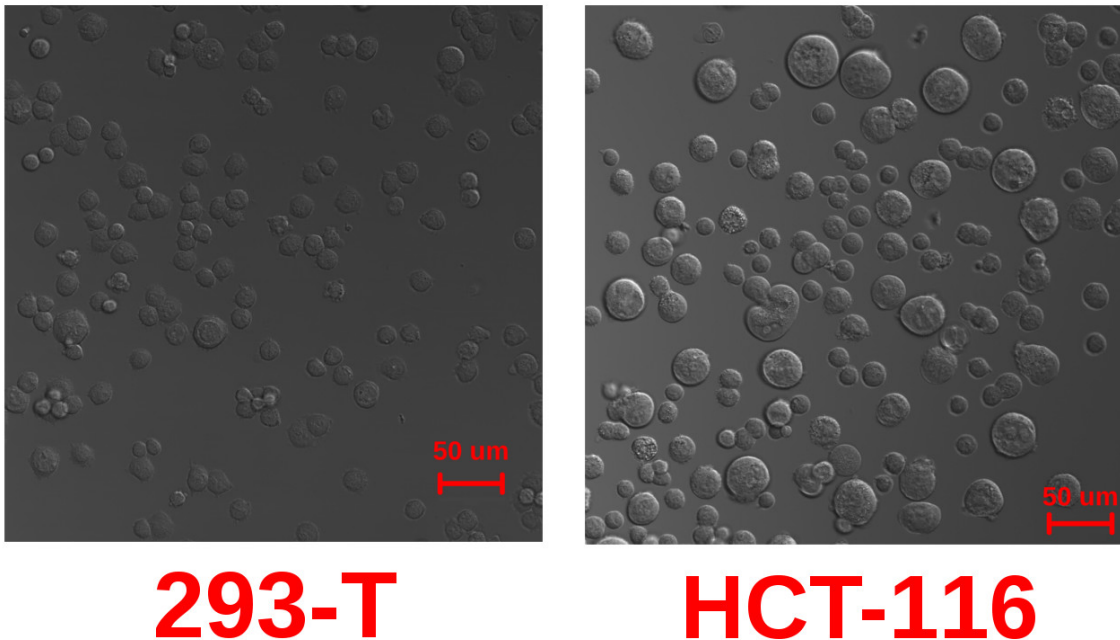


Figure 5.2: Confocal images of 293-T (left) and HCT-116 (right) cells. Scale bars are $50 \mu\text{m}$ long.

after the experiment. To date, the experiments performed have primarily been focused on analyzing the optical data in the experiments, since measuring their deformability optically is a prerequisite for determining it via the RP signal.

5.2.1 Experiment and instrumentation control

The entities involved in the experiments include the microfluidic channels, the cells and the suspension media that holds them, a syringe pump to drive the suspension through the systems, a microscope and high-speed camera used to take the images, the data acquisition card (DAQ) that acquires the RP signal, a central control computer used to run the experiments, and various other miscellaneous pieces of equipment. A more in-depth description of these components and the roles they play in the experiment is as follows.

First, we start with the cells. Three human cell lines were provided for the experiments,

Step name	Instrument	Parameters
Preprocess cleaning	Isoproponal	
Wafer dehydrate	Dry oven	95°C, 30 min
First spin	Laurell spinner	(parameters)
Second spin	Laurell spinner	F
Soft bake (cold)	Hot plate	65°C, 1 min
Soft bake (hot)	Hot plate	95°C, 5 min
UV flood exposure	AMV	52 seconds (intensity varies, adju
Post-exposure bake (cold)	Hot plate	65°C, 1 min
Post-exposure bake (hot)	Hot plate	95°C, 5 min
SU8 develop	SU8 develop solution	5 min soak, with periodic agitat
SU8 developer rinse	SU8 developer solution	
Soft bake (hot)	Hot plate	95°C, 5 min
Post-photolithography bake	Hot plate	95°C, 2 hours
PDMS preparation	Sylgard-184 and curing agent	10:1 by volume Sylgard-184 t
PDMS degassing	Vacuum	30 min
PDMS cure on SU8 mold	Hot plate	75°C, 150 min
PDMS-glass bond	Harrick-Plasma oxygen plasma chamber	300 mT, med. power,

Table 5.1: Class Mark List

chosen for the variety of deformation and size properties they exhibit. The cell lines are HCT-116 (colorectal cancer), 293-T (derived from human embryonic kidney cells), and THP-1 (monocytes). Images of the HCT-116 and 293-T cells are shown in Fig. 5.2. The cells are filtered and diluted to a concentration of $0.5 \times 10^6/\text{mL}$ or $1 \times 10^6/\text{mL}$ in a solution of HBSS, a relatively highly conductive biocompatible buffer. In most experiments, the solution was doped with methylcellulose, another biocompatible component that increases the viscosity of the solution, which should promote cell deformations. Pluronic, a biocompatible surfactant, is added at 0.1% concentration by volume.

The microfluidic channels are fabricated *via* standard, well-established soft photolithography techniques. Fabrication primarily takes place in a class 10000 clean room of the BiON facility at the University of California, Irvine. First, SU8-2025 photoresist is spun onto a 4 inch silicon wafer with the correct rotational speed to achieve a thickness of $20\ \mu\text{m}$. A transparency with the channel design printed on with a high DPI printer is taped onto the SU8 side of the

wafer, which is then exposed to a UV flood lamp. UV light passes through the non-printed parts of the transparency and reaches the SU8 photoresist. Polymer molecules in the exposed areas are cross-linked, resulting in these regions being more stable. The photomask is then removed, and the wafer soaked in SU8 developer solution until the non-crosslinked parts of the channel are completely washed away. The resulting structures left after the SU8 is washed away comprise the device mold. PDMS, a relatively chemically inert elastomer is degassed and then poured over the mold and baked until completely hardened. After curing, the PDMS layer is carefully pulled off the wafer, and individual microfluidic devices are cut out. The inlet and outlet access ports are punched through with a biopsy punch. Finally, the PDMS device and glass slide are treated in an oxygen plasma which temporarily alters the chemical composition of the surfaces, allowing for bonding. After being taken out of the plasma, the glass slide and PDMS layer are quickly but delicately pressed together, resulting in a quick bonding. Table 5.1 contains a list of the key steps involved in the device fabrication, the particular instrument(s) used in each step, and all main parameters relevant to those instruments operations in this application.

Once the device is fabricated, it is taped onto the glass stage of the optical microscope. The high-speed camera is mounted on to the microscope, where the light is directed instead of into the eyepiece. Plastic tubing, which serves as the fluid access, is inserted into the inlet and outlet ports. Ag-AgCl electrodes are inserted into the tubing as well, as close as possible to the actual microfluidic device. The electronic set up used to make RP measurements consists of a patch clamp amplifier, which in its current configuration merely applies a voltage, and a lower amplification amplifier. This circuit is connected to a BNC breakout box, which connects to the data acquisition card via a parallel data bus, which actually streams the measured RP data. A syringe containing the particle solution is inserted into the inlet tubing with a luer lock configuration, and the syringe is mounted onto a syringe pump which is used to drive the solution through the channel. Finally, the syringe, high-speed camera, and data acquisition card are all connected into a central control computer which is used to

command the three instruments and save their data locally. Figure ?? shows a scheme of the hardware implementation used for the experiment.

In order to control the three instruments and save data, a graphical user interface (GUI) program was written. The program was written in C++ and the Qt Framework, and uses threading to ensure asynchronous operation of the three instruments, as well as the controls in the GUI itself. Communication protocols used were specific to each of the hardware instruments. The software communicates with the syringe pump *via* a serial RS-232 communications protocol. Communication with the high-speed camera occurs over TCP/IP protocol over a 1 Gb ethernet line, with instructions specific to the camera's manufacturer. Lastly, the DAQ card is controlled via the niDAQMX software library. The software allows the user to perform all operations on the syringe pump remotely. When not recording, the software displays live images from the camera feed that show the view through the microscope. The user may also change the camera's recording parameters such as frames per second, exposure rate, and pixel resolution, and when ready, to record videos and save the data to the computer after recording. Similarly, the software also displays the RP data stream and can save it as well. Figure 6.2 shows an image of the GUI program; the software is open-sourced and available at https://github.com/tphinkle/cell_controller.

After the cell suspension is prepared and the experiment set up, data recording occurs. The syringe pump is started so that the solution is driven through the microfluidic channels. The initial ‘push’ of the syringe pump is usually much greater than needed, which serves two purposes. First, it quickly pushes the solution from the syringe pump to the actual device. Sedimentation due to gravity is significant for the cells used here, so a quick start to the experiments is highly desirable in order to ensure high event frequency during recording. The second purpose of pushing solution very rapidly is that it puts the fluid into a turbulent regime. In this regime, the regions of solution adjacent to the exit of the channel display stable turbulent vortical flows, and are very likely to capture cells. These trapped cells

provide a target by which to focus the microscope; due to the extremely small size of the channels, even under small latent pressures in the system (i.e., without pushing on the syringe pump), cells move far too quickly to properly focus on, usually staying in the field of view of the camera for only a single frame in the GUI's view. However, while the cells trapped in the vortical flows at the channel's exit are rapidly moving, they do not leave the field of view of the camera and therefore act as a moving target on which to focus the microscope. This unconventional trick has proven absolutely invaluable in the experimental workflow, as the focus required to obtain good camera images of the cells is very sensitive. In unfocused images, while cells may be detected their boundaries are often non-resolvable. After the proper focus has been established, the flow rate is reduced to the desired flow rate that the user wishes to record, and a fixed amount of time is waited to allow the fluid to equilibrate. After this delay, both the RP and camera signal are recorded. While the recording itself is very fast, the data must be transferred to the control computer in order for it to be stored; the onboard camera memory is only sufficient to hold the data of a single recording. The transfer and saving process takes nearly 15 minutes, and over this duration of time the vast majority of cells sediment to the bottom of the tubing and syringe. For this reason, in between data transfers we remove the tubing and syringe and clean them. After recording, the solution is gently mixed to resuspend the cells, and the process of pushing the solution, refocusing the microscope, and recording is repeated. Experiments are repeated in this way for different cell lines, channel geometries, and fluid flow rates. Following the experiments, data is immediately backed up redundantly to external storage drives where it remains until it is ready for post processing and analysis.

5.2.2 Data analysis

The data generated from these experiments includes the imaging data from the camera and the resistive pulse data. In order to analyze this unique combination of data sets, a library

called pore_stats was written in Python. pore_stats was primarily written for the purpose of analyzing resistive pulse data, however image processing functions were added to analyze the data from these hybrid RP-IM experiments. Pore_stats is discussed in greater detail in chapter 6

The primary observable of interest in this experiment is the shape of the particle. There is no single way of defining the shape of an object, but because we are interested in comparing the RP signals of cells with the theoretical RP amplitudes of ellipses, we determine the shape of the cell by fitting ellipses to its borders across multiple frames. Thus, the objective in demonstrating deformation optically is to fit ellipses with semi-major axis a and semi-minor axis b to cells across multiple frames and track their change in aspect ratio as they pass through the channel. According to the above model, the cells should oscillate between prolate, oblate, and spherical shapes at various points in the channel, and therefore we expect to observe an oscillation of the determined aspect ratio $\gamma = a/b$ between values > 1 and values < 1 . The exact shape of the cell is never exactly ellipsoidal, however we find that for most shape configurations it is an adequate approximation.

While the ellipses could be fit manually by determining the width and height of the channel in each frame, the number of cells observed prohibits this manual measurement. Instead, we devise an image processing pipeline that starts with the raw camera data and results in a calculation of the ellipse fits for every single detection and every single particle passing through the channel. The pipeline works as follows. First, cells are detected in individual frames via a template subtraction method. Then, cells are tracked across frames using a minimum distance approach. These two methods are described in greater detail in chapter 6. After a list of events is determined, ellipses need to be fit to the image of the cell in each frame. A number of preprocessing steps is required to transform the image to a form where this ellipse fitting is possible. One possible ellipse fitting protocol is shown in Fig. 5.3. All processing protocols must reduce the image down to a binary form where the only

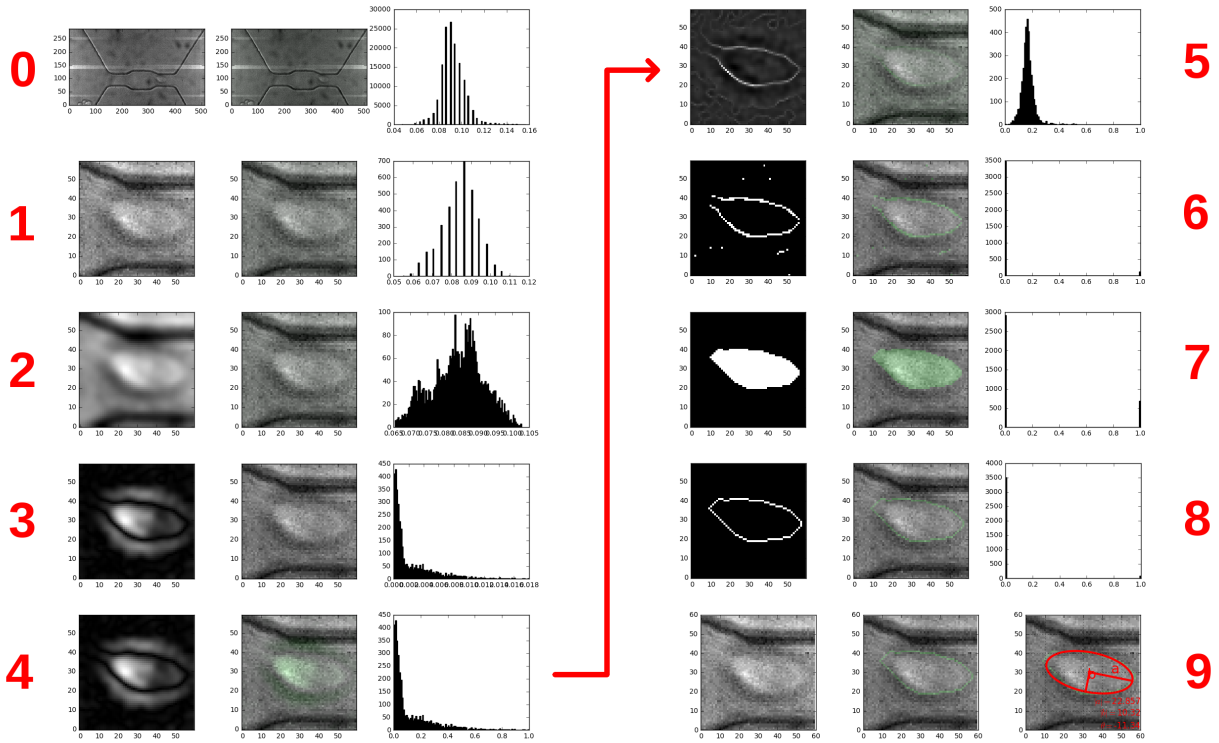


Figure 5.3: Example ellipse fitting protocol for a single detection within a single event. The left column of each row shows the current image transformation. The central column shows the raw frame with the pixels shaded green with intensity according to the intensity of the pixels in the transformed image. The right column shows pixel intensity in the processed image. **1:** Raw image. **2:** Image is cropped in the vicinity of the particle. **3:** Template image is subtracted off. **4:** Pixel intensity is rescaled. **5:** Laplacian derivative. **6:** Pixel intensity thresholding. Notice the histogram becomes binary distributed. **7:** Morphological closing of image. **8:** Image is dilated and subtracted from undilated image, leaving a thin shell around the border of the cell. **9:** Ellipse is fit to the cell's border.

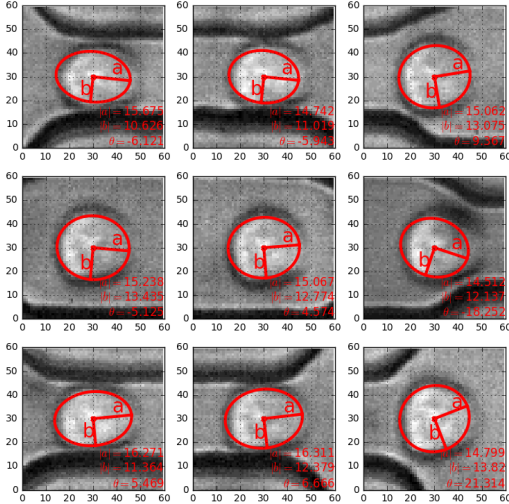


Figure 5.4: Ellipse fits for a 293-T cell passing through a $15 - 30 - 15\mu\text{m}$ channel at various positions. Notice that in the narrow portions of the channel the particle assumes a prolate (axially-elongated) shape, while in the central cavity it assumes an oblate (laterally-elongated) shape, in agreement with the motif presented in Fig. ??

pixels highlighted are the pixels on the exact boundary of the cell. Operations common to most processing protocols are template subtraction, Gaussian blurring, Laplace derivative transformation, thresholding, and morphological operations such as binary dilation, erosion, and closing. The end result is shown in Fig. 5.3, row 9. Fitting an ellipse to the particle in each frame is useful because many properties of the particle and its translocation can be determined via the ellipse fits. For instance, ellipse fitting yields accurate determination of the central position of the particle, which can be used to accurately determine its trajectory and velocity. Furthermore, once the ellipse is obtained for every frame it is easy to calculate the aspect ratio of the particle during the course of its trajectory and compare with the expectations of the model proposed earlier (Fig. ??).

5.3 Results & Discussion

The most important question to be answered in the experiments is whether the cells actually deform according to the model proposed. In order to answer this question, we examined specific events to look at their change in aspect ratio as they pass through the channel. Many events consistently show a deformation pattern that subscribes to the model, as shown in Fig. 5.4. On the other hand, there were many events that showed modest to little deformation. However, this result is not unreasonable; our model does not suggest that all cells must deform, and indeed there may be cells that are quite resilient to deformations, or cases where the hydrodynamic forces were insufficient to generate significant deformation. However, we never observe a trend opposite to the deformation mode posited, i.e. an oblate-to-prolate transition rather than a prolate-to-oblate transition. This observation suggests that, while the magnitude of the effect may be low in some cases, the effect still occurs.

Chapter 6

Hybrid resistive-pulse optical detections in microfluidic systems

6.1 Background & Theory

As we have seen, RP sensing is a method for determining the physical properties of particles by way of measuring the change in resistance of a conducting channel they create as they pass through it. RP's primary advantage is that it can be employed at many scales and in a diverse number of applications, and is especially useful at the nanoscale where the number of particle characterization techniques is limited—in particular, optical imaging is prohibited at this scale. To first order, the mechanism for the rp current pulses is straight forward: when the particle enters the channel, it occupies a volume that would otherwise be occupied by ions, decreasing the conductance, and increasing the total system resistance. According

to this simple model, the resistive of the system is determined solely by the equation

$$R = \rho \int A^{-1}(x) dx, \quad (6.1)$$

where R is the system resistance, $A(x)$ is the annular cross-section of the channel at position x , and ρ is the resistivity of the solution. In most RP set ups, the current is measured instead of the resistance, so Eq. 6.1 is usually inverted via Ohm's law to obtain the current: $\Delta I/I_p = \Delta R/R_0$, where I is the measured current, and the subscripts 0 and p denote quantities when the channel is empty, and occupied, respectively. While Eq. 6.1 serves as a good approximation for the RP amplitude that may be accurate in some cases, it fails to take into account the electrostatic boundary conditions present in the system. For a completely insulating pore and particles, these boundary conditions are $E_n = \sigma$, and $E_t = 0$, where E is the electric field, n is the direction normal to the surface in question, t is any transverse direction, and σ is the charge density of the surface. The effects of boundary conditions can have a large influence on the measured rp amplitude that is position and geometry dependent, and therefore, most importantly can affect measurement of the size of a particle from the resistive pulse amplitude. Therefore, significant efforts have been directed towards finding more accurate expressions for specific particle and channel geometries. For instance, Smythe calculated the expected RP amplitude for spheres passing along the axis of cylindrical channels, and arrived at the expressions

$$\frac{\Delta I}{I_p} = \frac{d^3}{LD^2} \left[1 - 0.8 \left(\frac{d}{D} \right)^{-3} \right]^{-1}, \quad (6.2)$$

where d and D are the diameter of the particle and pore, respectively, and L is the length

of the channel. Equation 6.2 is probably the single most useful equation for sizing particles in resistive pulse experiments, however due to the preceding arguments we know it is only an approximation. For instance, it does not include particles that travel off-axis, and also assumes a channel length that is far greater than the length of the particle to be sized. Furthermore, it is only accurate for cylindrical channels and spherical particles. However, these specific conditions are seldom all true for systems of interest where RP sensing may be useful. The typical route taken in cases where Eq. 6.2 cannot fully capture the experimental findings is to devise a model that relates the position of the particle, the particle's geometry, and the geometry of the channel to hte expected rp amplitude. then, based on the model, conclusions are drawn from the Rp signal about the positoining and dynamics of the translocation. As a concrete example, berge *et al.* observed a positive correlation between the translocation times and the rp amplitudes of microbeads that were driven through their channels by an applied pressure. They argued that, due to the Poiseuille flow profile present in their channel, a larger translocation time correlated to an off-axis translocation, and therefore due to the correlation they observed between translocation time and RP amplitude, that off-axis translocations increased the RP amplitude magnitude. As another example, Tsutsui *et al.* performed experiments in low-aspect ratio pores and found a significant variance in the observed resistive pulse amplitudes that could not be explained by size variance in the population alone. They argued, therefore, that the combination of particle and channel geometry created a unique situation where the observed RP amplitudes was highly trajectory dependent, and they then devised a model to relate the trajectory to the RP amplitude.

In both of the above examples, the one-dimensional rp data set is used to study the complex dynamics of particle translocations through pores. The authors' inferences could very well be accurate, but could easily be validated or clarified by simply observing the translocations while simultaneously recording hte rp data. however, the difficulty in performing such an experiment is the scale at which they worked; at the nanoscale, only electron microscopy is viable due to the optical diffraction limit. However, because RP experiments are largely

scale independent, one possible option is to scale the solution up to a size where optical diffraction is possible, and to perform simultaneous RP and optical measurements. Such experiments could be used to clarify the positional dependencies of the rp signal, and the results would generalize back down to the nanoscale.

In order to resolve the positional dependencies of the RP amplitudes, we devised a microfluidic experimental and data analysis platform that allows simultaneous RP and IM measurements and analysis. The experimental system is based on a hihg-speed camera combined with an optical microscope which captures images of particles as they pass through a microfluidic channel while the ionic current is simultaneously recorded (described in greater detail in the following section). By tracking particles simultaneously in the two data streams, we are able to create a position-RP amplitude mapping for each particle. The mappings of many particles are combined to create a ‘resistance map’ of the channel, a two-dimensional plot of hte local resistance in the channel as measured by the instantaneous RP amplitude $\Delta I/I_p$, and which can address specific questions about the positional dependencies of the resistive pulses, including but not limited to:

- At which axial position does the RP amplitude attain its maximum value?
- What is the effect of lateral displacement of a particle inside the channel on its resulting RP amplitude?
- How is the variance distributed in variable-width channels, such as channels having a central cavity?

6.2 Experimental hardware and software

We devised a hybrid resistive pulse-optical imaging platform that is capable of resolving the spatial dependencies of the RP amplitude signals. The set up (Fig. 6.1) consists of a high-

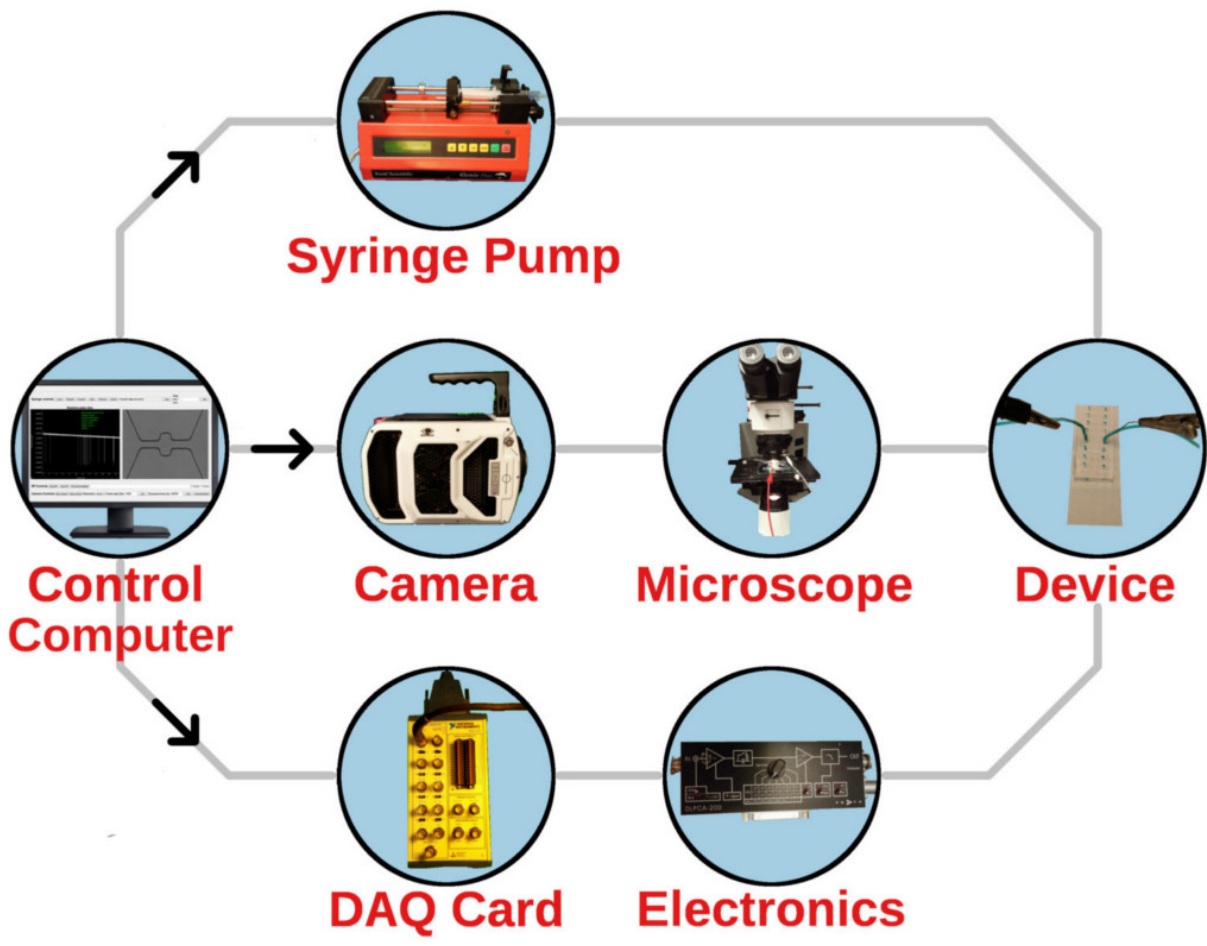


Figure 6.1: Hardware set up for the hybrid RP-IM experiments.

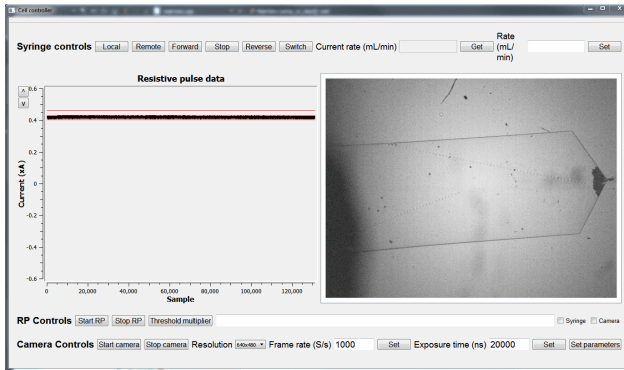


Figure 6.2: ***cell_controller***, a GUI program written in C++ and the Qt Framework. The program controls the instruments used to run the experiment.

speed camera combined with an optical microscope, all of the electronic equipment used to acquire the RP signal, a syringe pump to drive particle suspensions through the system, a planar microfluidic channel, and a central control computer used to run the experiment and record data.

The program used to control each of the instruments used in the experiment was written in C++ and makes use of the Qt framework to provide a GUI environment in which to run the experiment. The program is open-sourced and available at https://github.com/tphinkle/cell_controller. The software controls the high-speed camera, a data acquisition (DAQ) card used to record the current measurements, and the syringe pump. Each instrument uses its own communication protocol; the high-speed camera is controlled by commands sent via TCP/IP protocol over a 1 GB/s ethernet line, the DAQ card is controlled using the National Instruments NIDAQmx API, and lastly, the syringe pump is controlled via serial commands sent over an RS-232 line. A screen shot of the program is shown in Fig. 6.2.

The channels used for these experiments were made from PDMS bonded to a glass slide. PDMS is a transparent elastomer that is relatively inert, transparent, and durable, and for these reasons is probably the most common material used in microfluidic experiments today. Two classes of channels were created in PDMS, constant-width and variable-width, which will be discussed separately in the discussion section. Within each class of channels,

different geometries were considered. Images of some of the channels used in the experiments are shown in Fig. 6.4, along with lines indicating the tracked trajectories of individual particles (discussed below). 5 μm polystyrene beads were used as the experimental particle to track, and were suspended in 1 M unbuffered KCl solution. The high concentration of solution was chosen because it increases the signal-to-noise ratio, and facilitates analysis of the RP events. The syringe pump rate was chosen to be 0.005 mL/min, which enabled a large number of events to be detected while also allowing for good sampling of individual events in both the RP (250.000 kHz) and IM (50.000 kHz sample, 10 μs exposure) signals. At this flow rate, particles traveled a small ($<10 \mu\text{m}$) distance in between frames, and minimal blurring occurred. The *cell_controller* program recorded the camera and resistive pulse data simultaneously so that the two data streams are guaranteed to capture the same particle translocations.

6.3 Data analysis software

A software library called *pore_stats* was written in Python and PyQt to facilitate analysis of the resistive pulse data. The program includes a GUI application that can be used to quickly isolate the resistive pulses from the entire time-series. The application includes a number of convenient aspects, including the ability to find events in a drifting or unsteady baseline, the ability to low-pass filter the data to find events with a low signal-to-noise ratio, the ability to filter events based on their amplitude and duration, and a function that allows the user to train a logistic regression model in order to make automatic future accept/reject predictions. A screenshot of the program is shown in Fig. 6.3. Aside from the GUI program, *pore_stats* contains a wide variety of functions contained in a library that can be called to perform operations on the RP data, such as filtering, minimum/maximum detection, etc., and to calculate the relevant RP parameters such as duration, amplitude, sub-amplitudes, number



Figure 6.3: *Screen capture of the GUI component of the pore-stats software library.* The program enables fast and accurate extraction of RP events from the baseline data. The main panel shows the raw time-series data (zoomed out), with events that were detected with the program highlighted in blue. The bottom left plot shows a single event that has been targeted by the user. The bottom right plot shows a scatterplot of the current and duration for all events detected, and shows how bulk events can be rejected by selecting a region of the scatter plot. The bottom right buttons and fields are used to change the search parameters, to begin the search, filter data, and enable various other functionalities.

of events, event velocity, etc. Finally, because the experiments used for this project include simultaneous resistive pulse and optical tracking, the *pore-stats* library contains modules for analyzing the imaging data. The library enables detection of particles in individual frames, tracking of particles across frames, and a host of image processing tools that allow the user to calculate physical parameters of interest, such as particle size, aspect ratio, position, etc.

6.4 Results & Discussion

6.4.1 Data analysis explanation

The experimental hardware and software, and the data analysis software described above were used to perform the experiments and analyze them completely. The data analysis pipeline is as follows. First, the resistive pulse data was opened using the GUI application within the *pore-stats* library, which was used to extract the detected RP events. Once RP events were detected in the baseline of the time-series, they were saved separately. Next, the camera images were analyzed in order to track optical events. Particles were detected within individual frames using a thresholding approach; a frame in which no particles were present was used as a template, which was subtracted off individual frames. This subtraction yields an image where the pixels of the particles are highlighted white, and everything else is black. A flood-fill algorithm was then used to find incidences of connected pixels, which correspond to individual particle detections. Then, this analysis was performed on the next image in the camera's recorded video, and particles detected in this frame are connected with particles in the previous frame using a minimum-distance approach. Because we know the exact geometry of the channel, we are also able to determine the physical length of a pixel in the camera image. This is useful because we can then measure distance in physical units (e.g. microns) instead of pixel units. Additionally, we can also use the lines of the channel

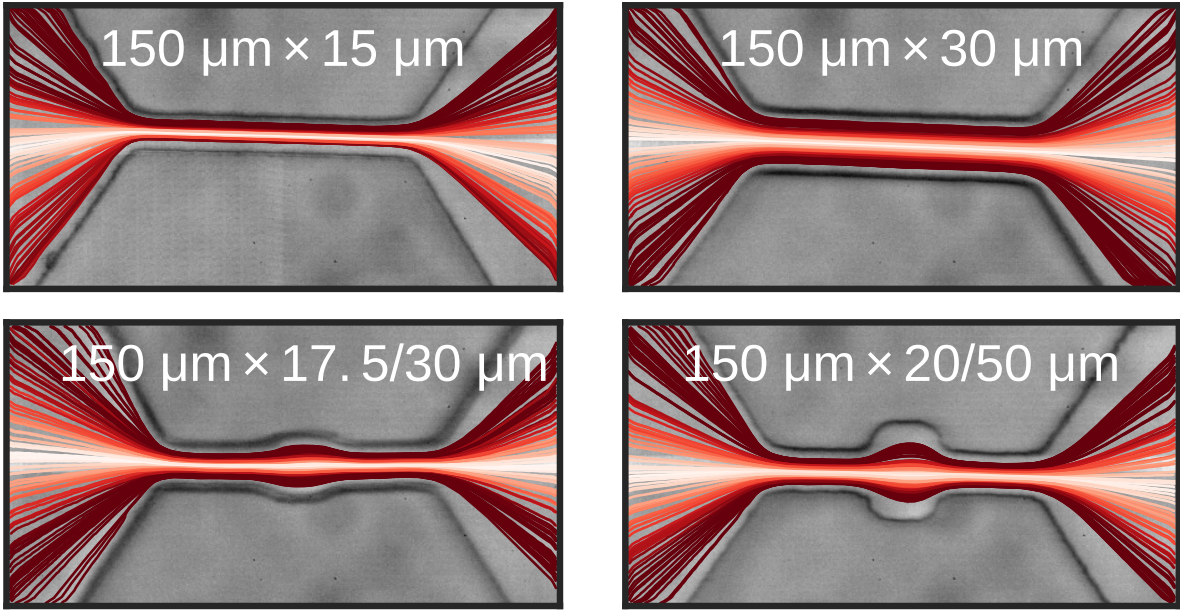


Figure 6.4: **Images of some of the channels used in this study with trajectory lines overlaid.** Each line corresponds to the passage of a single particle through the channel, tracked using image detection techniques. The channels fall into two categories, channels that are complete straight and channels which have central cavities.

to create a coordinate system with axes aligned with the axial and lateral directions of the channel. The end result is that through the coordinate transformation and particle tracking, we are able to calculate the actual trajectory in physical units that a particle undertakes when passing through a channel. The trajectory is then described by a sequence of pairs x_c, y_c , where x_c are the axial and y_c transverse coordinates of the particle with respect to the channel's coordinate frame, in physical units of microns. We chose a coordinate system such that $x_c = 0$ corresponds to the particle crossing the channel's threshold, and $y_c = 0$ on the channel's axis.

Because the particles travel very small distances in between frames, tracking individual particles across multiple frames is relatively straight forward. A string of individual detections comprises an IM event. In order to compare the events tracked via RP and IM, a protocol had to be established for matching the events appropriately. In order to do this, we first

constructed two time series corresponding to the times of events of the tracked RP and IM signals. The times from one signal were shifted until both sequences were seen to overlap. In many cases tracking of some particles fails in either signal. For instance, in the RP signal there could be a brief burst of noise that prevents detection of a pulse in the baseline. In the camera data, failure to track a single particle was less likely to occur, although still possible in principle. Unpaired events were dropped from the respective sequence to which they belonged. After this coarse alignment, we are left with two sequences *IM* and *RP* such that every event *i* in one signal has a matching event *i* in the other signal that is known to correspond to the same physical particle translocation. However, in order to compare actual data points in the RP and IM signals, a more fine-tuned alignment must be made. In order to perform this exact matching, we find two data points that are known to correspond to the same instant in time (up to the precision of the slower of the two instruments' sampling periods). For instance, for a pair of detected events in the RP and IM signals, we find the camera frame where the particle occupies the exact center of the channel, and the middle-most data point in the RP signal; we know that both data points correspond to the same instant in time (again, with precision given by the slower of the two sampling periods). Fine alignment of the two time series for each event is then achieved by adding a simple time offset to one of the signals, equal to the difference in times of the two corresponding data points. In principle, if the camera and DAQ card sampled at exactly the rates specified by their hardware specifications, and this rate did not change within a single recording, fine alignment of the entire time-series would be possible by simply aligning the RP and IM data of a single particle translocation. However, in practice we find that if we apply this offset for a single particle, the signals become out of sync at a later time, which is due to slight inaccuracies in their reported sampling periods. For this reason, we do not apply a single shift to the time-series in order to align the entire thing, but apply a unique alignment for every pair of events that we compare.

After aligning the two time-series and calculating the position of the particle in the channel's

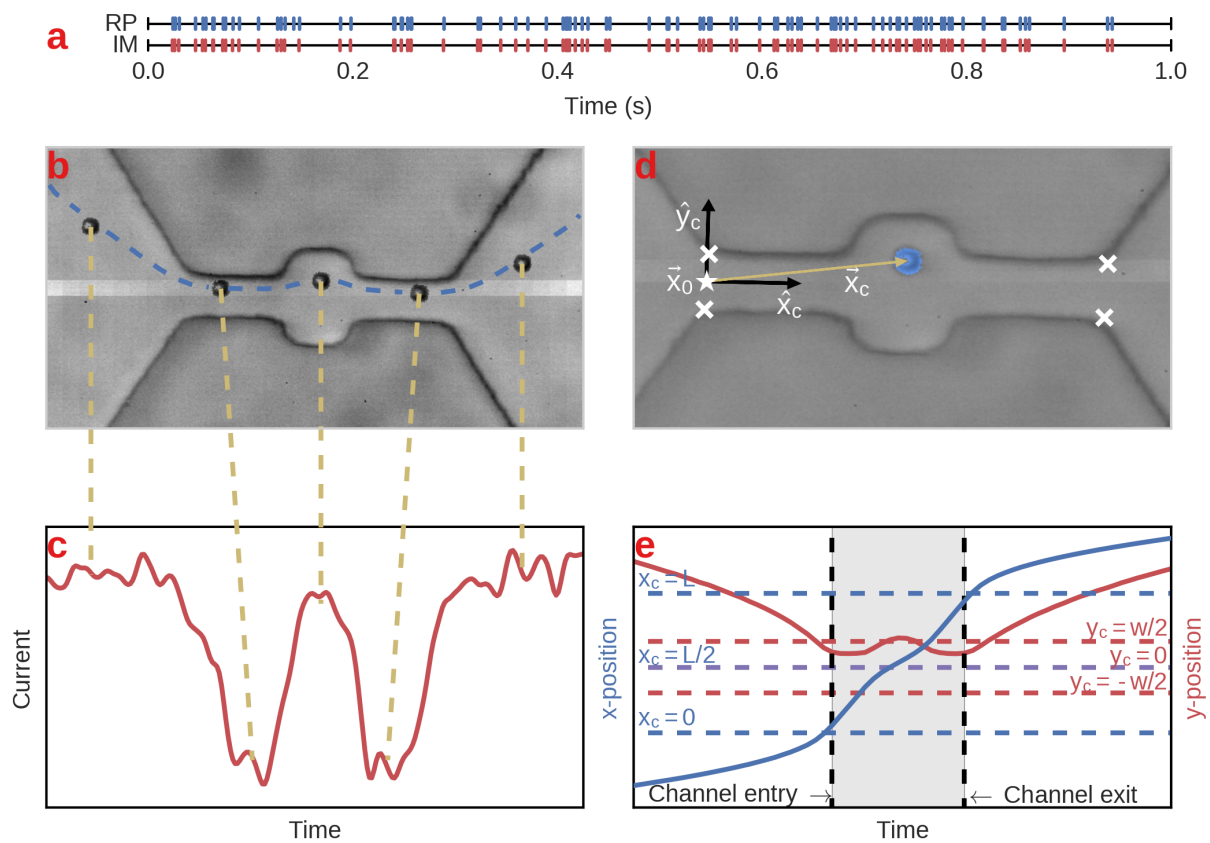


Figure 6.5: Event matching protocol for the RP and IM signals. a.

coordinate system, we have a time-series of data $x, y, \Delta I/I_p$; in other words, for every event we are able to determine the exact $\Delta I/I_p$ for every position in the particle's trajectory through the channel. The event matching protocol, as well as calculation of the particle's positions in the channel's coordinate frame, are shown in Fig. 6.5.

Armed with the synchronized data set, we can now explore positional dependencies of the RP signals. This matching allowed us to create ‘resistance maps’ of the channel, a picture of the channel that shows the amplitude of the $\Delta I/I_p$ at various points. Example resistance maps are shown in Fig. ???. Each data point in the resistance map indicates the position of a single particle at a single point in time, and the color reflects the instantaneous value of $\Delta I/I_p$ at that time. In the following sections we analyze resistance maps for straight channels and channels with non-constant widths.

6.4.2 Straight channels

The geometries of the straight channels used in this study are shown in Fig. 6.4, top row. The resistance maps determined for these channels are shown in Fig. ???. All channels were approximately $20\text{ }\mu\text{m}$ in height. The interior regions of hte channels show relativeliy darker red colors than the exteriors, indicating a higher resistance in accordance with our expectations. In the immediate vicinity of the channel, there is a region of moderate resistance known as the access resistance, which extends slightly inside the channel. In the rest of this section we delve into these aspects of the resistance map in greater detail.

Position of maximum RP amplitude in the channel

In the traditional RP technique, pulses are usually analyzed for their duration (sometimes called the dwell time) and their amplitude. The pulse duration is a measure of hte particle's

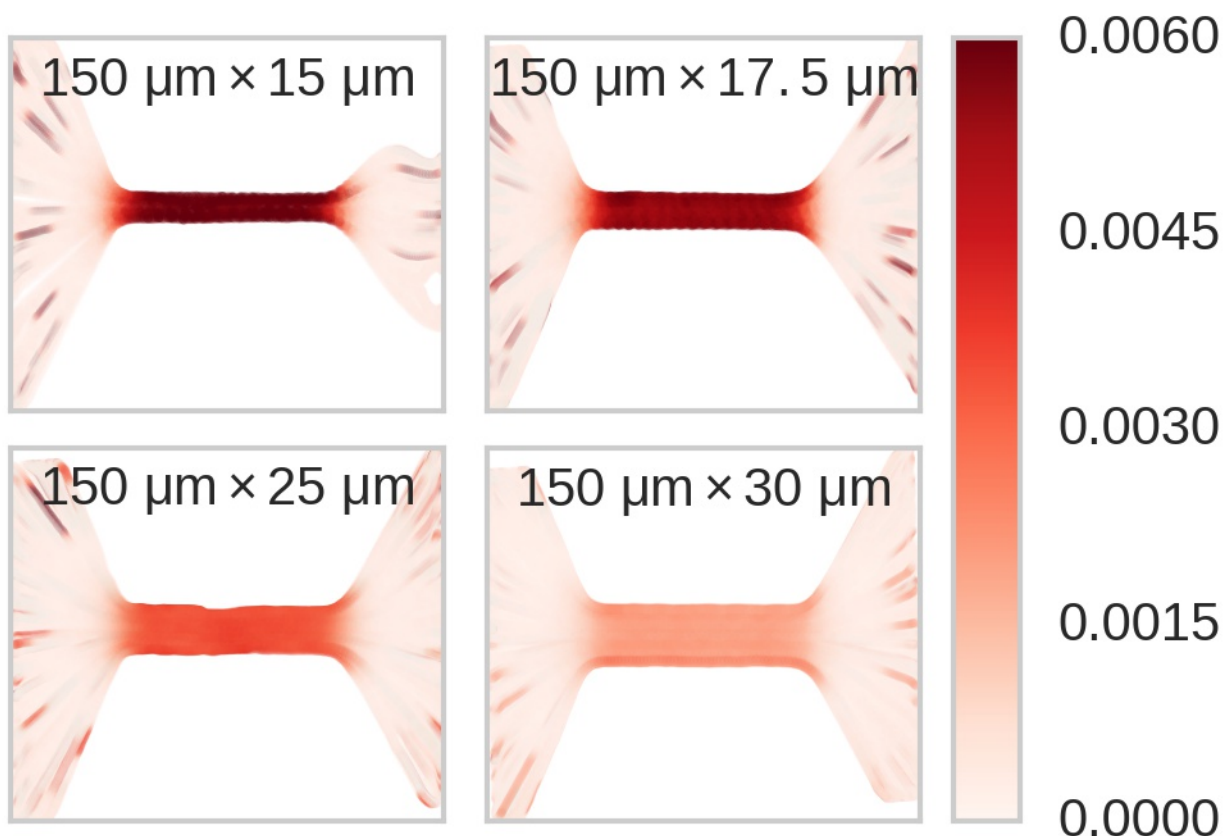


Figure 6.6: **Resistance maps of the straight channels used in this study.** The resistance maps show that the resistance is most concentrated in the micro constriction, and that the resistance is small elsewhere. A region of finite resistance exists between the micro constriction and the reservoir leading up to the channel. This region is known as the channel's access resistance.

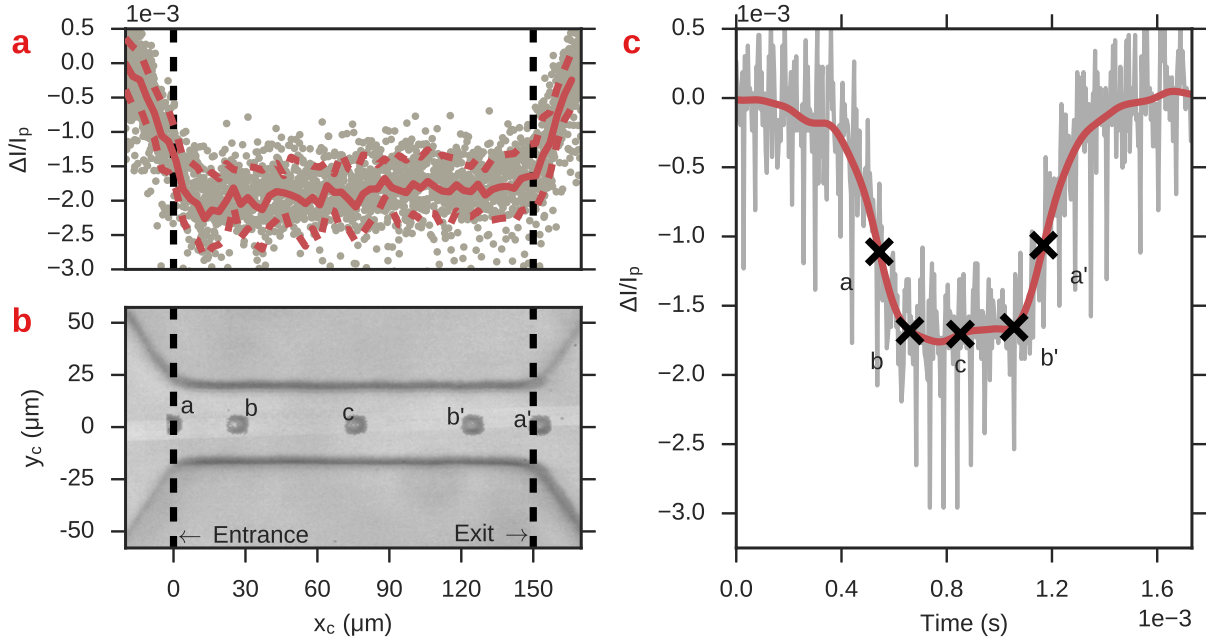


Figure 6.7: Plot of $\Delta I/I_p$ vs axial-position x_c for polystyrene beads passing through the PDMS channels. The plots reveal that the current does not reach its maximal value until the particle is well inside the channel.

velocity, and if the particles are driven through the channel electrophoretically or through electroosmosis, this becomes a basis for measurement of the particle or channel ζ -potential, respectively. However, an exact measurement of the dwell time is always somewhat arbitrary because there is no definitive point in the resistive pulse where we can say the start and stop of the event occurs. Typically some standard is adopted by the researcher for when the beginning and end of an event occur; most researchers choose to use the full-width-at-half-maximum (FWHM) as the points at which the particle enters and exits the channel. The resistance map will allow us to directly observe the current value at the entrance and exits of the channel, and to compare this with the FWHM of the signal to see if this standard is justified. We created plots of the axial position x_c and instantaneous current value $\Delta I/I_p$ for each event for the straight channels studied. Figure 6.7 shows a single event from the recorded RP time series alongside the data of many events plotted in coordinates of $\Delta I/I_p x_c$. The figure reveals two interesting features. First, the current does not plateau until the particle is

well within the channel, even more than its full diameter. This result is unusual, and suggests that the entrance of the pore has less resistance than its entrance points, even though these points have the same width. Another result is that the point at which the particle crosses the threshold of the channel corresponds very closely to the FWHM of the pulse, a result which suggests that for the purposes of measuring the dwell time of the particle, the FWHM may be a more accurate estimate than a thresholding approach.

Dependence of resistive pulse amplitude on lateral displacement

As mentioned in the introduction to this chapter, off-axis translocation of a particle is expected to significantly effect the amplitude of the RP signal it creates. This effect is significant in sizing applications, where it broadens and shifts the distribution of the particles sizes as measured by RP. In order to better understand the effect of off-axis translocation on the RP amplitude, Berge *et al.* performed experiments with particles driven through pores by an induced pressure. As opposed to electroosmosis, pressure-driven flow results in a Poiseuille distribution of the fluid flow rate, which is parabolic and greatly varies across the face of the channel. The experimenters used their knowledge of Poiseuille flow to determine the lateral offset position y_c of the particles based on their translocation time. They observed that the slower moving particles with greater offset position also had larger resistive pulse amplitudes than faster moving, on-axis particles. They devised an empirical relationship from the data of the following form:

$$\frac{\Delta V}{\Delta V_0} = 1 + \alpha \left(\frac{y_c d}{D} \right)^3, \quad (6.3)$$

where d is the diameter of the particle, D the diameter of the pore, and α was a constant

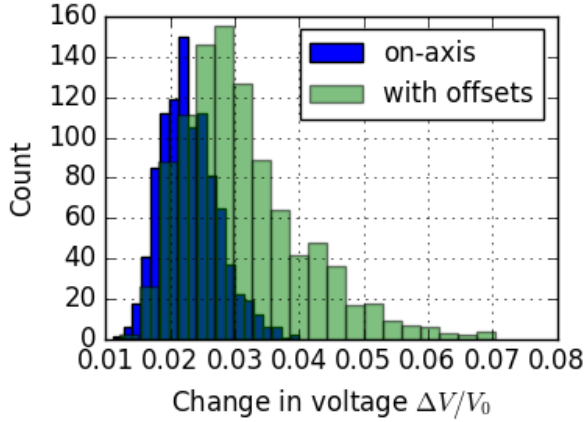


Figure 6.8: Plot of the measured voltage (similar to current) of simulated particle translocations through a pore, with off-axis contribution according to the results of Berge *et al.* (Eq. 6.3). The plot reveals the effects of off-axis translocation, namely that the distribution of measured ΔV shifts towards greater values and broadens.

determined to be between 5 – 7.5. The equation shows that the distribution of diameters D as determined by RP is both broadened and shifted towards higher diameters by the off-axis effect. Figure 6.8 shows simulated data of particles passing through a pore and the resultant measured $\Delta V/V_0$ (the quantity measured by Berge in his original work).

Although the effect was well-established by the authors, it was only indirectly inferred from the data. Using the hybrid RP-IM approach, we can directly measure the effect of off-axis translocations in RP experiments. Before directly showing the relationship, we first confirmed that we observed the exact same relationship observed by Berge *et al*, namely a positive correlation between translocation time and pulse amplitude. This relationship is shown in Fig. 6.9. The scatter data were fit with straight lines, and reveal that not only does the event amplitude increase with increasing translocation time, but that this effect decreases with increasing channel width in accordance with Eq. 6.3.

The results are shown in Fig. 6.10. The left column of Fig. 6.10 shows the translocation time Δt versus the off-axis position y_c for the straight channels studied, while the right hand column shows $\Delta I/I_p$ versus y_c for the same events. The left column indicates that

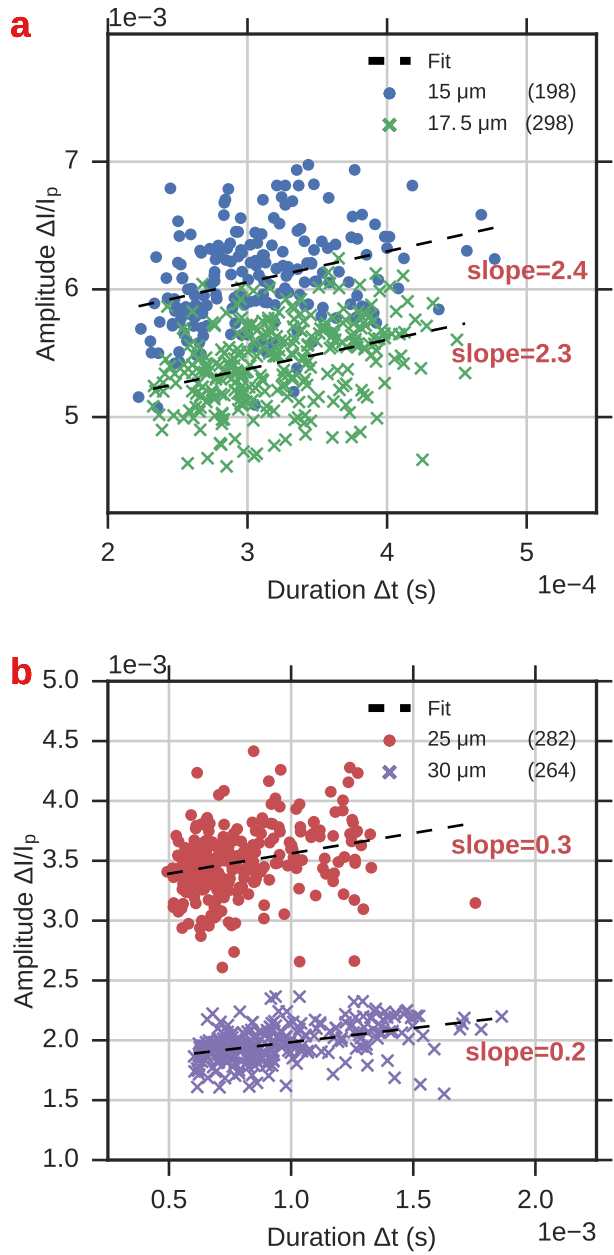


Figure 6.9: Scatter plot of translocation duration Δt versus event amplitude $\Delta I/I_p$ for the four straight channels studied, with straight line fits. The fits reveal the positive correlation between translocation time and off-axis position, as observed by Berge *et al.*.

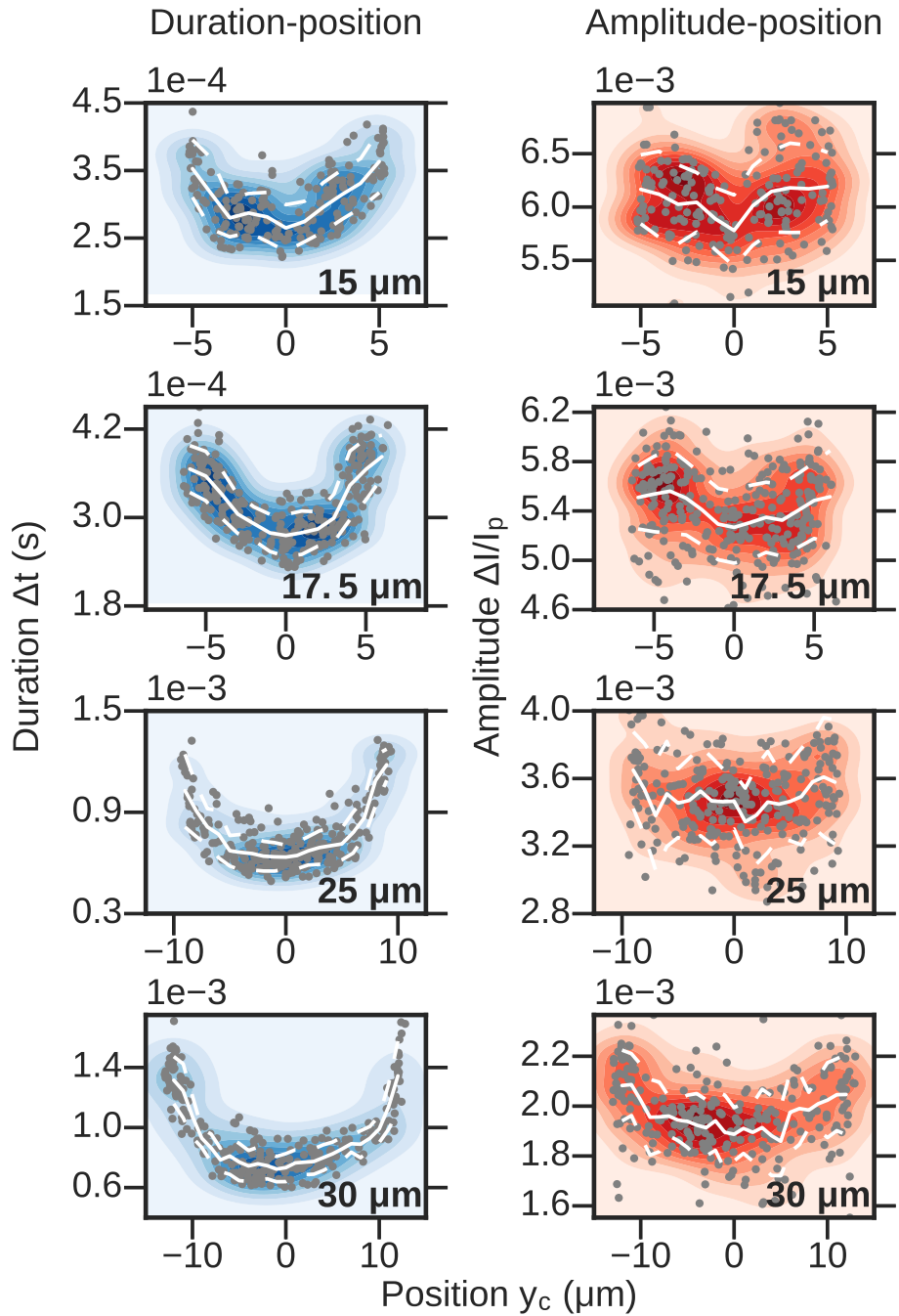


Figure 6.10: Translocation duration Δt and RP amplitude $\Delta I/I_p$ versus lateral position y_c for four straight channels.

the translocation time strongly increases at off-axis positions closer to the channel walls, in accordance with our expectations for the fluid flow profile of Poiseuille flow. Additionally, the right hand figures reveal that the amplitude increase $\Delta I/I_p$ also increases for particles passing closer to the channel walls, in agreement with the results observed by Berge [1] and predicted by Smythe [8]. The relationship between amplitude and position is not as strong as of that between translocation time and position, but in all four channels studied we still observed the same dependence. The difference between minimum and maximum $\Delta I/I_p$ from the four channels is approximately 8%; this difference, while small, is non-negligible and is in rough agreement with the level of difference found in the Berge papers (10%). We note that measurement of the current amplitude of a single event is itself an inherently noisy process. First, the baseline must be accurately determined, which is often an ambiguous measurement, especially when dealing with noisy baseline signals. Second, the interevent current itself is a noisy measurement due to the noise within the signal and the fact that the current level may slightly change during translocation due to non-perfect smoothness of the PDMS channels. For instance, in Fig. 6.7, we see that the event is not perfectly flat, indicating perhaps that there is a small slope in the height of the channel. However, regardless of the noise in the measurement, each of the channels still directly reveal the trend of off-axis translocation increasing the measured resistive pulse amplitude.

6.4.3 Channels with a central cavity

The next section covers channels that have a central cavity. The geometry of the devices is shown in the bottom of Fig. 6.4. All channels were approximately $20\ \mu\text{m}$ tall. Resistance maps are shown in Fig. ???. The geometry used here is somewhat artificial, and channels having central cavities are not a wide class of channels or pores used in resistive pulse studies. However, channels with non-constant widths, and even with widths that discretely changes from one value to another are not uncommon in resistive pulse applications. For instance,

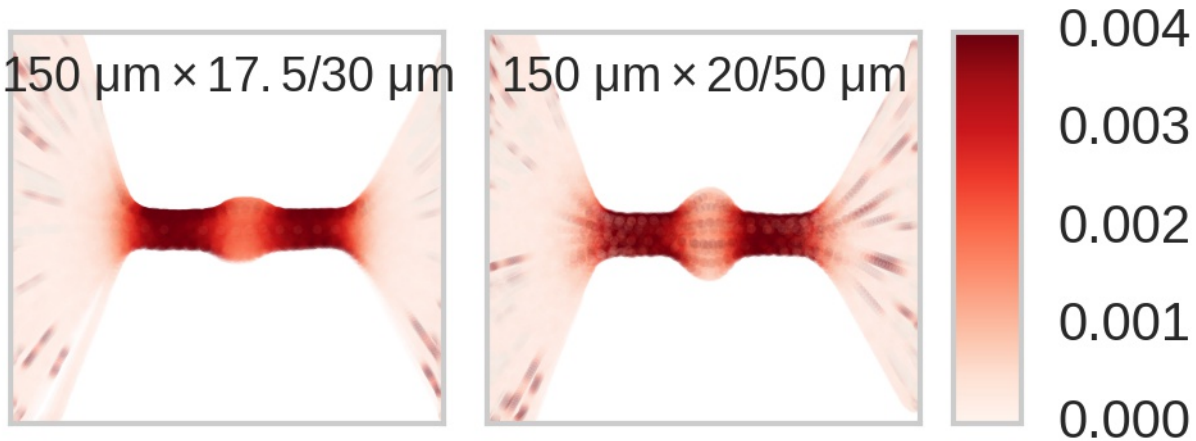


Figure 6.11: **Resistance maps of channels having a central cavity.** The resistance maps show that the resistance is most concentrated in the narrow portions of the channel, and less-so in the central cavities (as expected from $R = \rho \int dz/A(z)$).

one of the most commonly used biological nanopores is known as α hemolysin, which is characterized by having a narrow half and a wide half. However, the particular geometry of a channel with a central cavity was recently proposed as a platform for creating positionally-dependent hydrodynamic forces that can deform particles in a controlled manner. This channel geometry was promoted as a means of probing the deformability of single human cells, a topic that will be discussed in the next chapter of this dissertation. In the rest of this section, we discuss the distribution of resistance in the channel as determined by the resistance maps, as well as the effects of off-axis translocation of particles. In particular, we find an interesting relationship between off-axis position and pulse amplitude that behaves opposite to what was found in the previous section on straight channels.

Resistive pulse amplitude in the wide and narrow portions of the channels

Basic physics considerations suggest that the resistance should be more concentrated in the narrow portions of the channel than in the central cavity, and therefore that the resistive pulse amplitudes should be larger in the narrow portions as well. This simple feature of the system is confirmed by the shapes of the individual resistive pulses; an example can be found

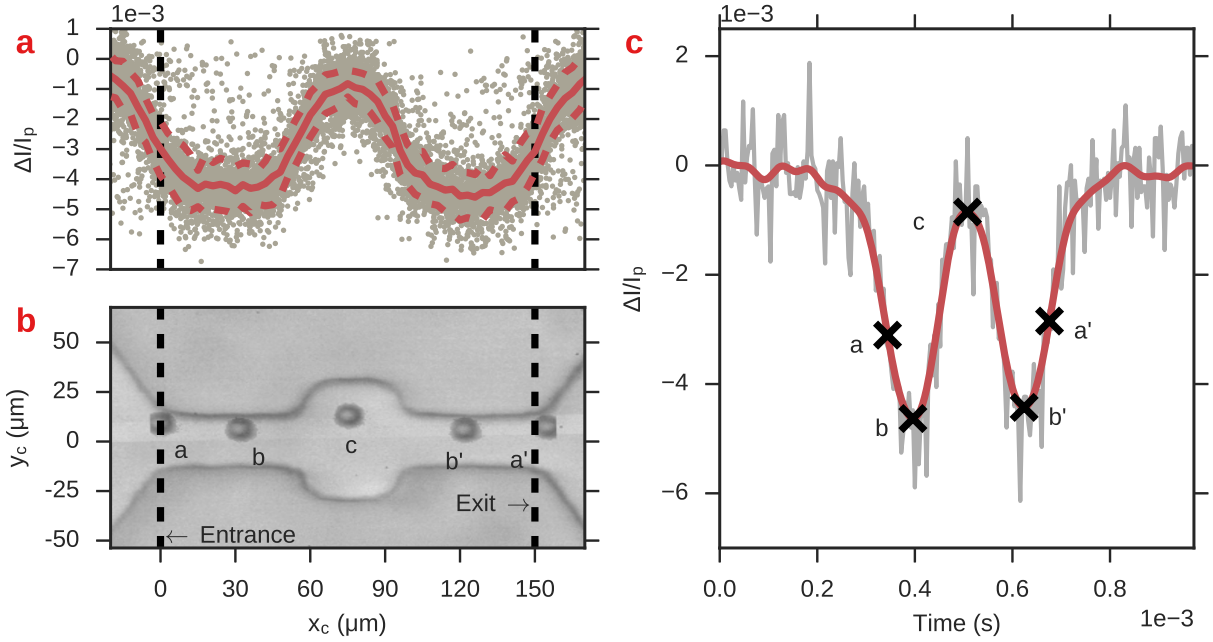


Figure 6.12: Resistive pulse amplitude $\Delta I/I_p$ versus axial position x_c (a) and versus time t (c). The camera image (b) shows several stills of particle positions aligned with the instantaneous resistive pulse value in the plot above (a).

in Fig. 6.12c.

$$\begin{aligned} \Delta R &= \frac{4\rho d^3 S (d/D)}{\pi D^4} \\ &= \frac{4\rho d^3}{\pi D^4} \left[1 - 0.8 \left(\frac{d}{D} \right)^3 \right]^{-1} \end{aligned} \quad (6.4)$$

However, a more quantitative description of the distribution of the local resistance in the channel is found in equation 6.4 [3]. Since our experiment measures the current rather than the resistance, we can use our experimental data to verify Eq. 6.4 by observing that

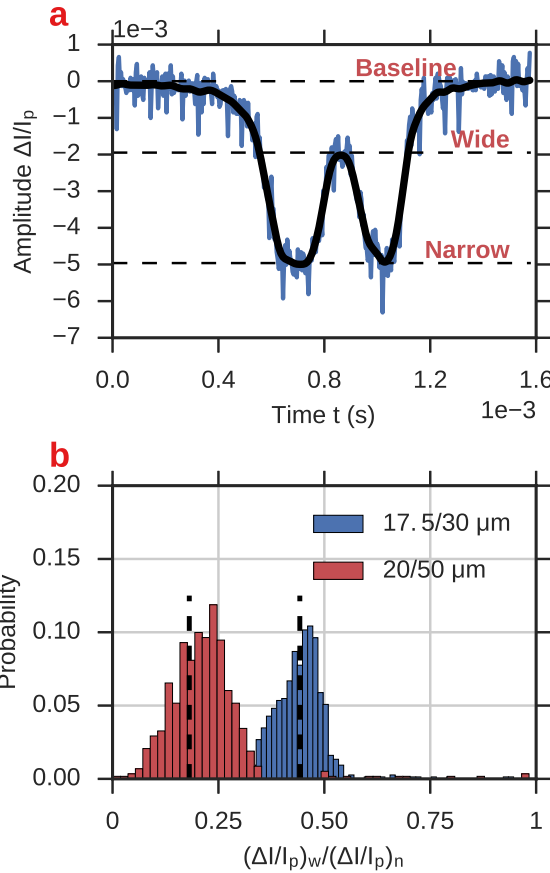


Figure 6.13: **Histograms of the ratios of the pulse amplitude $\Delta I/I_p$ in the narrow portion of the channel and in the central cavity for the two types of cavitated channels studied.** The dashed lines indicate the theoretical values predicted by Eq. 6.5. In both cases, the theoretical predictions closely match the experimentally obtained results.

$\Delta R/R_0 = \Delta I/I_p$, and therefore

$$\frac{\Delta I/I_p|_{x_c=x_{c1}}}{\Delta I/I_p|_{x_c=x_{c2}}} = \frac{\Delta R/R_0|_{x_c=x_{c1}}}{\Delta R/R_0|_{x_c=x_{c2}}} = \frac{\Delta R|_{x_c=x_{c1}}}{\Delta R|_{x_c=x_{c2}}}. \quad (6.5)$$

Equation 6.4 can be substituted into the final expression in 6.5, and therefore the equation allows us a means of comparing the experimentally obtained values for $\Delta I/I_p$ with the theoretical equations. This operation was performed for each of the channels with central

cavities, with x_{c1} corresponding to the particle occupying the narrow portion of the channel, and x_{c2} corresponding to the particle occupying the exact middle of the cavitated part of the channel. The results are shown in Fig. 6.13. The histograms indicate the distribution of the experimentally measured ratios, while the dashed lines represent the theoretical predictions of equation ???. The spread in each distribution is a combination of measurement error on the exact values of the current, an intrinsic (although small) spread in the distribution of sizes of the particles, and perhaps most importantly, the distribution of off-axis positions y_c , which we showed significantly contributed to the measured $\Delta I/I_p$ in the previous section, and which we will further discuss in the next section. While the dashed lines overlap well with the actual distributions, we note that there is a discrepancy in both cases. Equation 6.5 was derived for spheres moving through cylindrical channels only, and so we expect that our channels, which have rectangular cross-sections, may not adhere perfectly. In using Eq. 6.5, we approximated our channels as cylinders having radii that would yield a cross-sectional area the same as the actual cross-sectional area of the rectangular channels. This approximation will be more accurate for low-aspect ratio cross sections (i.e. squares), and less-so for larger aspect ratio channels. This observation agrees with our findings: the $20 - 50 - 20\mu\text{m}$ channel has a larger aspect ratio in its cavity, and also happens to have a greater discrepancy between the experimental results and the theoretical predictions of Eq. 6.5.

Bibliography

- [1] L. I. Berge, T. Jossang, and J. Feder. Off-axis response for particles passing through long apertures in coulter-type counters. *Meas. Sci. Technol.*, 1(6):471, 1990.
- [2] L. Bocquet and E. Charlaix. Nanofluidics, from bulk to interfaces. *Chem. Soc. Rev.*, 39:1073–1095, 2010.
- [3] R. W. DeBlois, C. P. Bean, and R. K. Wesley. Electrokinetic measurements with sub-micron particles and pores by the resistive pulse technique. *J. Colloid Interface Sci.*, 61(2):323–335, 1977.
- [4] M. J. Fulwyler. Electronic separation of biological cells by volume. *Science*, 150(3698):910–911, 1965.
- [5] E. Keogh and C. A. Ratanamahatana. Exact indexing of dynamic time warping. *Knowledge and Information Systems*, 7(3):358–386, Mar 2005.
- [6] A. J. Pascall and T. M. Squires. Induced charge electro-osmosis over controllably contaminated electrodes. *Phys. Rev. Lett.*, 104:217–252, Feb 2010.
- [7] Y. Qiu, P. Hinkle, C. Yang, H. E. Bakker, M. Schiel, H. Wang, D. Melnikov, M. Gracheva, M. E. Toimil-Molares, A. Imhof, and Z. S. Siwy. Pores with longitudinal irregularities distinguish objects by shape. *ACS Nano*, 9(4):4390–4397, 2015. PMID: 25787224.
- [8] W. R. Smythe. Offaxis particles in coulter type counters. *Rev. Sci. Instrum.*, 43(5):817–818, 1972.
- [9] T. M. Squires and M. Z. Bazant. Induced-charge electro-osmosis. *J. Fluid Mech.*, 509:217252, June 2004.
- [10] I. Vlassiouk and Z. S. Siwy. Nanofluidic diode. *Nano Lett.*, 7(3):552–556, 2007. PMID: 17311462.
- [11] C. Yang, P. Hinkle, J. Menestrina, I. V. Vlassiouk, and Z. S. Siwy. Polarization of gold in nanopores leads to ion current rectification. *J. Phys. Chem. Lett.*, 7(20):4152–4158, 2016.

Appendix A

Appendix Title

A.1 Lorem Ipsum